The Dissertation Committee for Ju Zhang
certifies that this is the approved version of the following dissertation:

Simulation of Gas Dynamics, Radiation and Particulates in Volcanic Plumes on Io

Committee:

David B. Goldstein, Supervisor

Philip L. Varghese, Supervisor

Laurence M. Trafton

Thomas J.R. Hughes

Laxminarayan L. Raja

Simulation of Gas Dynamics, Radiation and Particulates in Volcanic Plumes on Io

by

Ju Zhang, B.S.

DISSERTATION

Presented to the Faculty of the Graduate School of

The University of Texas at Austin

in Partial Fulfillment

of the Requirements

for the Degree of

DOCTOR OF PHILOSOPHY

THE UNIVERSITY OF TEXAS AT AUSTIN

May 2004

Dedicated to my parents.

Acknowledgments

I would like to thank my advisor, Dr. David Goldstein for his guidance, support and encouragement throughout the span of our research. His tireless and constant quest of knowing "why" has stimulated the creativity of this work. I would also like to thank my other advisor, Dr. Philip Varghese, for sharing his wisdom and communication skills, and for his emphasis on conveying ideas appropriately and accurately. I also extend thanks to Dr. Laurence Trafton for the fruitful discussion and important suggestions during our regular group meetings, and Dr. Deborah Levin, Natalia and Sergey Gimelshein for productive collaborations.

I wish to acknowledge the previous work by my past colleague, Victor Austin, without which our research would not have gone as far as it did. His efforts and help in explaining his program to me deserve my special thanks. I also wish to express my thanks to my other past and present colleagues: Roberto Roveda, Conrad Lee, Sidra Silton, David Young, Joung Yeoung Shim, Chris Moore, Kenji Miki, Benedicte Larignon, Gerardo Colmenero, Kevin Marr and Yuto Shinagawa. Notable thanks go to Roberto Roveda and Conrad Lee for familiarizing the foreigner with the environment during the early time, and Chris Moore and Kenji Miki for the fruitful discussion.

Gratitude and best wishes to my friends at UT. Special thanks go to

Guanghua Wang for penetrating discussions.

Eternal thanks to my parents and my brother for their constant high expectations and their sacrificing the many occasions of traditional family union.

Simulation of Gas Dynamics, Radiation and Particulates in Volcanic Plumes on Io

Publication No. _____

Ju Zhang, Ph.D.
The University of Texas at Austin, 2004

Supervisors: David B. Goldstein
Philip L. Varghese

Volcanic plumes on Jupiter's moon Io are modeled using the direct simulation Monte Carlo (DSMC) method. The main goal of this work is to improve the understanding of Ionian atmosphere itself and the internal processes that are responsible for the volcanic plumes with rarefied gas dynamics modeling techniques developed for aerospace engineering applications.

A DSMC model including spherical geometry, variable gravity, internal energy exchange (discrete vibration-translation and continuous rotation-translation energy exchange) in the gas, infrared and microwave emission from the gas, multi-domain sequential calculation to resolve the fast emission event, opacity and two phase gas/particle flow, has been developed. Increasing confidence in our model has been built up through the encouraging matches to and agreements with a variety of observations, such as plume shape, vertical gas

column density in the plumes, plume images, plume shadows, ring depositions, *etc.*.

A concept of virtual vent is proposed for both volcanic tube and lava lake plumes. A parametric study of the two most important parameters at the virtual vent - velocity and temperature - is performed. Constraints are put on the vent conditions via the observables such as the canopy shock heights, peak gas deposition ring radii, vertical and tangential gas column densities, and total gas mass and emission power. Also, the flow of refractory 1 nm – 1 μm particles entrained in the gas is modeled with "overlay" techniques which assume that the background gas flow is not altered by the particles. The column density along the tangential lines-of-sight and the shadow cast by the plume are calculated and compared with Voyager and Galileo images. Encouraging matches are found between simulations and observations.

The model predicts the existence of a canopy-shaped shock inside the gas plume, a multiple bounce shock structure around a dayside plume, a frost depletion by the gas bounce, concentration of emission in the vibrational bands in the vent vicinity and re-emission at the shocks for certain band. An upper limit on the size of spherical particles that can track the gas flow in the outer portion of the plumes is ~10 nm. Particles of size ~1 nm can track the gas flow well throughout the entire plume. A subsolar frost temperature in the range of $\sim 110 - 118$ K is suggested.

Table of Contents

List of Tables

List of Figures

xviii

xix

xxiii

Chapter 1

Introduction

1.1 Motivation

One of the most startling discoveries of the Voyager flybys of Jupiter was the existence of spectacular umbrella-like plumes over nine points on Io's surface. The first discovered volcanic plume, Pele, rises more than 300 km above the surface (Strom and Schneider 1982). Volcanic plumes have also been observed during several Galileo flybys of Io. Figure 1.1 shows one of the Galileo images of Io's surface and two active volcanic plumes. Figure 1.2 shows the Voyager image of the ultra-violet brightness of Pele plume, and Fig. 1.3 the visible Voyager image of Prometheus (Note the remarkable "spider arms" of ejecta from this plume). Pele is so large in size that it is even detected by HST (Fig. 1.4). Subsequent to their discovery, modeling of these volcanic plume flows has been one of the major tasks associated with Ionian atmospheric studies as will be illustrated in the following section. The modeling of these plumes has also been the focus of the present work.

Many Ionian volcanoes manifest themselves by particulates rising high above the surface and many observable features of Ionian volcanic plumes are associated with the fine particulates in these plumes. Most of the Voyager
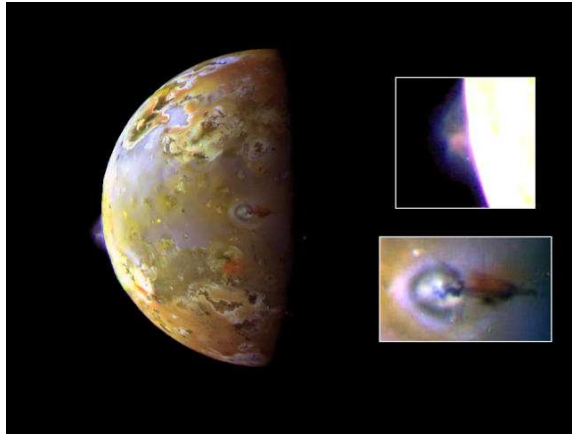
Figure 1.1: Galileo images of Io's volcanic Plumes. Pillan Patera is seen on the limb while Prometheus is seen from above near the terminator (boundary between day and night).
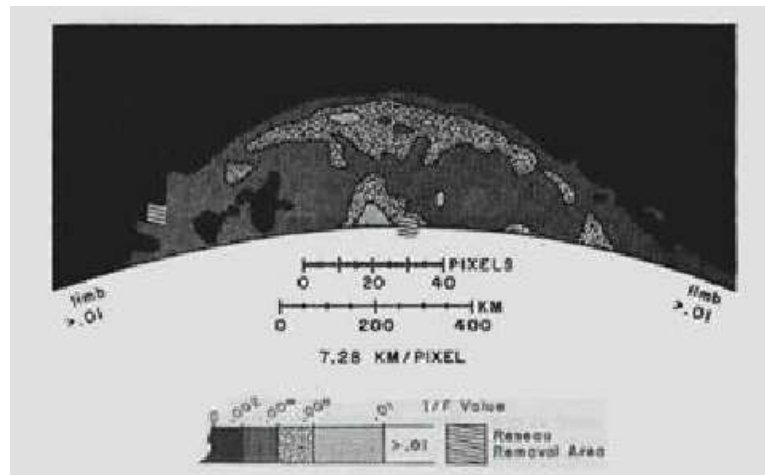
Figure 1.2: Voyager image of the ultra-violet brightness of Pele, (*From Strom and Schneider (1982), courtesy of Robert Strom*).
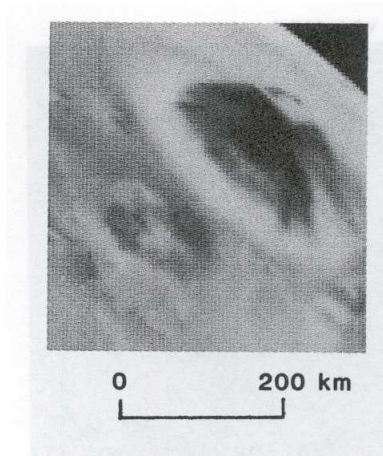
Figure 1.3: Voyager image of Prometheus, (*From McEwen and Soderblom (1983), courtesy of A. McEwen*).

and Galileo plume images likely show sunlight scattered by particles (possibly snow-flakes, droplets and/or dust) entrained in the plumes. Photometric studies of Loki by Collins (1981) indicate that particles of various sizes (from 0.01 μm up to 1000 μm) are present. Strom and Schneider (1982) suggested that the bright envelope appearing in the smoothed ultraviolet brightness images of Pele may be the result of a concentration of particles at a shock front.

Another remarkable feature associated with most volcanic plumes on Io is the ring deposits as can be seen in Fig. 1.1 around Prometheus. Figure 1.5 shows another Galileo picture of the surface marking around Pele.

Unfortunately, despite its discovery more than 25 years ago, the atmosphere of Io remains poorly understood. The main goal of this work is to improve the understanding of Ionian atmosphere with rarefied gas dynamics

3
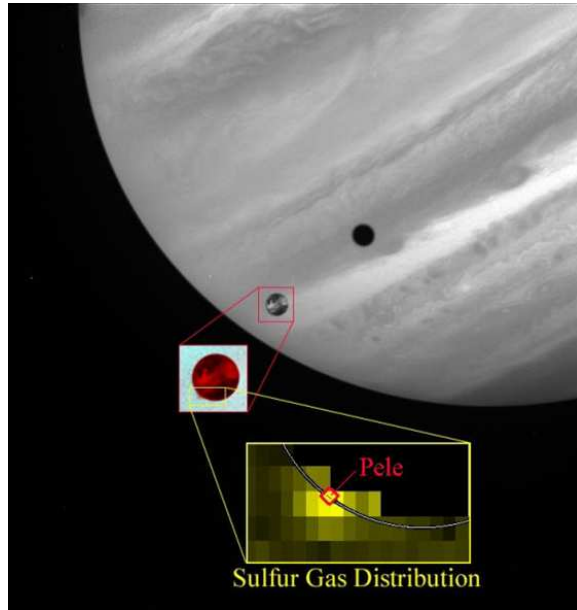
Figure 1.4: HST image of Pele.

modeling techniques developed for aerospace engineering applications. Specifically, the direct simulation Monte Carlo (DSMC) method is used. Io is by far the most volcanically active body in the solar system and the volcanic gases expand into a near vacuum, so some regions of the atmosphere resemble nozzle flow and hypersonic jets – typical aerospace engineering applications. Most of the observations of planetary atmospheres, and all of those for Io, are via remote sensing of the radiation produced by, or transmitted through, the gas. Thus, there is reason to develop advanced techniques to model, in an integrated way, the gas-dynamics of hypersonic volcanic jet flow along with the radiated signature that may be observed. As mentioned above, many observable features of Ionian volcanic plumes are associated with the fine particulates

4
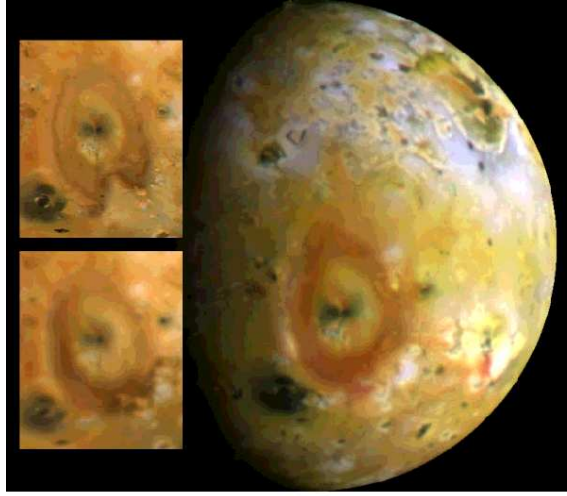
Figure 1.5: Galileo images: Note the red ring deposition around Pele. The inset images are from the Voyager 1 (top) and 2 (bottom) spacecraft.

in these plumes. Thus, there is also reason to study the behavior of two phase gas/particle flow in these volcanic plumes. Such techniques also have engineering applications, *e.g.* to understand rocket plume signatures, multiphase flows, and satellite plume impingement and interference effects.

1.2   Objectives

The main goal of this work is to improve the understanding of Ionian atmosphere itself and the internal processes that are responsible for these volcanic plumes. In the present work we concentrate on modeling the hypersonic plume flow of Io's volcanoes. The unique features of the problem distinct from the familiar aeronautical engineering applications are the significance of gravity (which causes the plume to eventually fall back upon itself), the unusual

gas species (SO_2), the low collision frequencies (seconds-to-minutes between collisions), and the large mean free paths (centimeters to kilometers). Emphasis was placed on reproducing and explaining observed features (plume images, shadows, deposition patterns etc.), helping to predict possible observables, and developing some theoretical gas dynamic analysis. The gas dynamics and radiation coupling proposed in the vent vicinity and the transport of particulates in the plume will be studied in great detail. One can compare results to observations from Earth, from HST and from the Voyager, Galileo and Cassini.

1.3 Dissertation Overview

A literature review of earlier observations and numerical studies of the Ionian atmosphere is provided in Chapter 2.

Chapter 3 describes the details of various innovations incorporated in the DSMC model, including the consideration of a body force (gravity), SO_2 internal energy exchange, radiation from rotational lines and discrete vibrational bands (aimed at connecting the gas dynamic simulation to the radiation signature of the plumes by remote sensing), multi-domain calculations to resolve radiation in the vent vicinity, and "overlay" gas/particle flow modeling.

Examples and basic features of simulated volcanic plumes on Io and comparisons with observation data are presented in Chapter 4. Further results and comparisons are given in Chapter 5, including a parametric study of vent conditions, matching a variety of observations including plume images, plume shadows and ring deposition. The concept of the "virtual" vent and

6

the simulations of lava lake plumes are discussed in Chapter 6. Concluding thoughts are presented in Chapter 7.

Chapter 2

Literature Review

2.1 Early Observations

An overview of pre-Galileo observations is provided by Lellouch (1996). Here, a very brief summary of such early work is presented.

As mentioned in the introduction section, one of the most startling discoveries of the Voyager flybys of Jupiter was the existence of spectacular umbrella-like plumes over nine points on Io's surface. The first discovered volcanic plume, Pele, rises more than 300 km above the surface. Strom and Schneider (1982) suggested that the bright envelope appearing in the smoothed ultraviolet brightness images (*cf* Fig. 1.2) of Pele may be the result of a concentration of particles at a shock front. McEwen and Soderblom (1983) analyzed the plumes observed by Voyager and classified the plumes into two types, Pele- and Prometheus-type. Photometric studies of Loki by Collins (1981) constrained the particle sizes in the plume.

The first measurements suggesting an Ionian atmosphere were those of Binder and Cruikshank (1964) who reported that Io was brighter by about 10% during an interval of $\sim$15 min. after emerging from a Jupiter eclipse. The favored explanation was that during the eclipse, some part of an atmosphere

condenses to form a bright frost or haze. The first direct evidence of an Ionian atmosphere was obtained by Kliore *et al.* (1975) who used the Pioneer radio occultation experimental finding of an ionosphere to calculate a surface pressure of the order of nanobars near the terminator. SO_2 gas was first detected by Pearl *et al.* (1979) using the Voyager IR spectrometer (IRIS) to identify the ν_3 band of SO_2 at 7.3 μm. Millimeter observations by Lellouch *et al.* (1990) and Lellouch *et al.* (1992) of SO_2 rotational lines emission provided further evidence of an SO_2 atmosphere. Later, HST observations of UV sunlight reflected from Io's surface with numerous SO_2 absorption bands (Ballester *et al.* 1994) also supplied persuasive evidence of an SO_2 atmosphere on Io. These observations had limited success in defining the spatial distribution of Io's atmosphere. Recently, McGrath *et al.* (2000) suggested the spatial variability of SO_2 and SO on Io. The SO_2 column density observed over a high-latitude region was $\sim 7 \times 10^{15}$ cm^{-2}, while that over the Pele volcano was a factor of 5 higher, perhaps due to an active plume at Pele. The 1.5×10^{16} cm^{-2} SO_2 column density observed over Ra, a bright equatorial region that may also have contained an active plume, was a factor of two higher than that detected over the high latitude region.

2.2   Numerical Study

Numerical studies of Io's atmosphere began with the work of Ingersoll *et al.* (1985) who solved the vertically integrated conservation equations in which the flow properties (horizontal velocity, atmospheric pressure, tempera-

ture etc.) are functions of angular distance from the subsolar point. Therefore, the model is essentially one dimensional which appears to be inadequate for the highly dynamical three dimensional atmospheric structure on Io. The model does not consider the plasma bombardment, which plays an important role in determining the structure of any Ionian atmosphere. Most of all, the rarefaction and non-LTE (non-local-thermodynamic equilibrium) effects are not included in the model. This limited the model's applicability because of the wide-range of flow regimes from virtually continuum flow to free-molecular flow, present on Io. The continuum assumption breaks down in low-density flows as the mean free path of molecules becomes comparable to the length scale of flow features; this invalidates the use of a continuum flow modeling. In spite of all these limitations, Ingersoll *et al.* (1985) found that the sublimation of SO_2 gas from frost on the sunlit face and its condensation on the night side could produce supersonic winds which decelerate through a hydraulic jump. The hydraulic jump has been reproduced by the rarefied gas flow model of Austin and Goldstein (2000). The solution is found to be very sensitive to the temperature of the frost at the subsolar point which was a key unknown at that time. Ingersoll (1989) later investigated the effects of the patchy nature of the SO_2 frost to accommodate the nonuniform surface properties found in observations. Ingersoll (1989) proposed that an area of length scale $L = \sqrt{2\pi}H/\alpha$, where H is the scale height and α is the SO_2 sticking coefficient, would determine its own atmospheric pressure if the surface is cold and frost is present. This essentially gives the influence length scale of a sublimation atmosphere.

The model of Ingersoll *et al.* (1985) is modified in Ingersoll (1989) to be simple enough to allow the solutions to be in closed analytical form, and is also versatile enough such that two kinds of sources, sublimation and volcanic venting, can be treated equivalently with the volcanic venting modeled as a source of mass distributed over an assumed area covered by a plume.

Moreno *et al.* (1991) developed numerical models based on the conservation equations of inviscid, compressible gas dynamics to simulate both sublimation and volcanic atmospheres. The improvement of their model as compared to Ingersoll (1989) is the 2-D axisymmetric nature of the model. In common with Ingersoll (1989), they found that the sublimation atmosphere is a dynamic one, and the flow becomes supersonic as it expands away from the subsolar point; the sublimation SO_2 atmosphere does not extend to the nightside assuming a surface sticking coefficient of one, and the nightside SO_2 atmosphere is thus only of volcanic origin. However, due to the inviscid nature of their model, there are no shock waves in the sublimation atmosphere, and as they pointed out, their continuum approach is not valid far from ($\theta > 80^o$) the subsolar point. Such breakdown in the continuum theory becomes more severe in their Pele-type volcanic atmosphere simulation since the plume flow quickly becomes free-molecular away from the vent vicinity (as will be shown in this dissertation). Additionally, no apparent canopy-shaped shocks are found in their volcanic atmosphere, and a re-entry shock is present even in their nightside volcanic atmosphere with assumption of SO_2 surface sticking coefficient of one. As will be shown in this dissertation, these results are not consistent

11

with our volcanic plume modeling. With the same assumption of SO_2 surface sticking coefficient of one, we found that the down-falling gas in a nightside volcanic plume simply pours onto the surface and condenses unimpeded. The down-falling gas flow in our result is virtually a free-molecular one which cannot be simulated by Moreno's model. A re-entry shock does appear in the dayside volcanic atmosphere in our results as in theirs. However, there are still appreciable qualitative differences between the re-entry shocks in our and their results: the re-entry shock in our result is purely due to the interaction of the down-falling plume gas and the dense sublimation atmosphere at relatively high surface temperatures, and is nearly horizontal at an altitude close to the surface; the shock in their results may be partly due to the continuum nature of the model in addition to the interaction of the down-falling plume gas and the sublimation atmosphere.

Ingersoll *et al.* (1985), Ingersoll (1989) and Moreno *et al.* (1991) did not include heating mechanisms of the atmosphere such as solar UV and IR, plasma and Joule heating. Neither did they include the radiative cooling effects of SO_2 except that Moreno *et al.* (1991) incorporated a crude radiative transport model in which both the radiative cooling of the atmosphere and the heating of the atmosphere by the surface is taken into account assuming blackbody emission with certain emissivity. Among the early detailed numerical investigations of heating and cooling of the Ionian atmosphere are Lellouch *et al.* (1992), Strobel *et al.* (1994) and Wong and Johnson (1995). Lellouch *et al.* (1992) examined models of one dimensional atmospheric profiles sub-

ject to different assumptions about heating from a plasma bombardment of the exosphere but still could not explain the hot (200 – 600 K) localized atmospheric temperature inferred from millimeter observation. The focus of Strobel *et al.* (1994) is to find the heating mechanisms that could explain this hot atmospheric temperature of 200 – 600 K and the relatively warm bulk atmospheric temperature (200–400 K) derived by Ballester *et al.* (1994) based on HST observation. These temperatures should be compared to the temperature of $\sim$140 K of the first scale height. Strobel *et al.* (1994) developed a radiative-thermal conduction model with different heating mechanisms and near-IR (infrared) and non-LTE cooling by SO_2 ν_1, ν_2 and ν_3 and rotational lines, and found that Joule heating is the dominant heating mechanism in the sub-nanobar regions of Io's atmosphere and the asymptotic thermospheric temperature can attain a value as high as 1800 K. However, the model of Strobel *et al.* (1994) is one dimensional in the vertical direction so that the effect of the dynamical nature (supersonic sublimation-driven flow or volcanic activities) of the atmosphere on the temperature profile cannot be evaluated. A 2-D dynamical model with plasma and solar UV heating and IR cooling was developed by Wong and Johnson (1995). The model of Wong and Johnson (1995) is similar to that of Moreno *et al.* (1991) except that the plasma and UV heating is added, and is more adequate than that of Strobel *et al.* (1994) in that the dynamical nature of the atmosphere is included. The focus of Wong and Johnson (1995) is to study the effect of plasma heating on the dynamics of a sublimation-driven atmosphere near the exobase. They found that plasma

heating significantly inflates the upper atmosphere and increases the exobase altitude, and the dynamical nature of the atmosphere, particularly the horizontal flow, is also important in determining the exobase altitude. Unlike Strobel *et al.* (1994), Wong and Johnson (1995) used a thermal-dynamic equilibrium cooling model instead of a more appropriate non-LTE cooling model for IR cooling, and did not include SO_2 ν_1, ν_2 and ν_3 vibrational bands cooling and Joule heating. The incorporation of non-LTE cooling and Joule heating is done later in Wong and Johnson (1996) which also added photochemistry of SO_2 aimed at approximating the abundance of minor species in Io's atmosphere. Even with more detailed heating and cooling mechanisms in their dynamical model (Wong and Johnson 1996), the picture remains inaccurate and incomplete because they use a continuum semi-viscous (vertical direction only) model whereas rarefaction effects can be important especially near the exobase. In addition, the volcanic plume flow is neglected in Wong and Johnson (1996). It should be noted that one of the results of this work is that when both a sublimation atmosphere and a volcanic plume are present at the same time, the plume may rise well above the sublimation atmosphere exobase, and extends laterally quite far via gas "bounces" and blankets the sublimation atmosphere. Therefore, the interaction of the upper atmosphere from volcanic plumes with the plasma and radiation from space must also be studied.

Austin and Goldstein (1995) presented the first rarefied gas dynamic model (Direct simulation Monte Carlo, DSMC) for the numerical simulation of the Ionian atmosphere. They examined the nature of the shocks which de-

velop in the volcanic plumes and how the plumes expand in the presence of a background non-condensible gas. Austin and Goldstein (1998) also presented the first DSMC simulations of a sublimation/condensation driven circumplanetary flow as well as high spatial resolution modeling of a volcanic plume. Heating due to plasma bombardment is modeled using a modification of the time-splitting method ("overlay" technique). The absorption of plasma energy is integrated cell-by-cell from the top of the domain down to the surface in each column of cells while the gas flow field is held frozen (the velocity of the plasma particles is much greater than that of an atmospheric gas molecule). The energy deposited in a computational cell is evenly divided among all the molecules in the cell and is further evenly divided between the translational and rotational energy modes (assuming a locally equilibrium distribution). Translational energy is distributed to the molecules in proportion to the difference between the speed of each molecule and the average molecular speed in the cell. Using this method the average (bulk) flow velocity remain unchanged. The plasma particle momentum is not transferred to the atmospheric particles and vibration, dissociation, and electronic excitation were neglected. A simple form of non-LTE infrared radiation from the SO_2 rotational levels was also incorporated. The cooling is based on a simplified model of Lellouch *et al.* (1992) which assumes an optically thin gas.[1] The effects of solar UV and Joule heating and photochemistry of SO_2 were not included. Austin and

---

[1]However, the effect of the failure to include "hot band" transition in the model in Lellouch *et al.* (1992) must be investigated in the future.

Goldstein (2000) later used this model and presented detailed calculations of sublimation/condensation driven flows including parametric studies of surface temperatures, the amount of non-condensible background gas, and energy input from the plasma bombardment of the upper atmosphere. The emphasis of that work is on the atmospheric structure and the effect of different parameters on the observable frost deposition. They found that the atmospheric flow is rarefied everywhere except near the surface in the subsolar region. In common with Ingersoll (1989), they also found that a standing shock is formed near the terminator. Similar to the results of Wong and Johnson (1995), a dramatically inflated upper sublimation atmosphere is seen due to plasma heating. The model of Austin and Goldstein (2000) simulates the rarefied conditions better and, thus, should more accurately predict various flow features such as the thermal structure of the sublimation atmosphere, the standing shock location, exobase altitude and so on.

2.3 Recent Development in both Observations and Numerical Study

Our understanding of Io's atmosphere has improved substantially due to recent observations and theoretical analysis. The importance of the role of volcanoes in generating and maintaining Io's SO_2 atmosphere has been emphasized. Geissler *et al.* (1999) examined the Galileo imaging of atmospheric emission from Io and tested the association of blue equatorial glows with specific volcanic plumes. Strobel and Wolven (2001) found that only eight Pele-type

volcanoes would be needed to account for the SO_2 abundance inferred from reflected solar Lyman-α intensity data. Thus, they suggested that, in addition to a sublimation atmosphere, volcanic plume atmospheres may also contribute substantially to the overall atmosphere. As discussed in the preceding section, a surprisingly hot (200–600 K) localized atmospheric temperature relevant to the first scale height (40 km) is inferred from millimeter observation if a hydrostatic atmosphere is assumed (Lellouch et $al.$ 1992). Although Strobel et $al.$ (1994) found that Joule heating is the dominant heating mechanism in the sub-nanobar regions of Io's atmosphere and the asymptotic thermospheric temperature can attain a value as high as 1800 K, the profile still cannot explain the high temperature in the first scale height. However, as pointed out by Ballester et $al.$ (1994), the width of the rotational lines ($\sim$600 kHz at 220 GHz, Lellouch et $al.$ (1992)) is equivalent to a gas velocity of about 0.8 km/sec, which falls exactly in the range of the ejection velocity of the volcanic plumes, as inferred from their height in the Voyager images (0.5 – 1 km/s Strom and Schneider (1982)). Therefore, Lellouch (1996) used a ballistic model to simulate volcanic plumes and interpreted the millimeter data to obtain a column density near the plume center of $\sim 10^{18}$ cm^{-2} and the average column density over the plume of $\sim 10^{16}$ cm^{-2}, which agree better with that derived by Strobel and Wolven (2001), Feldman et $al.$ (2000) and McGrath et $al.$ (2000). The existence of a sodium cloud surrounding Io requires an atmospheric source other than sublimation of frost since the vapor pressure of NaCl is extremely low. Active volcanoes must be considered. Moses et $al.$

17

(2002a) used a one-dimensional model including chemical kinetics and diffusion to simulate the photochemical processing in Pele's volcanic gas. They found that NaCl, Na, Cl, KCl, and K will be the dominant alkali and chlorine gases in atmospheres generated from Pele-like plume eruptions on Io. Lellouch *et al.* (2003) also investigated the possibility of volcanically emitted sodium chloride as a source for Io's neutral clouds and plasma torus, and suggested that the volcanic emissions provide important sources of Na and Cl.

Dynamic volcanic plume models are essential to efforts to link the plumes to the various observations mentioned above. However, such dynamic models are quite complex (Kieffer 1982, Lellouch 1996). Crude plume models have been used in many interpretations of observation data. A ballistic plume with a uniform gas temperature is used in the interpretation of millimeter wave data of Lellouch (1996). As will be discussed below, the thermal motion of individual particles and their collisions are not taken into account in a ballistic model so that the resulting flow field does not reflect features such as shocks or the acceleration and cooling of the gas through expansions which should occur at certain locations. As will be shown in this dissertation, the assumption of a uniform gas temperature is especially poor. This can be seen from the large variation in the gas temperature in a Pele-type plume. The one-dimensional diffusion model used by Moses *et al.* (2002a) neglected the plume dynamics and could not produce a shock at high altitude. Therefore, the sodium densities they obtained seem to be too high at high altitude as compared to the observations by Schneider *et al.* (1991a). If one accounts for the rapid slowing

of the upward moving SO_2 and entrained sodium through the canopy shock, the observed low sodium number density at high altitude (Schneider *et al.* 1991a) may well be reproduced. Various models from Stochastic-Ballistic to computational fluid dynamics (CFD) to rarefied gas dynamics have been developed and adopted for dynamical studies of volcanoes as summarized in the preceding section and also recently by Douté *et al.* (2002). Unfortunately, as already discussed, these models are physically different and sometimes internally inconsistent. The Stochastic-Ballistic (SB) model can satisfactorily reproduce the plume shape and ring deposition of some plumes by careful manipulation of the initial conditions. However, the thermal motion of individual particles and their collisions are not taken into account in a SB model so that the resulting flow field does not show features such as shocks or the acceleration and cooling of the gas through expansions which should occur at certain locations. We believe that the SB model is not suitable for the simulation of the gas flow, and the constraints it places on the initial conditions are not accurate. Continuum flow models have limited applicability because of the wide-range of flow regimes occurring in plumes. Conditions range from a virtually continuum flow close to the vent to free-molecular flow far from it. The continuum assumption breaks down in low-density flows because the mean free path of molecules becomes comparable to the length scale of flow features which invalidates the continuum flow approximations. The difficulties posed by the Stochastic-Ballistic and continuum flow models are overcome by the direct simulation Monte Carlo (DSMC) approach (Bird 1994) which has

been adopted and applied to volcanic plume modeling by Austin and Gold-stein (1995, 2000). We have followed this approach and developed our gas dynamic, radiation and gas/particulates flow model based on it (Zhang *et al.* 2001, 2003a, 2003b, 2003c, 2004, Moore *et al.* 2003).

One important uncertainty for the plumes is the temperature of the gas as it leaves the vent. A wide variety of reservoir conditions have been postu-lated yielding a wide range of gas temperatures at the vent ranging from less than 300 K to as high as 1400 K, depending on reservoir conditions (Kieffer 1982). Recent observations have suggested that the magma temperature at Pele may exceed 1700 K (Lopes-Gautier *et al.* 2002). Using two-temperature fits to the Galileo Near-Infrared Mapping Spectrometer (NIMS) spectra for Pele at night-time, they obtained the temperature for the hot component of 1760 $\pm$210 K suggesting that the Pele caldera has small areas where lavas are at temperatures consistent with ultramafic compositions. Zolotov and Fegley (2001) calculated a total vent pressure for Pele of 0.01 to 2 bars at a vent temperature in this range (1760$\pm$210 K). These are drastically different from the vent conditions (T of 650 K and P of $\sim$40 nanobar) that we used to repro-duce the plume shape of Pele and the vertical column density observed around Pele. However, this large difference may be reconcilable if the precise defini-tion of a "vent" is distinguished for the different studies as will be explained in the present work. The concept of an "virtual" vent makes our simulation applicable to various types of possibly complex volcanic sources. In fact, the sources of volcanic eruptions on Io are quite complicated. As suggested by

Kieffer *et al.* (2000), Prometheus is likely caused by molten lava impinging on a thick SO_2 frost field. Douté *et al.* (2002) proposed at least three sources of vent material for Prometheus: the interaction of flowing lava and preexisting volatile deposits on the surface, direct degassing from the lava, or the eruption of a liquid aquifer from underground.

As already discussed in Section 2.1, many Ionian volcanoes manifest themselves by particulates rising high above the surface and many observable features of Ionian volcanic plumes are associated with the fine particulates in these plumes. Most of the Voyager and Galileo plume images likely show sunlight scattered by particles (possibly snow-flakes, droplets and/or dust) entrained in the plumes. Photometric studies of Loki by Collins (1981) indicate that particles of various sizes (from 0.01 μm up to 1000 μm) are present. Strom and Schneider (1982) suggested that the bright envelope appearing in the smoothed ultraviolet brightness images of Pele may be the result of a concentration of particles at a shock front. The wavelength dependence of the optical depth in 1996 HST observations of Pele can be matched by either a plume of SO_2 gas having an average column density of $\sim 3.7 \times 10^{17} cm^{-2}$ or a plume of very small scattering particles with maximum size of 0.08 μm (Spencer *et al.* 1997). Thus, it is important to study the behavior of gas/particle flow in these volcanic plumes once the gas dynamic model has been developed; such a gas/particle flow model enables one to better understand the observed plume images. Meanwhile, the deposition patterns around Prometheus are among the most dramatic features on Io and have attracted much attention.

Douté *et al.* (2002) obtained maps of SO_2 areal abundance and mean grain size around Prometheus, and used a semiempirical ballistic model to examine the progressive emplacement of the SO_2 ring. Geissler *et al.* (2003) suggested that there is a multiple ring structure around Prometheus with the radii of these ring deposits centered at 72 km (bright yellow), 95 km (dark), 125 km (white), and 200 km (a faint yellow ring that becomes prominent at high solar phase angles). This remarkable multiple ring structure around Prometheus is demonstrated in Fig. 2.1.
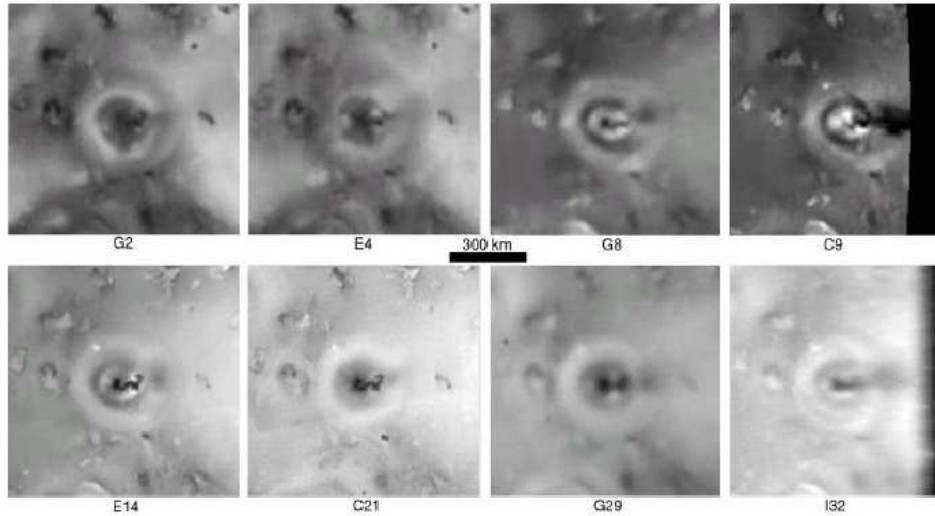
Figure 2.1: Surface change at Prometheus. (*From Geissler et al. (2003), courtesy of P. Geissler*).

Ingersoll (1989) pointed out that "the key unknowns for Io are the strength of the volcanic sources and the temperature of frost near the subsolar point". The recent Galileo PPR observation (Rathbun *et al.* 2003) gives a

better understanding of subsolar surface temperature. They obtained a subsolar surface temperature of $\sim$133 K based on the Galileo Photopolarimeter-Radiometer (PPR) observation. However, the relative significance of volcanic/sublimation atmosphere is still controversial. In an analysis of HST UV spectra of Io's Prometheus plume and adjoining low- to mid- latitude region, Jessup *et al.* (2003) suggested that "at least on the anti-Jovian hemisphere where there are extensive deposits of optically-thick SO_2 frost, the atmosphere is primarily supported by vapor pressure equilibrium with surface frost". However, it should be pointed out that extensive deposits of optically-thick SO_2 frost is not a sufficient condition for the atmosphere to be supported by vapor pressure equilibrium with surface frost since the time of the day is also important. A frost without solar irradiation could not generate any significant sublimation atmosphere so even if the anti-Jovian hemisphere has extensive frost coverage it cannot be the main source of the atmosphere when it is on the night side. As suggested by Ingersoll (1989) and Moreno *et al.* (1991) since the sublimation SO_2 atmosphere does not extend to nightside, the only significant atmosphere there is within plumes. We believe that the sublimation atmosphere is only significant on the dayside and probably only around the subsolar point. It will be shown in this dissertation that although the column density is dominated by the sublimation atmosphere $\sim$100 km away from the vent, the plume rises way above and blankets the sublimation atmosphere. The plume gas shows dramatic dynamic features such as canopy and re-entry shocks and bounces. Therefore, even when both sublimation atmo-

sphere and volcanic plume are present at the same time and the sublimation atmosphere dominates the value of the column density, volcanic plumes may still play an important role in determining atmospheric properties like its inferred temperature and its interaction with the plasma and radiation from space. Thus, one must be specific when discussing the relative significance of volcanic/sublimation atmospheres. The particular aspect one is interested in – temperature, column density or atmospheric composition etc., and the particular location – near major volcanoes or far, dayside or nightside, upper atmosphere or near surface, frost rich or depleted region determine the relative contributions of the two sources of atmospheric gases.

Chapter 3

Numerical Methods

An important feature of volcanic plume flows on Io is the wide range of flow regimes present, from a virtually continuum regime near the volcano vent (number density of the order of 10^{17} molecule/m^3 with a vent diameter-based Knudsen number[1] of the order of 10^{-4}) to the free molecular regime at high altitude, with transitional flow in between. The Direct Simulation Monte Carlo (DSMC) method (Bird 1994) is the most suitable choice to model such flows. In DSMC the flow is represented by a large number of simulated particles which are moved and collided. The collisions between particles are simulated stochastically based on the kinetic theory of a dilute gas rather than deterministically as in molecular dynamics. Flow properties such as temperature and density are extracted by sampling and averaging over all the molecules. The collision model used in our DSMC method is the variable hard sphere (VHS) model with necessary parameters chosen for SO_2 molecules from (Bird 1994).

Use of the DSMC method has the advantage that it is relatively easy to include internal molecular energy modes and a wide variety of physical mech-

---

[1]Kn=λ/d, where λ = a gas molecule mean free path and d = the characteristic linear dimension.

anisms such as chemical reaction and thermal radiation, without substantially changing the computational algorithm. This advantage will be demonstrated below. However, computational challenges may arise too. For instance, The time steps required sometimes change dramatically from process to process. In the present work, when necessary, the computational domain is split into subdomains with different time steps and cell sizes. Radial cell-based weights are used in each subdomain for our axisymmetric problems.

The innovations we have incorporated in our DSMC method include the spherical geometry, the consideration of a body force (gravity), SO_2 internal energy exchange, radiation from rotational lines and discrete vibrational bands (aimed at connecting the gas dynamic simulation to the radiation signature of the plumes by remote sensing), multi-domain calculations to resolve radiation in the vent vicinity, gas opacity, and "overlay" gas/particle flow modeling. The model has reproduced the observed plume shape, ring deposition and some other features, and appears to be reasonably successful in simulating the plume flow and matching observations (Zhang *et al.* 2003a, 2003b, 2004).

3.1   Flow Conditions

The flow conditions and DSMC procedure used in the simulation of the plume flow are shown schematically in Figs. 3.1a and b. The flow is assumed to be axisymmetric and emerging at a uniform mean upward velocity (V_v) from a circular vent centered at the origin of the symmetry axis. As will be discussed in Chapter 6, the vent in our simulation is interpreted as
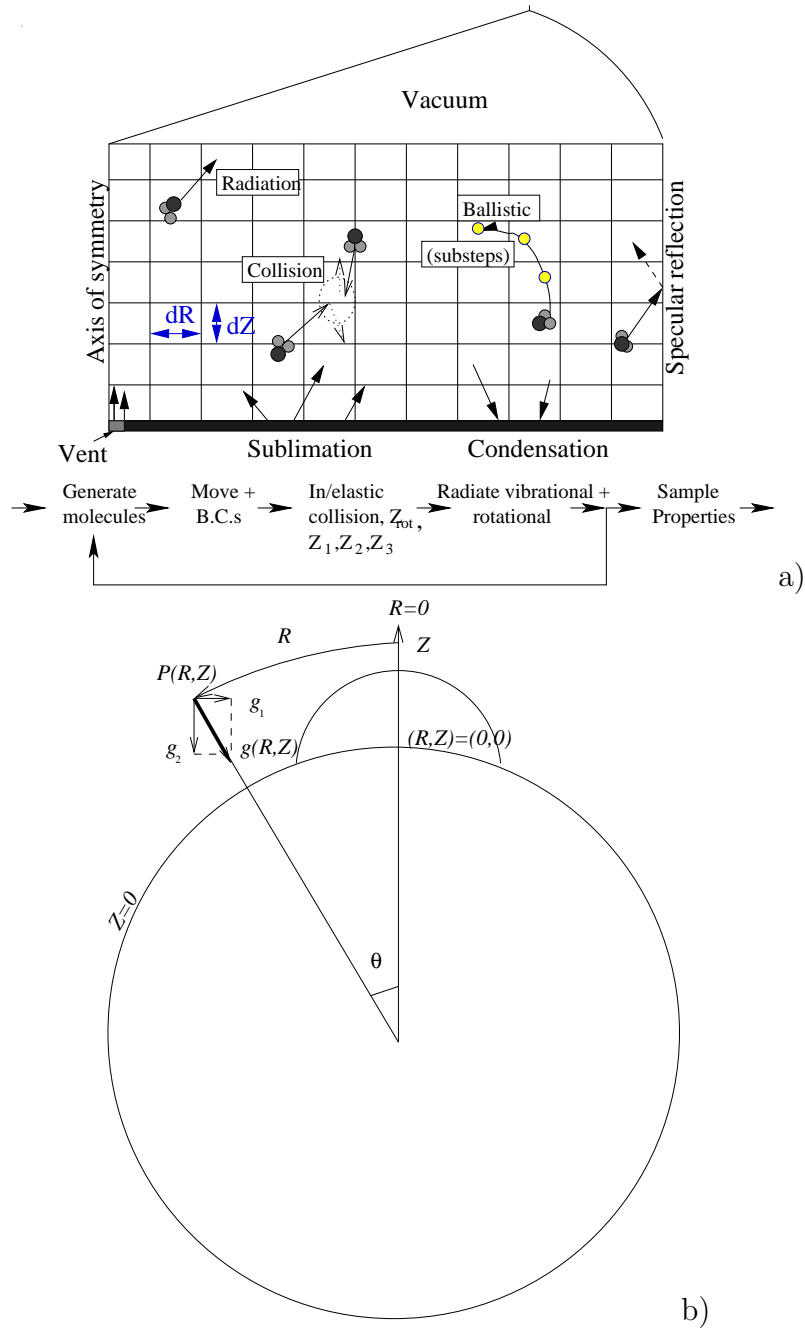
Figure 3.1: Schematic diagrams of the computational domain and computational procedures.

27

the "virtual" vent which represents the location where the gas temperature and velocity reach the modeled values. Therefore, our virtual vent may not necessarily be right at the exit of a volcanic tube and may apply to plumes having a lava-frost interaction as the source. The nominal vent radius is ~8 km. The effects of vent size are examined in Chapter 5. The molecules also have random thermal velocities sampled based on Maxwellian distribution at the vent temperature (T_v), and carry equilibrium rotational and discrete vibrational energy. A uniform velocity profile is reasonable at these relatively high Reynolds numbers ($\sim 5 \times 10^4$) if one assumes pipe-like flow out of a relatively straight subsurface conduit. The effect of other velocity profiles, *e.g.* parabolic profile, and source mechanisms, *e.g.* lava-lake or lava-frost interaction, at the vent are also examined and will be discussed in Chapter 5. The gas jet is assumed to be pure SO_2 because it has been the most frequently identified molecular species in Io's atmosphere and is thought to be the primary atmospheric component and the driving gas for most of the volcanic plumes (Pearl *et al.* 1979, Ballester *et al.* 1994, Lellouch 1996). The effects and transport of other species have also been investigated recently and will be presented in Chapter 5.

In early work (Zhang *et al.* 2003a, 2003b) a flat planet approximation was used. This is most appropriate for plumes which are small compared to the radius of Io. More recently, the spherical geometry was accounted for. The coordinates are interpreted in the manner shown in Fig. 3.1b. The altitude Z is interpreted as the distance from the spherical surface of Io, and the radius
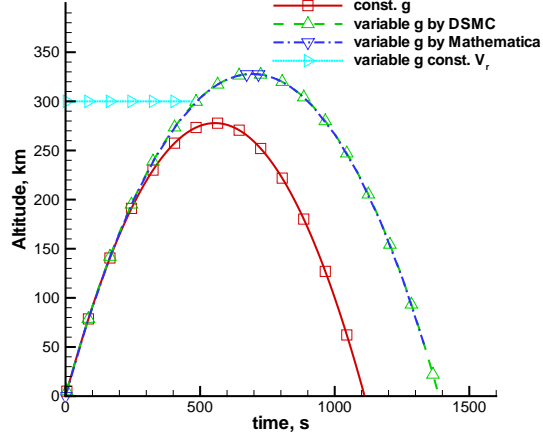
Figure 3.2: Comparison of altitudes of particle as a function of time calculated with constant and variable g.

R is interpreted as the length of the arc of a circle with the origin at Io's center and a radius r of the distance from the point of interest to the center of Io $(R_0 + Z)$, where $R_0 = 1800$ km is the radius of Io. The surface of Io corresponds to $Z = 0$ km, and the plume axis (also passing through the center of Io) corresponds to $R = 0$ km. The volume of each cell is $r^2 sin(\theta)\mathrm{d}r\mathrm{d}\phi\mathrm{d}\theta$ $= r^2 sin(\theta)\mathrm{d}Z\mathrm{d}\phi\mathrm{d}\theta$, where θ is the zenith angle as indicated in Fig. 3.1b and equal to R/r, and $\mathrm{d}\phi$ is set to unity.

The gas is subject to Io's gravitational field after it erupts from the vent. The altitude and direction dependence of the gravitational acceleration has also been included since it was recently found that, for large Pele type plumes, this dependence has a noticeable influence on the trajectory of the molecules and thus affects the plume shape. This can be illustrated by the

comparison of the trajectories (Fig 3.2) of two free flying molecules in two different gravity fields: one in a constant gravity field with $g_0 = 1.8$ m/s^2 evaluated at the surface and the other in an altitude dependent $g(Z) = g_0(\frac{R_0}{r})^2$. The two molecules initially move upward normal to the surface at the same velocity of 1000 m/s. Due to the smaller gravity force at high altitude, the molecule moving in the variable gravity field rises ∼20% higher. Note that our new DSMC model was validated by comparing the trajectory calculated in DSMC to an independent calculation by Mathematica that is also shown in Fig. 3.2. In addition, the calculation of the motion and the indexing of the molecules in the new DSMC model with spherical geometry has been checked by calculating the trajectory of a molecule released at an altitude of 300 km with orbital velocity. The horizontal line segment in Fig. 3.2 shows that the particle orbits at constant altitude as expected. The effect is further shown for simulated Pele type plumes in Figs. 3.3a and b. Note the greater height and width of the plume in the variable gravity field. Also note that the two plumes compared use the flat surface approximation.

For the convenient calculations of inter-molecular collisions in DSMC, the molecules are moved in a Cartesian coordinate system (x_1, x_2, x_3) with corresponding accelerations $(g_1, g_2, g_3) = (-g(r)sin(\theta), -g(r)cos(\theta), 0)$, where $g(r) = g_0(\frac{R_0}{r})^2$. The coordinates of the molecules are then transformed back to spherical coordinates for indexing. As shown in Fig. 3.4, neither the spherical geometry nor the position dependence of the gravity force are significant for small Prometheus type plumes (with plume height of less than ∼80 km) espe-

a)
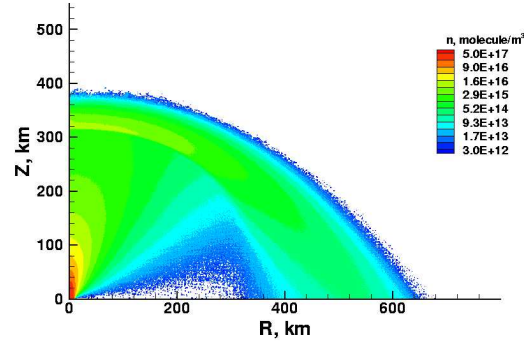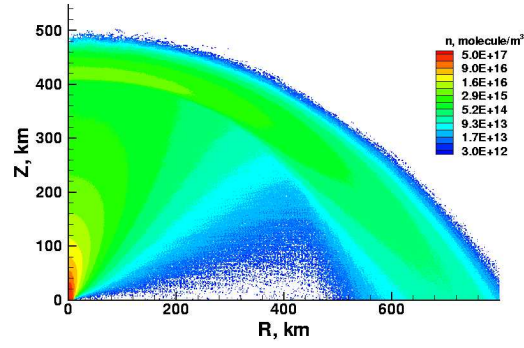
b)

Figure 3.3: The number density contours of simulated plume with a) constant g and b) variable g. Note the same vent conditions (T_v of 650 K and V_v of 1000 m/s) and the same axes for the two plumes shown.
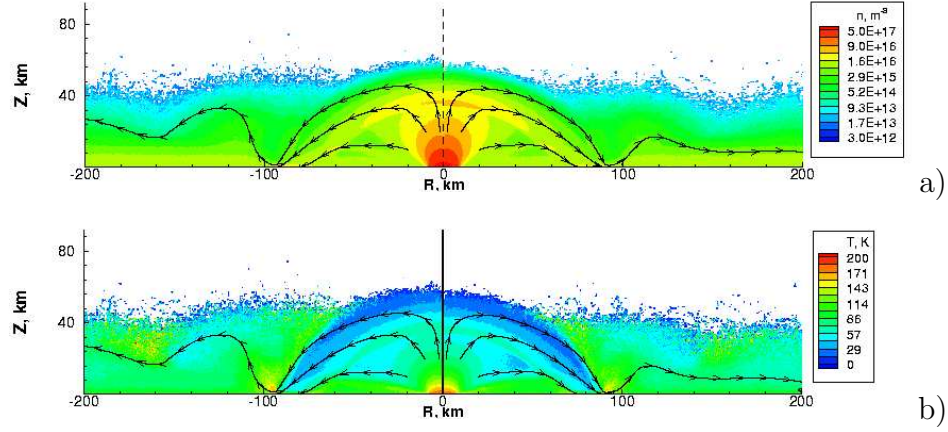
Figure 3.4: a) The number density and b) temperature contours of simulated Prometheus type plumes with (left) constant g and flat geometry and (right) variable g and spherical geometry. Note the same vent conditions (T_v of 180 K and V_v of 200 m/s) and the same nominal surface temperature of 110 K for the two plumes shown.

cially inside the main plume. Therefore, some of the early simulation results (with flat surface approximation and constant gravity field) associated with Prometheus type plumes are still used in the discussion in the present work without invalidating the conclusions.

The molecules escape into space if they cross the upper boundary of the computational domain (rarely), and are reflected by the outer specular wall when they collide with the circumferential boundary. The assumption of a specular wall at the outer boundary is not accurate. However, it appears to be the best choice since a vacuum boundary will introduce artificial outflow of the sublimation atmosphere. A hydrostatic pressure boundary or a zero gradient boundary is not appropriate due to the dynamic nature of the sublimation

32

atmosphere especially when it interacts with the volcanic plume. Most importantly, we will show in the next chapter that when the specular outer wall is placed at a sufficient distance from the vent it has no effect on the flow in the regions of interest. The surface of Io is assumed to be very rough and have a sticking coefficient of $\alpha = 1$ so the molecules condense when they contact the surface. On the other hand, the surface sublimates vapor and the sublimated molecules are emitted randomly into a hemisphere at a rate specified by the equilibrium vapor pressure at the surface temperature. Note that although other combinations of sticking coefficient and sublimation outflux are possible, our treatment of sublimation/condensation model is greatly simplified by assuming sticking coefficient of 1 regardless of surface temperature. This assumption is quite realistic at surface temperature of less than 110 K (Sandford and Allamandola 1993). Moreover, it produces the correct equilibrium vapor pressure and a suitable gas outflux from the ice into a near-vacuum when the outflux should be independent of the influx. It is understood that in reality α depends on internal and translational energy of the incident molecule, impact angle, surface temperature and surface structure. Similarly, the distribution of sublimated molecules may depend on the incident stream as well as surface details. However, detailed knowledge of these dependences is lacking, and, hence we would have to make assumptions about these variations if they were to be included in the model. Moreover, engineering simulations in other contexts have shown that details of this nature generally do not alter the mean flow appreciably.

3.2 Internal Energy Exchange and Radiation Modeling

The modeling of IR radiation requires knowledge of the spatial distribution of the vibrational and rotational populations of SO_2. Translational-internal energy transfer as well as spontaneous emission processes must be modeled. In our early simulations, it was usually assumed that the densities are sufficiently low that the effects of re-absorption of plume emission on the vibrational and rotational population may be ignored. This assumption was confirmed for the three vibrational bands by the absorption calculation in Zhang *et al.* (2003a). The results there show that gas density at least one order of magnitude higher is needed before the effects of re-absorption of vibrational bands emission need to be considered. The optically thin assumption for rotational lines in the vicinity of the vent is not accurate. However, the total rotational emission is generally one order of magnitude smaller than that from the vibrational bands in the vent vicinity and, thus, the opacity at the rotational lines does not have a significant effect on the plume dynamics. The effect of opacity will be further discussed in Chapter 5. Note that we currently do not consider the radiative heating of the gas by surrounding hot lava. However, the radiative heating of the surface by the gas is examined.

3.2.1 Internal Energy Exchange

The modeling of rotation-translation (RT) energy transfer during collisions between SO_2 molecules is performed using the Larsen-Borgnakke method, and a discrete version of the method is used for vibration-translation (VT) en-

ergy transfer (Larsen and Borgnakke 1974, Bergemann and Boyd 1994). The Larsen-Borgnakke method is a phenomenological method and the most frequently used approach in the modeling of internal energy transfer. In this method post-collision internal energies are assumed to be distributed according to the local equilibrium distribution functions. It has been shown (Bird 1994) that it is not necessary for the total collision energy to include the energy of all modes that are to be subject to redistribution in the collision in the Larsen-Borgnakke method. A succession of redistributions, each of which involves only a single internal mode and the translational mode, can thus be used. Since SO_2 molecules have three vibrational modes, advantage has been taken of this serial consideration of each mode in our DSMC model. The reason for treating the vibrational energy in a quantum fashion is that the vibrational levels are widely spaced, and at the relatively low temperatures of present interest the vibrational modes can not be regarded as being fully excited.

Special effort has been placed on modeling the unique VT relaxation process of SO_2 molecules. Those relaxation processes are discussed extensively in (Lambert and Salter 1957, Bass *et al.* 1971, Lambert 1977). Experimental ultrasonic dispersion data in gaseous sulfur dioxide (Lambert and Salter 1957) show a double relaxation process. One process, hereinafter called process one, corresponds to the lowest mode ν_2 (for the band center at 518 cm^{-1}), and the other (process two) corresponds to the combination of the ν_1 (1151 cm$^-$1) and ν_3 (1361 cm^{-1}) vibrational modes. It has been suggested (Bass *et al.* 1971)

35

that, for process two, the collision relaxation number, Z_2, defined as the average number of intermolecular collisions necessary for a molecule to lose one quantum of vibrational energy, follows the Landau-Teller temperature dependence of collision number, which predicts $\log(Z_2) \propto T^{-1/3}$ for gas temperature T (Fig. 3.5). In contrast, the collision relaxation number for process one, Z_1, does not follow the Landau-Teller temperature dependence but reaches a maximum around T = 350 K due to preferential orientation requirements in low-temperature collisions.

In DSMC, the collision relaxation number (Z_v) is defined as the average number of inter-molecular collisions during a time interval that is equal to the vibrational relaxation time (Bird 1994), while the collision number Z in Bass *et al.* (1971) is defined as (Lambert and Salter 1957),

$$Z = Z_c \beta (e^{-h\nu/kT} + 1) = Z_v(e^{-h\nu/kT} + 1) \tag{3.1}$$

where Z_c is the number of collisions one molecule suffers per second (collision frequency), ν is the frequency of the vibrational mode, and β is the relaxation time for that mode. Therefore, Z_v and Z are different by a factor of $(e^{-h\nu/kT} + 1)$. For the ν_2 vibration mode, constant values of Z_1 (Fig. 3.5) of 300 and 158 are used for temperature less than and greater than 800 K, respectively, based on the work of Bass *et al.* (1971). Using Eqn. 3.1, the DSMC collision relaxation number for this mode Z_{v,ν_2} is therefore $Z_1/(e^{-h\nu/kT} + 1)$. The temperature dependence of Z_2 for the other two modes is based on a curve fit (Z_2 in Fig. 3.5) to the experimental data of Bass *et al.* (1971) and is

36
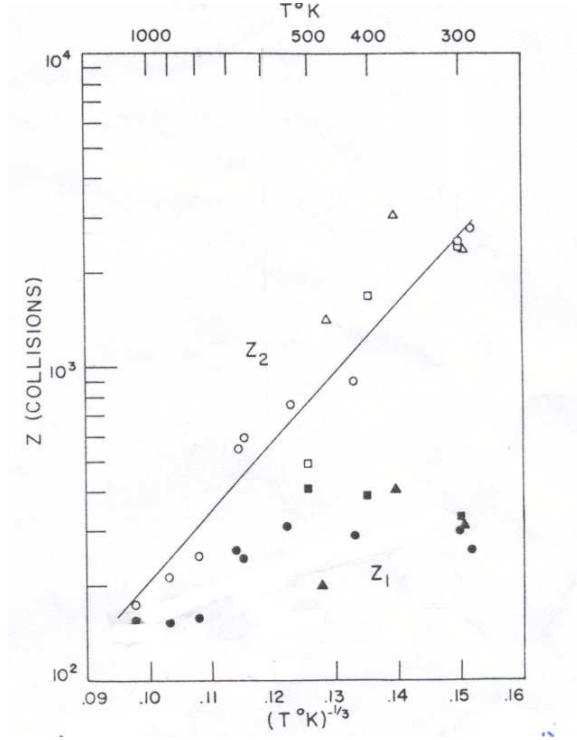
Figure 3.5: Experimental data of the collision number Z_{10} for SO_2 vibration relaxation. (Adapted from Bass *et al.*, 1971.)

expressed as,

$$Z_2 = e^{(50.T^{-1/3}-0.097)+5.19} = 163e^{50.T^{-1/3}} \tag{3.2}$$

and the DSMC collision relaxation number for these two modes, $Z_{v,\nu_{1,3}}$, is obtained by dividing this equation by $(e^{-h\nu/kT} + 1)$, where ν is the frequency of the ν_1 or ν_3 vibrational mode.

Note that the present model of VT relaxation of SO_2 molecules is more accurate than our early model of Zhang *et al.* (2003a). As will be discussed in Appendix A, the old and new VT relaxation models produce very similar

results both qualitatively and quantitatively. Thus, the results are discussed without specifying whether they are obtained from old or new VT relaxation model. However, it is worth pointing out that, unless otherwise specified, all the plume results in Chapter 4 are simulated with the old VT relaxation model. The new model was used for most of the rest of the results in the present work.

3.2.2   Radiation Modeling

There is non-LTE cooling by spontaneous emission from the three vibrational bands of SO_2. Thermal radiation occurs as a result of radiative transitions between the internal energy levels of molecules, and the probability per unit time for a molecule to spontaneously emit is specified by the Einstein coefficient, A_{nm}, for the transition $n \rightarrow m$. These coefficients have been found for the $1 \rightarrow 0$ transition of the ν_1, ν_2 and ν_3 bands to be 3.5, 0.88 and 44 $\sec^{-1}$, respectively (Radzig and Smirnov 1980). The radiation due to $n \rightarrow n-1$ transitions from higher (up to the third level) vibrational levels was incorporated recently and it is assumed that $A_{n \rightarrow n-1} = nA_{1 \rightarrow 0}$ (Penner 1959).

The rotational (microwave) cooling model of Lellouch *et al.* (1992) was originally used to calculate the microwave radiation from the gas (Austin and Goldstein 2000). In this model, the cooling rate R per molecule is given by $R = 4\pi\Sigma_j B_{\nu_j} S_j$ as an a priori function of temperature, where B_ν is the Planck function and S_j is the line strength of the jth rotational line. Lellouch *et al.* (1992) did not provide a detailed derivation of this cooling rate. A detailed

explanation of this model is presented in Appendix B. We recently discover an error in the results of Lellouch *et al.* (1992). The Hitran atmospheric data base was used in their calculations and the error arises because Hitran only lists the rotational transitions in the vibrational ground state (Varghese 2003, private communication). This leads to significant errors in SO_2 emission calculation at higher temperature ($\sim$70% at 700 K). We performed a detailed line-by-line calculation for HCN since it is a linear molecule with a simple spectrum, and verified that a simple analytical correction can be used for Hitran-based emission calculations. We also show that our result has the correct classical limit for a rotating dipole of a quadratic temperature dependence. The near quadratic temperature dependence in which $R[Js^{-1}/SO_2] = 1.744 \times 10^{-28}T^{2.043}$ by the model of Varghese (2003) is used for SO_2 rotational emission in the present work. Details are also provided in Appendix B.

In summary, we have recently improved our early model by including the spherical geometry, the variable gravity field, the new VT transfer model, the emission from higher vibration levels, and the correct rotational (microwave) emission model. The effects of these new features on our early results (mostly for the Pele type plumes) will be discussed at each point where they arise (mostly in Chapter 4). The results from the earlier model are still used in Chapter 4 for the introduction of basic features associated with the simulated volcanic plumes. Conclusions based on the more approximate early model remain at least qualitatively true for Pele type plumes and in most cases quantitative discrepancies of only $\sim 10 - 20\%$ arise when compared with the

improved model. We have also verified that the new model has no significant impact on the early results for small Prometheus type plumes. Therefore, many early Prometheus plume results are still used throughout the present work. Fortuitously, the effects of the variable gravity field and the emission from higher vibration levels tend to cancel which results in similar nominal vent conditions for Pele type plumes to those from the early results. Finally, a list of assumptions used in each result is provided in Appendix G in Table G.1.

3.3 Multi-domain Sequential Calculation

As pointed out above, numerical challenges arise when trying to include various mechanisms such as non-LTE thermal radiation into the DSMC calculations. For instance, the lifetime of the excited ν_3 vibrational state of SO_2 molecules is about 23 ms, so the time step in the calculation of the radiation from this band should be smaller than 23 ms. This time step, however, is too small for efficient calculation of ν_2 radiation, which has a lifetime of about 1 s. On the other hand, as pointed out earlier, the plume flow experiences a wide range of flow regimes from near-continuum to free molecular. In the near-continuum regime, we need very fine spatial and temporal resolution, while in the transitional and free molecular regime we do not.

These challenges are common in DSMC and various solutions have been proposed to overcome them (Roveda *et al.* 1997, Gimelshein *et al.* 2001). A multi-domain sequential calculation is used in our simulation. This approach is applicable because the flow is usually supersonic near the vent so it is not
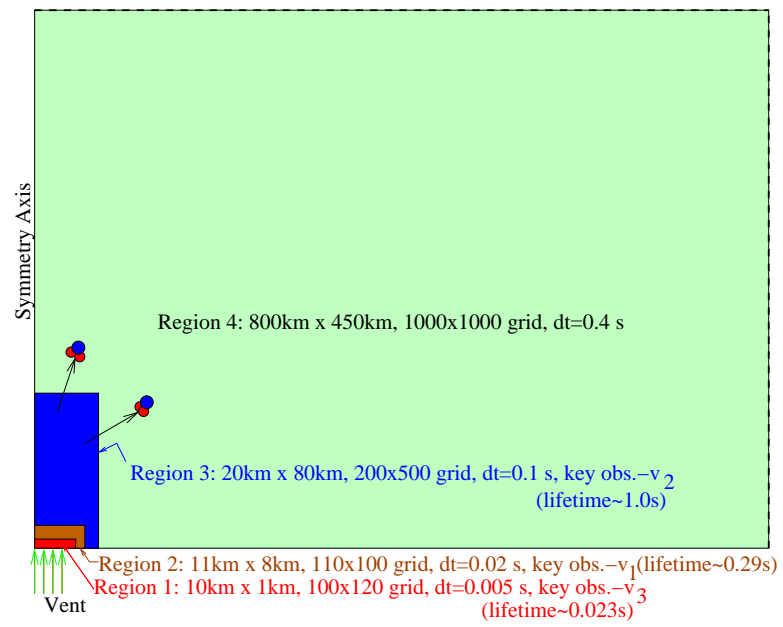
Figure 3.6: Schematic diagram of multi-domain sequential calculation.

affected by downstream conditions. The whole domain is split into multiple subdomains and sequential calculations are performed from the inner to outer domains. The majority of radiation events in the ν_1 and ν_3 bands are therefore captured with both very fine spatial and temporal resolution, and those in the ν_2 band with relatively coarser resolution. After most of the radiation features are captured at the core of the plume, an even coarser resolution is sufficient to calculate the downstream flow field. Figure 3.6 shows a schematic diagram of this flowfield decomposition. Example calculation parameters (domain size, grids, and timestep dt) and the key observables that drive their choice in each region are also shown in Fig. 3.6. The flow field is first obtained for tiny innermost region 1 with very fine spatial and temporal resolution to capture the signature of ν_3 band radiation. Molecules that cross the upper and right boundaries after steady state has been reached are stored as a source of input molecules for the calculation of region 2. During the calculation of region 2, molecules are read in to give the correct number flux. The process of storing and re-reading molecules between concentric regions is carried on until the whole flow field has been obtained. In our case, four steps are necessary. The sizes and grid structures of each domain shown in Fig. 3.6 are for the simulation of a nightside Pele type plume discussed in the following section. These parameters vary and are chosen appropriately for different plumes, but the storing and re-reading procedures for molecules are the same for all simulations.

The radial weighting factors may vary from one subdomain to another

One cell in coarser outer domain

weighting factor = (a+b+c+d)/4

weighting factor = a | weighting factor = b | weighting factor = c | weighting factor = d

Cells in finer inner domain
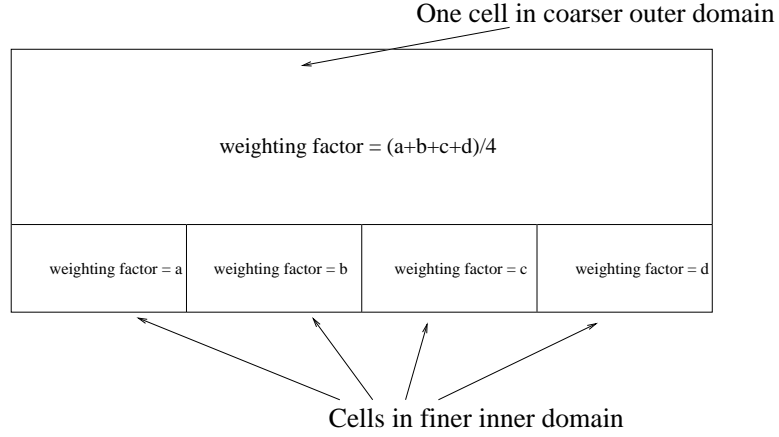
Figure 3.7: Schematic diagram of the dependence of the radial cell-based weighting factors of coarser outer domain on those of finer inner domain at the interface of the two domains.

because we need to maintain a correct number flux crossing the interfaces between subdomains having various time steps, and keep a reasonable number of simulated molecules in each subdomain at the same time. In general, the weighting factor is set to keep the number of simulated molecules in each cell around 50. This can be maintained by adapting the radial weighting factors of each subdomain. One should be careful, however, when dealing with the these weighting factors as the grid structures in the radial direction change from one domain to another. The radial weighting factors of each cell in the coarser outer domain depend on those in the finer inner domain because the molecules passed from the inner domain carry with them weights that must be represented correctly in the outer domain calculation. Each cell of the coarse outer domain at the interface of the outer and inner domains contains molecules from different adjacent inner cells usually with different weighting

43

factors. Therefore, a new weight for these molecules must be assigned. In our calculations, the width of the cell in the outer domain is set to n times that of the inner domain, where n is an integer, and an average of the radial weighting factors of those cells in the inner domain is used for the one cell in the coarser outer domain. This is illustrated by an example in Fig. 3.7 where n is 4.

A particular advantage of this sequential calculation is the good quality of the solution obtained near the vent where the Knudsen numbers are very low, while obviating the expense of carrying the very fine resolution through the whole domain. Also, in some cases, the sequential calculation is even faster than a single domain calculation. The most time consuming calculation in DSMC is the calculation of inter-molecular collisions. The collision rate is highest in the vent vicinity. However, the flow there reaches steady state much more rapidly than the whole plume does. Thus, it is inefficient to carry on the calculation of the flow in the vent vicinity after it reaches steady state. Since a multi-domain sequential calculation stops the computation of the flow in the vent vicinity after it reaches steady state, there is a dramatic saving in computational time - by a factor of $\sim 2 - 3$. This is especially significant for simulation of large Pele-type plumes with a small vent and high number density at the vent.

It should be pointed out that the multi-domain sequential calculation is only necessary for accurate plume spectra calculations in which high spatial resolution distribution of the population of internal energy modes is important. The gas dynamics in the plume is, however, represented accurate enough with
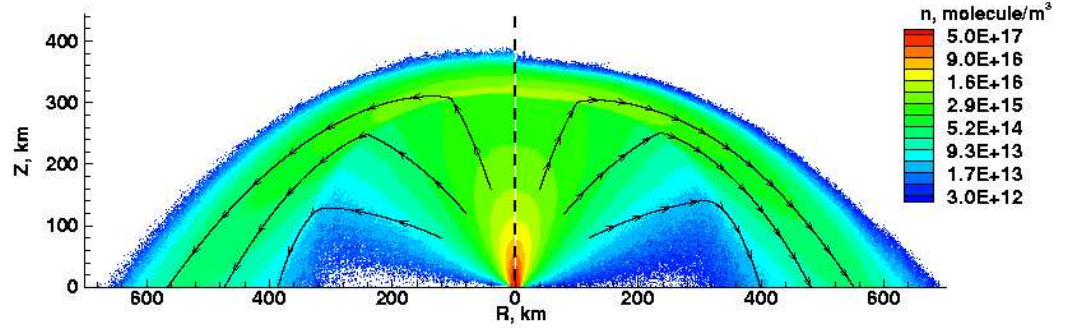
Figure 3.8: Number density contours of simulated Pele-type plume with single domain calculation (left) and multi-domain calculation (right).

an ordinary single domain single time step calculation. Fig. 3.8 shows that although the number densities at each location are not the same, they are qualitatively similar, and the differences in the canopy shock and plume heights and the plume width are negligible. Therefore, except in Chapter 4 or unless otherwise specified, the results presented are simulated with a single domain calculation.

3.4 Convergence Study

The calculations were checked for convergence with respect to grid, time step and number of simulated molecules. Figure 3.9 shows the results of number of simulated molecules convergence study, Fig. 3.10 shows grid convergence, and Fig. 3.11 shows time step convergence for a nominal Prometheus type plume. The results converge reasonably well (generally with less than

1% deviation of number density) except maybe for slight differences in the most coarse grid computation (Fig. 3.10a) from the rest. The criterion for the choice of spatial and temporal resolution is usually based on the mean free path λ and collision time τ_{col}, respectively. This criterion is quite stringent for a non-adaptive single domain calculation and can only be achieved by a multi-domain calculation. For example, in the nominal Prometheus type plume discussed above, the mean free path is $\sim$1 m and the collision time is $\sim$4 ms at the vent. These resolutions cannot be achieved by a single domain calculation. However, it may not be necessary to use such high resolutions since the length (vent radius, r) and time scale (the time it takes for gas to rise a distance of r above the vent) in the nominal Prometheus or Pele type plume is much larger, e.g. $\sim$10 km and $\sim$10 s, respectively. Therefore, less stringent but reasonable spatial and temporal resolutions are used in the single domain runs and have been shown to converge in the above discussions. The instantaneous number of particles per cell in the vent vicinity is usually maintained at $\sim$50 to get a reasonable statistical smoothness.

3.5 Parametric Study of Vent Conditions

A parametric study is performed for plumes assuming a surface temperature of 90 K. At such a low surface temperature, the sublimation atmosphere is negligible. Calculations showed that a canopy shaped shock is generated in a volcanic gas plume as a result of the gas flow falling back on itself due to gravity, and a ring shaped deposition pattern is formed around the vent
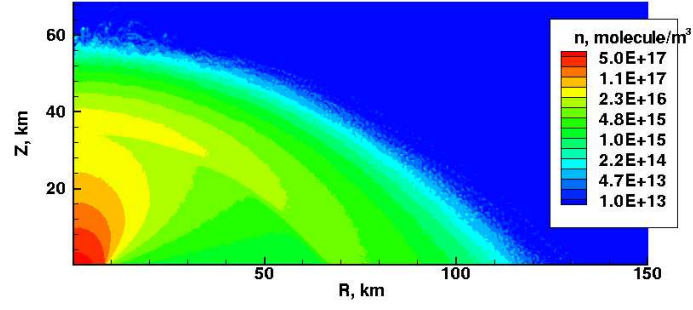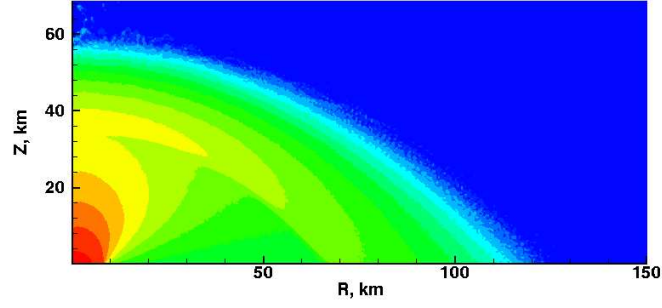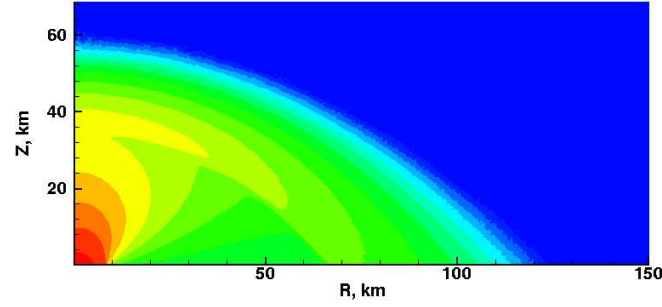
Figure 3.9: Number density contours of simulated Prometheus-type plume with total instantaneous number of simulated molecules of approximately a) 300,000, b) 600,000, and c) 3,500,000. For all the three cases, the time step and grid size are 0.5 s and 600×300, respectively. Differences are negligible.
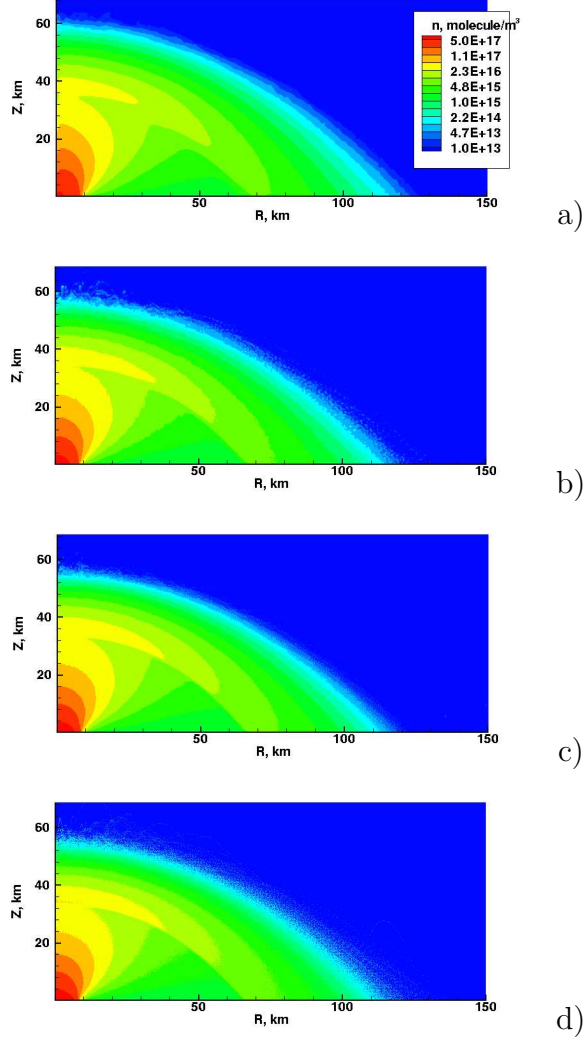
Figure 3.10: Number density contours of simulated Prometheus-type plume with grids of a) 300 × 150, b) 600 × 300, c) 1200 × 600, and d) 2400 × 1200. For all the three cases, the time step and number of simulated molecules are 0.5 s and approximately 1,000,000, respectively. Note the slight difference in the shape of contours near the shock between the most coarse grid computation in a) and the other calculations.
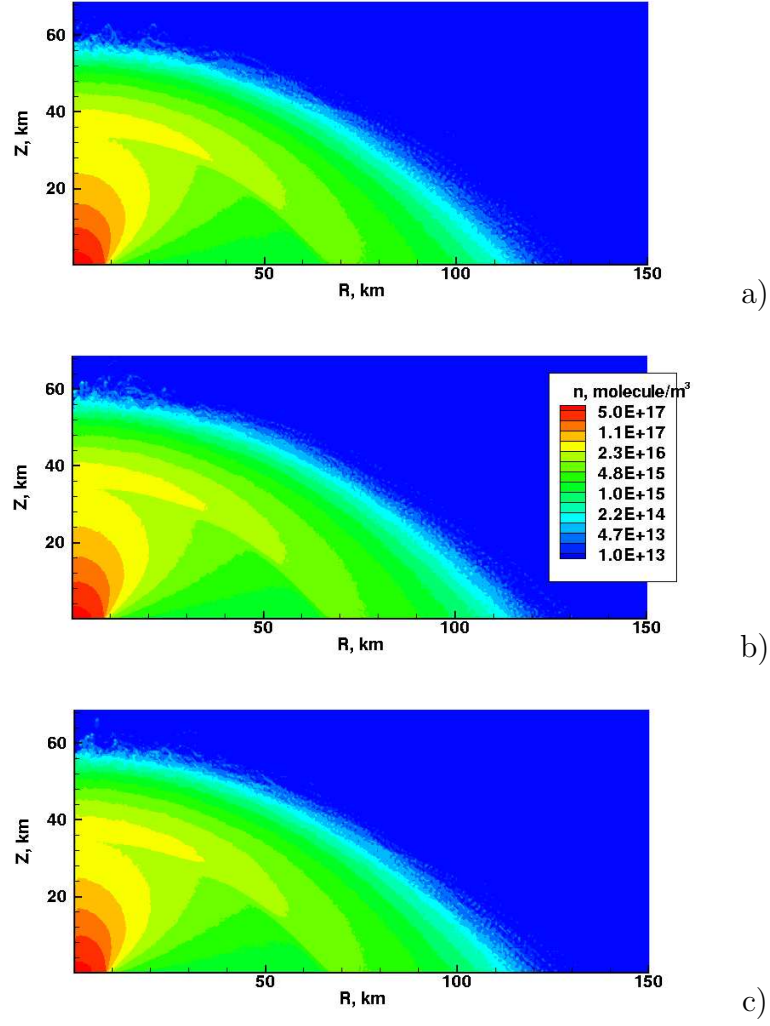
Figure 3.11: Number density contours of simulated Prometheus-type plume with time steps of a) 0.2 s, b) 0.5 s, and c) 1.0 s. For all the three cases, the grid and number of simulated molecules are 600 × 300, and ∼300,000, respectively.

49

as the gas falls on the ground in a night side plume. It is obvious that the plume morphology (shape), the shock height, and the deposition pattern are all functions of the vent and surface conditions. Knowledge of the dependence of plume morphology on "virtual" vent[2] conditions is very helpful in constraining the vent conditions using the observed plume shape. Quite often, the vent velocities are estimated by the ballistic height which is adequate for a first order estimate. However, the ballistic estimate is not accurate when the thermal energy of the gas and intermolecular collisions in the gas contribute to the development of the plume shape (as will be shown by some examples in the Chapter 5). Hence, we carried out a parametric study on V_v and T_v. Two sets of iso-contours in vent velocity-temperature (V-T) space were mapped with one set corresponding to constant canopy shock heights (H_{shock}) and the other to constant peak deposition ring radii (R_{ring}). Since relatively simple contour shapes were expected, only sparsely distributed but carefully selected (V_v, T_v) points were examined instead of closely spaced uniform (V_v, T_v) parameter grids. This reduced computational time dramatically. A couple of widely spread (V_v, T_v) combinations were first tried, approximate iso-contours of H_{shock} (or R_{ring}) were obtained by interpolation in Tecplot (an engineering graphic software package), and relatively simple contour shapes were indeed observed. More accurate contours were then obtained by testing more (V_v, T_v) combinations as needed. After these two sets of iso-contours were produced, we aimed to constrain the unique combination of the vent velocity and tem-

---

[2]The concept of "virtual" vent will be explained in Chapter 6.

perature by the observed shock height and peak deposition radius. It should be pointed out that the accuracy of the constraints depends on how good the model is and how well the assumptions at the vent represent reality. The assumptions here include an ∼8 km "virtual" vent radius, a fixed source number density at the vent (5×10^{17} molecules/m^3), and an optically thin gas in the ν_1, ν_2, and ν_3 SO$_2$ vibrational bands. It will be shown in the Chapter 5 that if the source number densities are changed within a certain range, the gas flows would still have approximately the same column density contour shapes except that the contour levels would be scaled by the ratio of the two source number densities. For this reason, the source number density was kept fixed in the study. The assumption of optically thin gas at SO$_2$ vibrational bands is adequate if the "virtual" vent radius is ∼8 km and the source number density is not too high. The opacity of the gas becomes significant and must be considered if the "virtual" vent radius is ∼1 km and the source number density is high. However, as will be shown in Chapter 5, the opacity of the gas generally causes only $\sim 10 - 20\%$ differences in the constrained vent conditions. The accuracy of these assumptions will also be discussed in greater detail in Chapter 6 after the results are presented.

3.6   "Overlay" Gas/particle Flow Model

Special effort has been expended on modeling the gas/particle flow in these volcanic plumes. Spencer *et al.* (1997) showed that the wavelength dependence of the optical depth in 1996 HST observations of Pele can be

matched by either a plume of SO_2 gas with a total mass of 1.1×10^{11} g or a dust plume of very small scattering particles with minimum total mass of 1×10^9 g and maximum particle size of 0.08 μm. They also suggested that either of these two possibilities, or a combination of them, is consistent with Voyager and HST observations. Since there are many positive SO_2 detections and Spencer *et al.* (1997) showed that their inferred SO_2 abundance is comparable to these estimates, it is reasonable to assume that Pele consists mainly of gas rather than dust, and the total mass of the gas is at least two orders of magnitude higher than dust. At such a low particle (dust) mass loading of less than $\sim 1\%$ it may be assumed that the flow of particles entrained in the gas plume does not alter the gas flow. Therefore, "overlay" techniques may be used to model the gas/particle flow. Two "overlay" methods were used. In the first method, referred to as the Collision Model, the particles were treated simply as another molecular species in DSMC and were allowed to collide with gas molecules. These "molecules" are huge in size compared to gas molecules and collide elastically with the gas molecules. Since it is assumed that the particle flow does not alter the gas flow, only the particle velocities are modified by each collision that involves a gas molecule and a particle. Note that, in order to get a sufficiently smooth particle flow field, it is necessary to continue the computation of the steady background gas flow after the background gas flow reaches steady state and the calculation of the particle flow started. The other method, referred to as the Drag Model, is to calculate the drag on the particles in a *pre-calculated* or frozen gas flow field and move the particles accordingly.

Since the particle-size based Knudsen number, Kn, is much greater than one, the drag coefficient, C_d, in the free molecular limit (Eqn. 3.3) can be used (Bird 1994).

$$C_d = \frac{(2s^2 + 1)exp(-s^2)}{\sqrt{\pi}s^3} + \frac{(4s^4 + 4s^2 - 1)}{2s^4}erf(s) + \frac{2(1-\varepsilon)\sqrt{\pi}}{3s}(\frac{T_w}{T_\infty})^{1/2} \quad (3.3)$$

where, $s = U_\infty \beta_\infty = U_\infty / \sqrt{2kT/m}$, ε is the fraction of molecules that are reflected specularly (the remaining fraction 1 - ε is reflected diffusely), T_w is the temperature of of particles, and T_∞ is the temperature of the gas stream. Assuming a cold sphere or a fully specular reflection ($\varepsilon = 1$), the free molecular drag coefficient is then reduced to the following,

$$C_d = \frac{(2s^2 + 1)exp(-s^2)}{\sqrt{\pi}s^3} + \frac{(4s^4 + 4s^2 - 1)}{2s^4}erf(s) \quad (3.4)$$

It is worth pointing out that one must be careful when dealing with small values of s: $C_d \to \frac{16}{3\sqrt{\pi}s}exp(-s^2)$ as $s \to 0$. A very accurate value of π (at least 7-8 digits) should be used in Eqn. 3.4 as $s \to 0$, otherwise the singular behavior of C_d will be incorrect and the finite drag ($\propto C_d s^2$) will become singular as $s \to 0$.

In both methods, it is assumed that the fine particulates are spherical (aimed at modeling crystals or droplets), and that the particle flow is so dilute that the particles do not collide with each other. The particles are released at zero velocity from the vent, although it should be recognized that the particles probably have an initial velocity. However, the effect of the initial velocity is very small due to the close coupling between the motion of the gas and the

particles for nano-size particles that are the focus of the present work. The initial velocity is important if the particles are large and the effect is briefly discussed in Appendix E. In our models, the particles execute Brownian motion, though this cannot be seen in particle trajectories plotted at km resolution. The mean number density of the above mentioned 0.08 μm particles is ~ 8 orders of magnitude lower than the gas number density assuming dust particle mass loading of 1%. Thus, although the cross sectional area of a particle is $\sim 10^4$ times larger than that of a gas molecule, the particle-particle collision frequency is still at least $\sim 10^4$ times lower than that of the gas molecules, and the assumption of no collisions between particles is thus justified. The particles are assumed to be *refractory* so that coagulation and evaporation are neglected in the models. The particles are also assumed to have a density of SO$_2$ liquid, 1.5 g/cm^3.

Each "overlay" method has computational advantages in different limits. The Collision Model is more suitable for nano-sized particles, while the Drag Model is best for relatively large, micron-sized particles. The collision rate of a nano-particle with the background gas molecules is not unreasonably large, thus the Collision Model is computationally affordable. Because of the large accelerations experienced by the nano-particles, the Drag Model requires an unreasonably small time step and thus is not suitable. For micron-particles, the collision rate with the background gas molecules becomes so large that the Collision Model is very expensive, but the particle trajectories can be easily computed by the Drag Model. Therefore, the Drag Model is used when
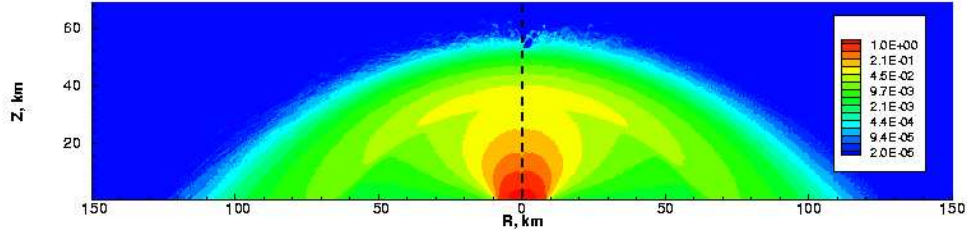
Figure 3.12: The number density contours of gas plume (left) and virtual SO_2 molecules (right).

particles are large, while the Collision Model is used if particles are small.

3.6.1 Validation of the "Overlay" Model

The validation here relies on convergence studies. For the Collision Model, the "overlay" particle flow is expected to asymptotically approach the background gas flow if the particles have SO_2 molecular size and mass (thus virtual molecules). Such convergence has been obtained as shown in Fig. 3.12 which illustrates the number density contours of virtual SO_2 molecules and the background gas. Additionally, the Collision and Drag Models were run with identical particle sizes and the results agreed providing a measure of cross-validation. Figure 3.13 compares particle trajectories calculated with the Collision Model and the Drag Model for a few vent input locations for 10 nm particles.

3.6.2 Collision Weight

As discussed above, the Collision Model is not suitable for the calculation of flows with large particles because the computation of the many collisions between a large particle and the background gas molecules becomes very time consuming. A "collision weight" can be used to extend the ability of the Collision Model to calculate flow of large particles. In such a calculation, the collision between a gas molecule and a particle is assumed to be N times as effective, where N is the collision weight, but N times less frequent. By "N times as effective", it is meant that in each collision the gas molecule is set to be N times more massive. Fig. 3.14 shows the comparison of particle trajectories calculated with and without a collision weighting factor of $N = 5$. The good agreement between the trajectories indicates that the collision weighting method is a reasonable way to reduce computational expense for trajectory calculations of large particles.

3.7 Column Density and Shadow Calculations

The column density along tangential lines of sight (herein referred to as TCD, i.e. tangential column density) can be calculated by ray tracing. Such calculations are necessary for direct comparison with observations of plume brightness. The angel of the center of the vent source with respect to limb (ϕ) is taken into account in the calculation as shown in Fig. 3.15a. The plume axis passing through the origin of Io is in the plane of the paper.

The column density at viewing angles other than tangential can be
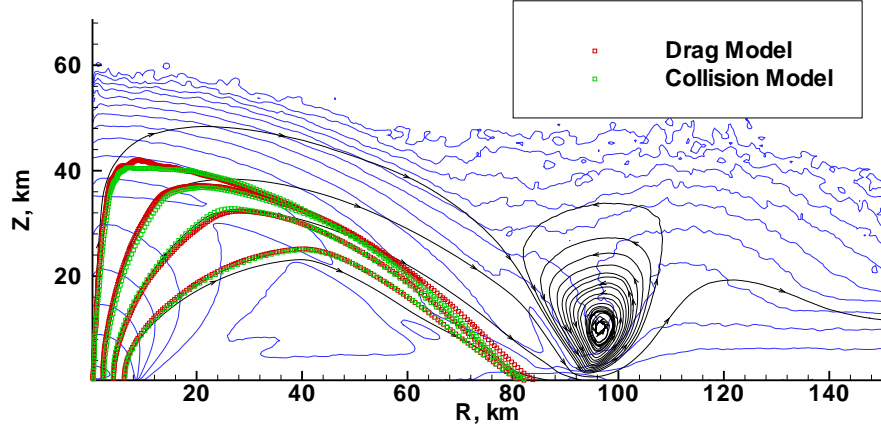
Figure 3.13: Comparison of 10 nm particle trajectories calculated with the Collision Model and the Drag Model. Also plotted are the gas number density contours (blue) and the streamlines (black).
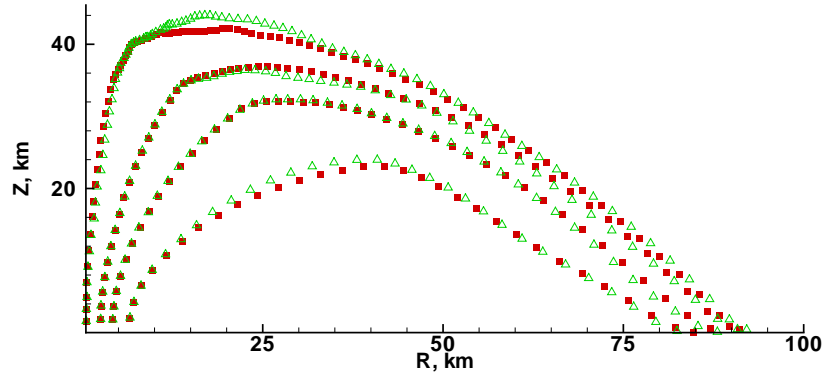
Figure 3.14: Comparison of particle trajectories calculated with collision weighting factor (red close square) and without the weighting factor (green open delta).
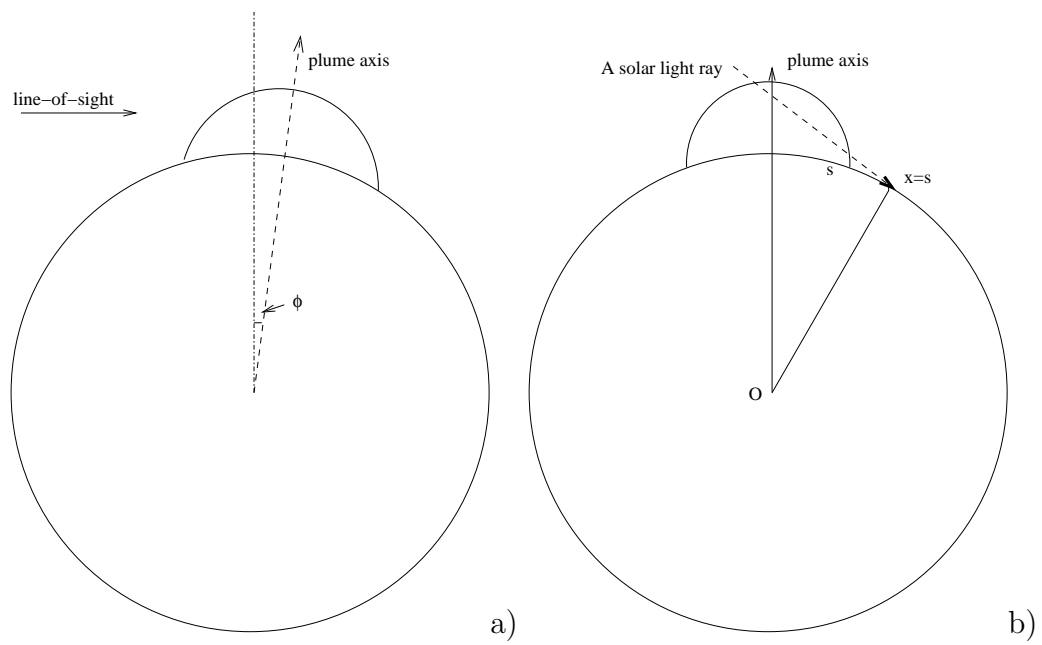
Figure 3.15: Schematic of ray tracing calculation for a) TCD; and b) shadow of plume with the consideration of spherical geometry.

projected onto the surface of Io and interpreted as the shadow cast by the plume if the particle plume that cast the shadow is optically thin. The effects of the plume opacity will be investigated in the future. Figure 3.15b shows the schematic diagram of this situation. The elongation of the shadow because of the spherical geometry of the surface of Io is also taken into account by allowing the solar ray (line of integration) to intersect with the surface of a sphere of radius of Io and calculating the length of the arc s as shown in Fig. 3.15b. Once the line of integration becomes tangential to the surface of Io at the terminator, the plume stops casting a shadow.

Chapter 4

Basic Features associated with Simulated Volcanic Plumes

4.1 Overview

In this chapter, the basic features associated with simulated plumes are discussed. Example results of two types of simulated plumes, Pele- and Prometheus-type, are presented, and plumes on both nightside and dayside are discussed. The relatively simple nightside Pele type plume is discussed first in Section 4.2, and Section 4.3 contains the results for a dayside Pele type plume. Results for a dayside Prometheus type plume are illustrated in Section 4.4. The basic features include the shape (height and diameter) of the simulated plumes, the flow properties such as the local number density, temperature, Mach number, emission rate, in the plume, the shocks appearing in the flow, deposition patterns and so on. Finally in Section 4.5, the simulation results are compared to observations and reasonably good agreement is obtained.

4.2 Nightside Pele type Plume

A simulation of a night-side Pele type volcanic plume on Io is discussed first because the resulting gas dynamics is relatively simple. We have chosen

a uniform vent mean velocity of 1000 m/s for Pele estimated by Strom and Schneider (1982). Several vent temperatures were tried and 650 K was chosen since it gives results that are a good fit to the general shape and deposition pattern of the plume observed by Voyager 1. Even though recent measurements suggest that the rock temperature near a vent could be higher than 650 K, the vent temperature used in the simulations represents the temperature at the "virtual" vent where the gas has expanded to reach the velocity of 1000 m/s. The heating of the gas by possible nearby hot lava is ignored. The source number density of 5.0×10^{17} m^{-3} (equivalent to a pressure of 45 nanobar at T_v of 650 K) was the lower limit of the gas source rate ($\sim 10^{29}$ SO$_2$ s^{-1}) estimated by Moreno *et al.* (1991). The nightside surface temperature was selected to be 90 K in agreement with observation (Johnson and Matson 1989). This value is also in the range of observed nightside surface temperature recently reported by Rathbun *et al.* (2002), who suggested a maximum nightside surface temperature of 95 K at the equator. Also, following Moreno *et al.* (1991), the vent has been assumed to be round, with radius of $\sim$8 km. This radius seems to be too large for a vent since the vent size is usually less than a couple of kilometers on Earth. However, the Earth analogy may be misleading in the sense that volcanism on Io may be quite different from that on Earth. In addition, as will be discussed in Chapter 6, the concept of a "virtual" vent makes the vent diameter of $\sim$10 km reasonable.

Io's nightside surface temperature of 90 K is very low, and nearly all the gas that falls to the surface will condense; the sublimation atmosphere under
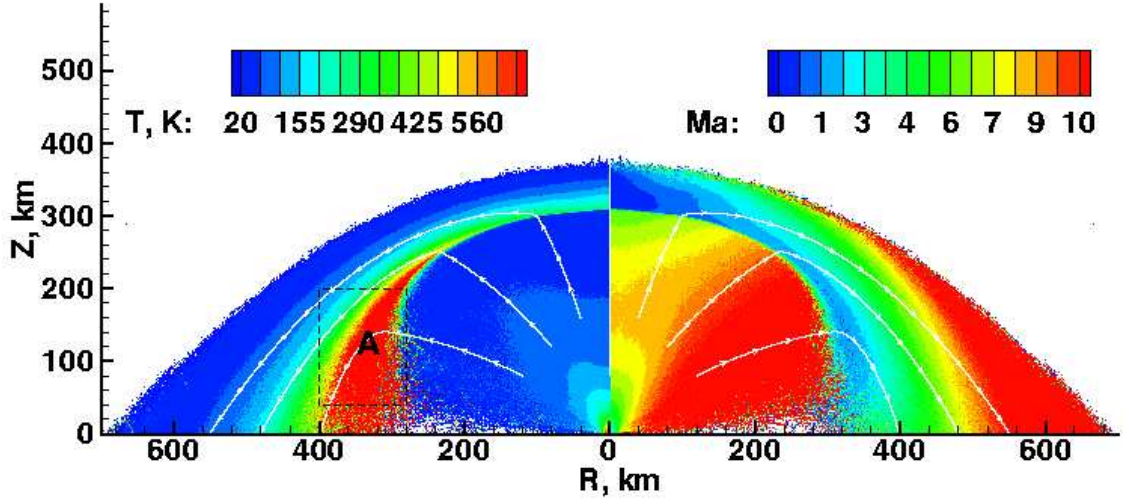
Figure 4.1: Temperature (left) and Mach number (right) contours with stream-lines overlapped for nightside Pele type plume. The black dashed box indicates the non-equilibrium low density region A.

such conditions is negligible. Figure 4.1 shows the calculated Mach number and temperature contours with streamlines overlayed. It can be seen that as the gas erupts from the vent at around Mach 3, it expands, accelerates and cools. A canopy-shaped shock is formed at a height of about 300 km. An interesting aspect of this canopy shock is that it is formed as a result of the presence of the gravity field rather than an atmosphere back-pressure or a deflection introduced by a solid surface as in most engineering applications. It is also seen that once the gas is high above or far away from the vent (roughly at $Z > 100$ km or $R > 60$ km), it becomes almost collisionless and freezes at $\sim$50 K until it reaches the shock. This frozen temperature region is where one could use a simple ballistic model to represent the flow. After being

62
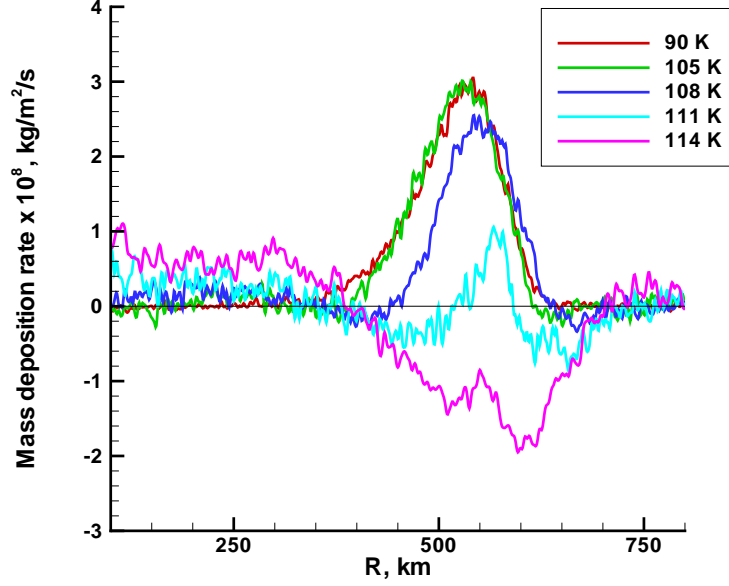
Figure 4.2: Mass deposition rate profiles at several different surface temperatures for a Pele type plume.

compressed and heated while crossing the shock, the flow turns outward and expands and cools again as it accelerates downward. The gas finally falls to the cold ground and condenses to form a ring of frost. The corresponding mass deposition rate profile along the surface is shown in Fig. 4.2. It is seen that most of the frost deposit is concentrated in a range from $R = 400$ to 600 km. The resurfacing rate is found to be 0.06 cm/year at the maximum deposition rate assuming a frost density of 1.5 g/cm^3.

Figure 4.3 shows the SO$_2$ number density contours of the flowfield. The vertical column density profile is also plotted in the figure and the average
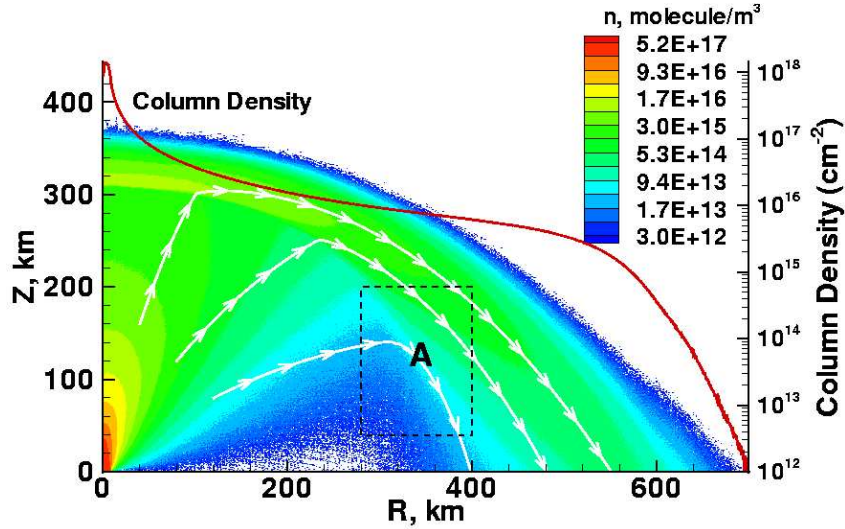
Figure 4.3: SO$_2$ Number density (molecule/m^3) contours with streamlines overlayed for nightside Pele type plume. The black dashed box indicates the non-equilibrium low density region A. Also plotted is the column density profile (red curve).

column density over the plume out to $R = 700$ km is calculated to be $\sim 1.1 \times 10^{16}$ cm^{-2}. The total mass of the gas in the plume is calculated to be 1.37 $\times 10^{10}$ g and about one tenth of the mass (6.5 $\times 10^8$ g) is in the plume core. Both the column density near the plume center ($\sim 10^{18}$ cm^{-2}) and the average column density over the plume are of the same order of magnitude as those obtained by Lellouch (1996). The average column density is about three times lower than that for Pele obtained by McGrath et $al.$ (2000), but close to that obtained by Strobel and Wolven (2001) for the entire surface of Io, based on the analysis of Feldman et $al.$ (2000).

64

Falling cold molecules

A

Nearly collisionless
mixture of two sets of
cold molecules produces
bimodal "hot" region A.

Radially expanding
cold molecules

Resulting mean flow
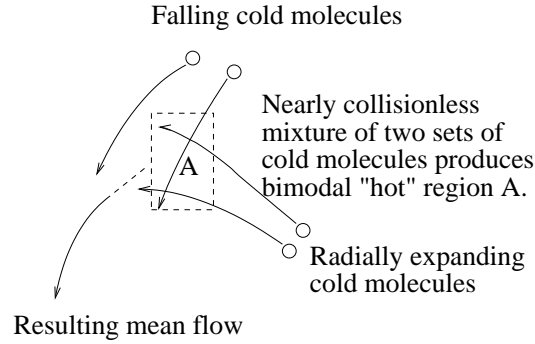
Figure 4.4: Schematic diagram of flows in the boxed non-equilibrium region
A.

There is a region indicated by a dashed rectangle (called region A) in
Fig. 4.1 around $(R, Z){=}(350$ km, 100 km) where the temperature seems to be
unreasonably high ($\sim$1000 K); the temperature at the vent is only 650 K. The
same region is indicated in Fig. 4.3 where is seen that the number density of
the flowfield is very low. Because the number densities in this region are very
low, the gas is a nearly collisionless mixture of molecules that have expanded
radially outwards and those that are falling back to the surface under the influ-
ence of gravity (Fig 4.4). Gravity also turns the radially expanding molecules
towards the surface and the mean flow streamlines turn towards the surface
around $R =$300 km. In boxed area A, the velocity distribution is bimodal
with two "cold" spikes of very different vertical velocity. The two modes in
the velocity distribution of the molecules at a point near $(R, Z){=}(350$ km, 100
km) can be clearly seen in Fig. 4.5. One set of the molecules have veloci-
ties concentrated around $(V_r, V_z){=}(280$ m/s, -700 m/s) and the other set are

65
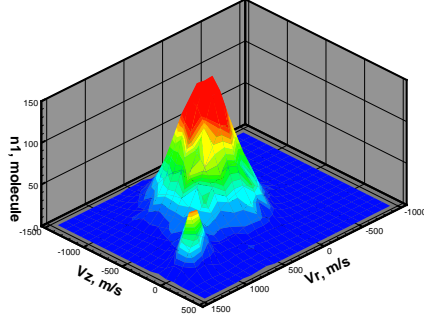
Figure 4.5: Velocity distribution profile in a 10 km × 10 km region centered at $(R, Z){=}(350$ km, 100 km).

around $(V_r, V_z){=}(1100$ m/s, -50 m/s). Representing this bimodal distribution by a single kinetic temperature based on the mean velocity results in the high computed temperature.

The contours of photon emission rate are shown in Figs. 4.6 and 4.7. Figure 4.6 shows rate contours in the ν_1 (1151 cm^{-1}), ν_2 (518 cm^{-1}) and ν_3 (1362 cm^{-1}) bands of SO_2 near the plume core. Figure 4.7 shows the contours of photon emission rate for the ν_2 (518 cm^{-1}) band for the whole flow field. It is seen that most of ν_1 and ν_3 band emissions come from a tiny region around the core of the plume and the gas rapidly loses its vibrational energy by emission in the ν_1 and ν_3 bands but relatively more slowly in the ν_2 band. The vibrational energy of the gas is not strongly replenished from translational energy through inter-molecular collisions, since the collision excitation rate is low. Taking the
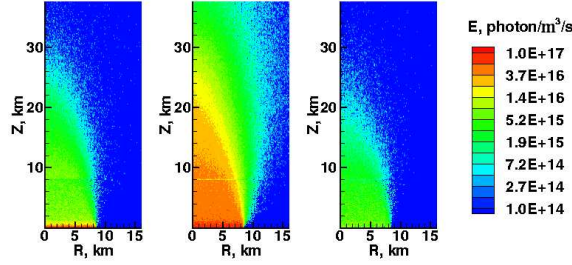
Figure 4.6: Contours of photon emission rate (photons/m^3/s) of ν_1 (1151 cm^{-1}), ν_2 (518 cm^{-1}) and ν_3 (1362 cm^{-1}) (from left to right) vibrational state of SO$_2$ near the plume core for nightside Pele type plume. Note the emission power can be obtained by multiplying the emission rate by the photon energies for the ν_1, ν_2 and ν_3 bands (2.29 $\times 10^{-20}$, 1.03 $\times 10^{-20}$, and 2.70 $\times 10^{-20}$ J/photon, respectively).

ν_3 band for example, the radiative lifetime of the ν_3 vibrational state is $\sim$23 ms but the collision relaxation time at the vent for ν_3 vibrational-translational energy transfer is $\sim$10 s. The gas is thus in a highly non-equilibrium state and the vibrational temperatures for the three vibrational modes become very low by an altitude of $\sim$50 km, $\sim$35 km, and $\sim$30 km, for ν_2, ν_1 and ν_3 bands, respectively.

When the flow reaches the canopy shock, it is again compressed and heated. The inter-molecular collisions become sufficiently frequent and with sufficiently high relative velocity that the ν_2 mode is re-excited and emission from the ν_2 band re-appears at the shock. However, emission in the other two bands does not reappear, principally because of the lower vibrational excitation rates (larger collision numbers Z_v) for the ν_1 and ν_3 vibration (see Section 3.2). No emission appears in the non-equilibrium region A discussed above, because
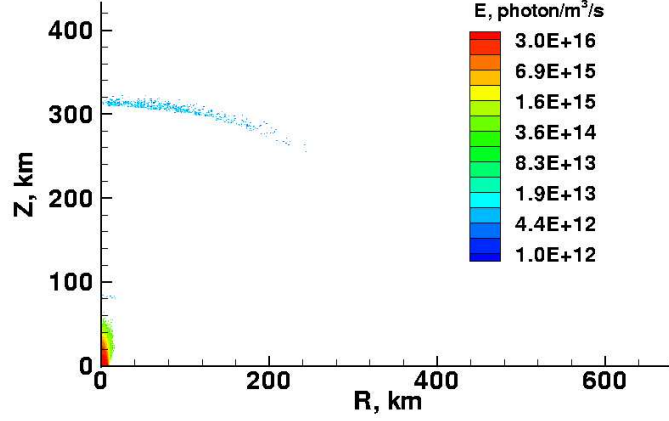
Figure 4.7: Contours of photon emission rate (photons/m^3/s) for ν_2 (518 cm^{-1}) vibrational state of SO$_2$ for nightside Pele type plume

the two components of the flow have a low level of internal excitation and there are not enough intermolecular collisions to cause vibrational excitation.

Figure 4.8 shows that the pattern of rotational (microwave) emission is different from the infrared emission from vibrational bands: the gas does not lose its rotational energy as quickly as it does its vibrational energy. Rotational energy is replenished relatively rapidly by collisions since the rotational collision number (Z_r=5) is much smaller than the vibrational collision number. The overall emission from rotational lines increases at the canopy shock for the same reasons as discussed above for vibrational bands.

An expanded view of temperature and number density contours in
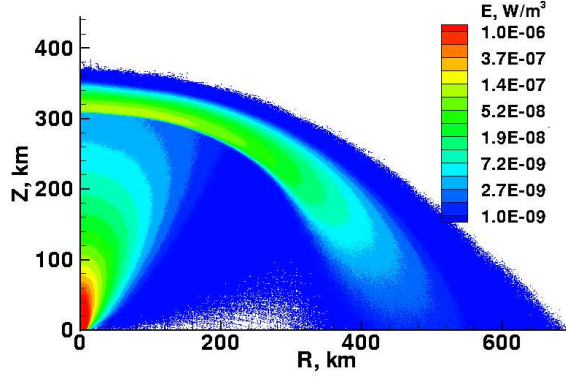
Figure 4.8: Contours of emission (W/m^3) from overall rotational bands of SO$_2$ for nightside Pele type plume.

Fig. 4.9 shows that the decrease of temperature immediately above the vent is caused to a large extent by vibrational band emission rather than by gas expansion. It is seen that, at the core of the plume, the number density does not change much to an altitude of about 20 km, where the expansion wave from the edge of the vent reaches the axis, but the translational temperature drops appreciably. The streamlines and the interfaces between subdomains are also plotted in the figure. The properties are satisfactorily smooth across the computational interfaces.

The total radiation power emitted from the plume is integrated to be 1.7×10^9 W for the ν_2 band, 2.3×10^8 W for the ν_1 band, 1.34×10^8 W for the ν_3 band, and 1.6×10^9 W for the overall rotational lines. For the three vibrational bands, virtually all the emission power comes from the plume core as already discussed above. The radiation powers emitted from the plume core are 1.58×10^9 W, 2.28×10^8 W and 1.33×10^8 W for the ν_2, ν_1 and ν_3

69
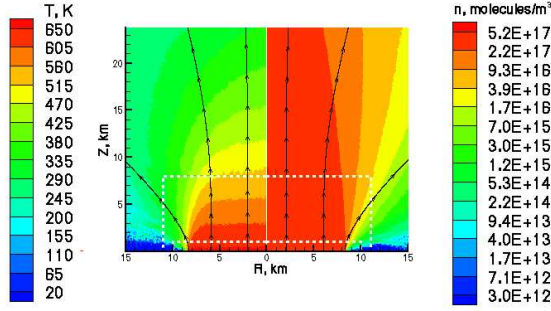
Figure 4.9: Close in look at the temperature contours (left) and number density (molecule/m^3) contours (right). The white dashed lines show the interfaces between regions of different resolutions.

band respectively. For the overall rotational lines, the power emitted from the plume core is only about one tenth (1.1 $\times 10^8$ W) the total power from the whole plume.

We can now examine the effect of plume core and canopy radiation on the ground surrounding the vent. That is, we can ask: is the plume radiation from vibration and rotation bands sufficient to appreciably heat the underlying surface? The schematic of the ray-tracing integration from each pixel in the plume to the surface is illustrated in Fig. 4.10. The total energy flux to a point on the surface (at $X = R$) from the entire plume is then,

$$\int_0^{R_0} \int_0^{Z_0} \frac{P(R', Z')cos\phi R'dR'dZ'}{4\pi} \int_0^{2\pi} \frac{d\theta}{D^2} \tag{4.1}$$

where $P(R', Z')$ is the emission power per unit volume at (R', Z'), D is the distance from the pixel to the surface point $X = R$, and ϕ is the angle between infinitesimal surface element normal to the ray and the surface of Io. Note that to avoid the singularity when the pixel and the surface point overlap, a virtual

70
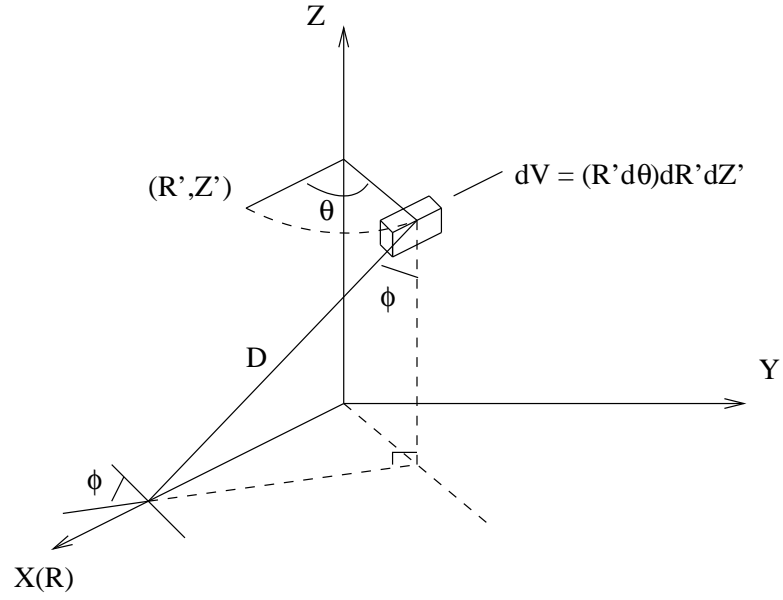
Figure 4.10: Heat flux to the surface due to emission from the simulated Pele plume.

surface at Z of a little smaller than zero is used without losing much accuracy. Figure 4.11 shows that the heat flux to the surface of Io is $\sim$0.01 W/m^2 at a distance of a few tens of kilometers from the edge of the vent. The rate is higher ($\sim$1 W/m^2) closer to the hot column of gas directly over the vent. The results suggest that the additional heating of the surface by plume emission is not important at tens of kilometers away from the edge of the vent compared to the solar flux of $\sim$40 W/m^2.
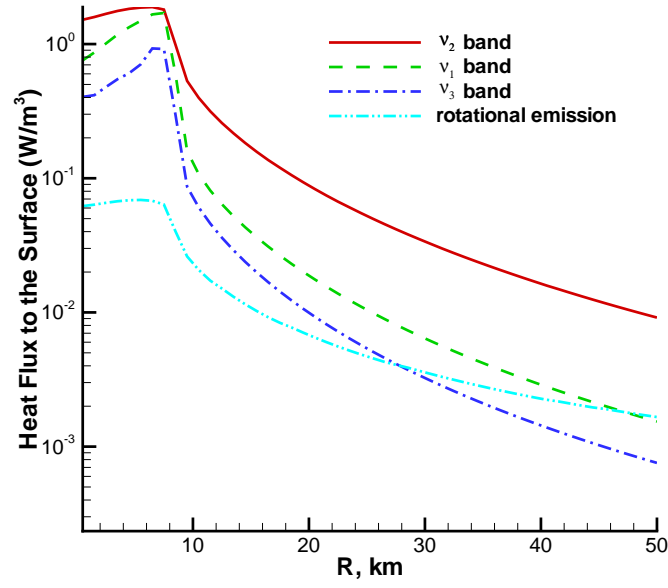
Figure 4.11: Heat flux to the surface due to emission from the simulated Pele plume.
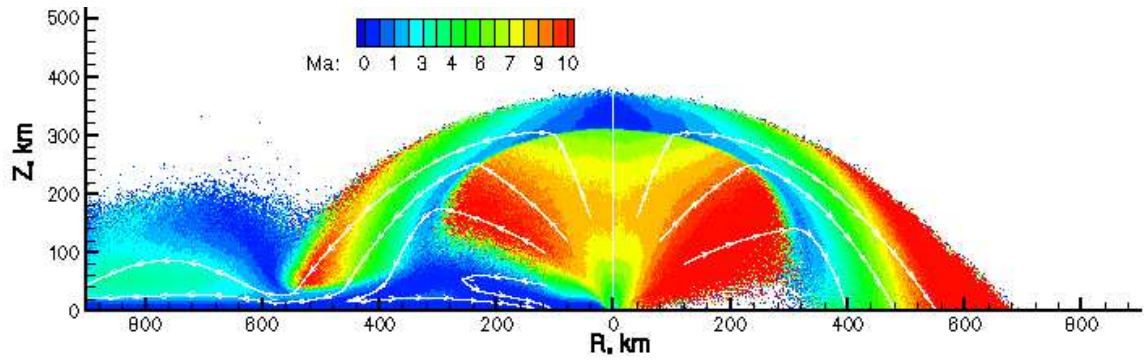
Figure 4.12: Comparison of Mach number contours between dayside (left) and nightside (right) Pele type plume.

4.3 Dayside Pele type Plume: the Impact of a Sublimation Atmosphere on the Plume

A day-side Pele type plume is considered next. The vent conditions are the same as those for the night-side plume. The surrounding surface temperature was set to 115 K which is in the range of the dayside Io surface temperature ($\sim$110-130 K). There will be appreciable sublimation from the surface of Io at this temperature and the atmosphere[1] formed by sublimation will change the volcanic plume flow field dramatically as the plume falls and interacts with it. Figure 4.12 shows a comparison of Mach number contours between day-side and night-side Pele type plumes. It is seen that the flow fields look similar below and at the canopy shock but quite different as the gas that crosses the canopy shock falls to the ground. A re-entry shock is formed in the day-side plume as the result of the interaction between the falling gas and the sublimation atmosphere. Such a shock is not seen in the night-side plume. The plotted streamlines show that for the day-side Pele type plume the sublimation atmosphere is dense enough to split the falling gas into two parts: the outer part is reflected up and turned further outward while the inner part is turned inward toward the symmetry axis. The Galileo image of the Pillan plume (*cf* Fig. 1.1) at almost zero solar zenith angle (SZA) actually shows such outward turning flows of the plume on both sides.

A parametric study was carried out to examine the nature of the impingement of the falling hypersonic gas onto a sublimating surface in greater

---

[1]Scale height H = RT/g $\simeq$ 8.3 km

detail. Several different surface temperatures around 108 K were examined and three such flowfields are compared in Fig. 4.13. It is found that the interaction between the impinging hypersonic gas and the atmosphere is quite sensitive to the surface temperature and the flow structure around the interacting region changes dramatically even for a small change in the surface temperature (105 to 111 K). At a surface temperature of 105 K, the sublimation atmosphere is not dense enough to decelerate and turn the falling gas so that most of the falling molecules strike the ground and condense unimpeded. A small part of the falling gas from the very top of the canopy does, however, get turned by the atmosphere as indicated by the outermost streamline. Here the gas density and thus the dynamic pressure are low.

The amount of the falling gas that is decelerated and turned becomes larger as the surface temperature rises and the sublimation atmosphere becomes more dense. This trend is clearly shown in the figure. Most of the gas is either turned inwards or outwards and the re-entry shock begins to form at a surface temperature of 111 K. This surface temperature of 111 K is interpreted as the critical temperature, at which the sublimation atmosphere vapor pressure is just high enough to balance the stagnation pressure behind a nearly horizontal re-entry shock. This interpretation was confirmed by a similar parametric study performed for a plume with a vent number density that is ten times lower. In this case the critical surface temperature defined above is estimated to be 104 K, in good agreement with the simulations. It is also found that the plume with ten times lower vent number density retains
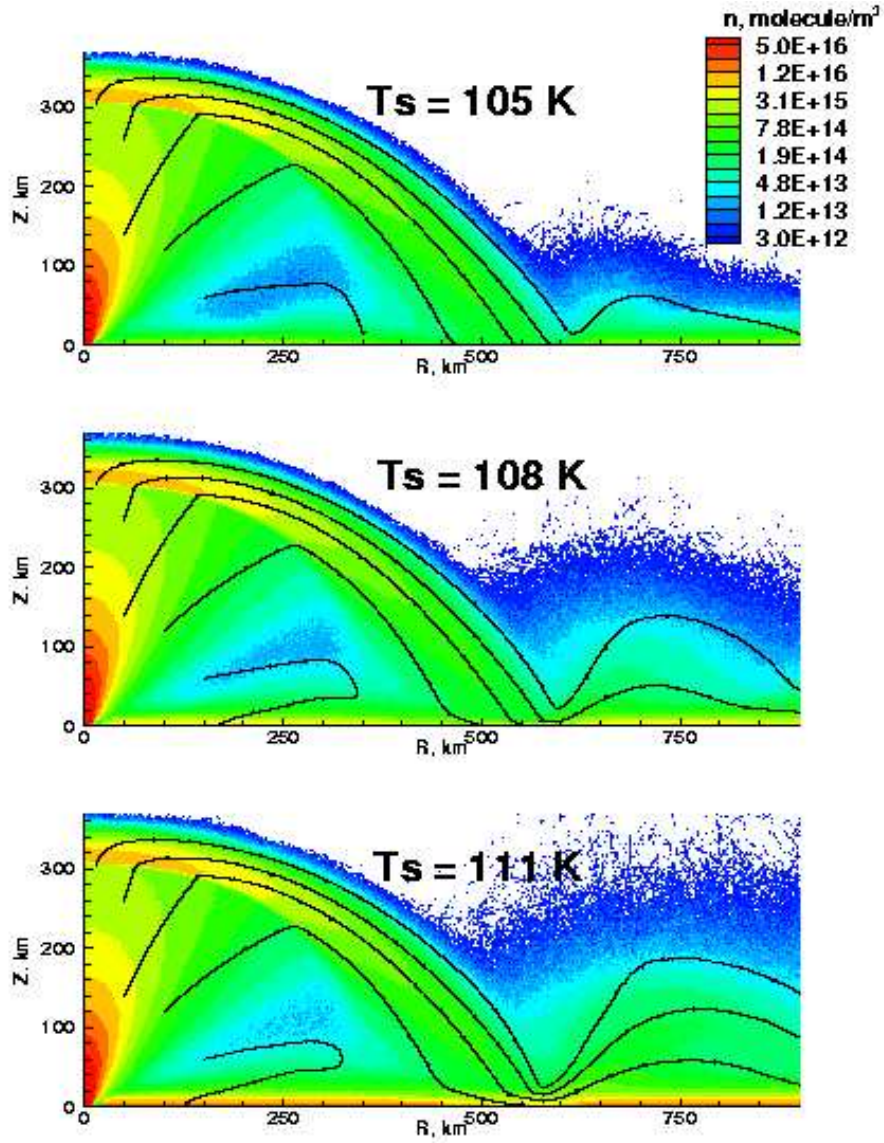
Figure 4.13: Number density contours of the flowfields with different surface temperatures. Notice the formation of a well defined bounce region at higher temperature.

75
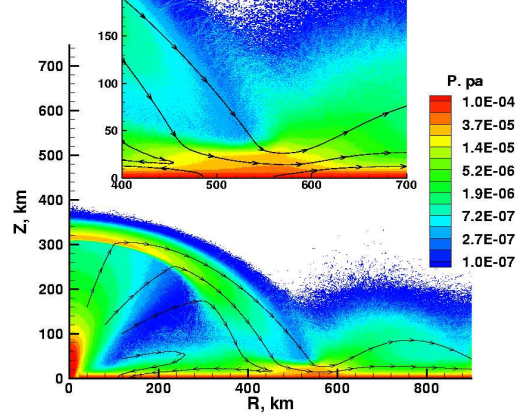
Figure 4.14: Pressure contours of dayside Pele: whole flow field (below) and turning region (inset).

more translational energy and rises higher and expands wider due to the reduced rate of inter-molecular collisions and the reduced internal energy losses through radiation.

The resulting surface deposition patterns, corresponding to the flowfields shown in Fig. 4.13, are plotted in Fig 4.2. At low surface temperatures, the falling gas simply pours onto the surface and condensation dominates resulting in a deposition peak centered at $R = \sim 500$ km. As the surface temperature increases, the SO_2 frost begins to be eroded below the turning point of the impinging flow. We believe that both the outward and inward turning flows entrain the upper part of the sublimation atmosphere which results in a (surprisingly) slightly lower surface pressure than the equilibrium vapor pressure; this causes the depletion of SO_2 frost from the surface by sub-
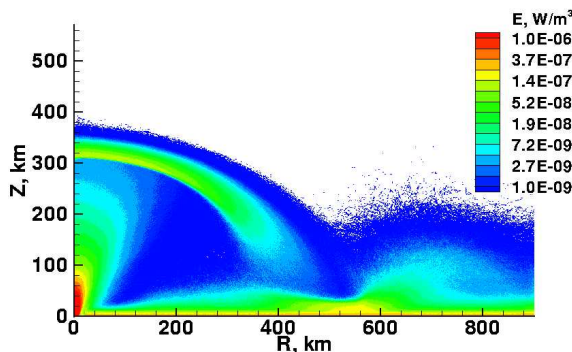
Figure 4.15: Contours of microwave emission (W/m^3) from rotational bands of SO$_2$ for a dayside Pele type plume.

limation. A close-up view of the turning region is also plotted in the inset in Fig. 4.14. The streamlines originating from the surface indicate the depletion effect. At an even higher surface temperature, the depletion becomes dominant and the deposition rate becomes negative from $R = \sim 400$ to 640 km. This is the same vent-centered ring where the peak deposition rate is located at low surface temperatures. These results suggest a possible change of the surface deposition pattern over the span of a day.

The results may also shed some light on the mechanism of the temporary (10-20 min) post-eclipse brightening on Io (Binder and Cruikshank 1964). It has been suggested (Nelson *et al.* 1993) that the brightening is caused by the condensation of atmospheric gases during the eclipse and their evaporation following emergence from shadow causes Io to assume its nominal brightness. However, it was found (Nelson *et al.* 1993) that removal of the SO$_2$ frost by solar heating alone is a very marginal explanation of even a 5%

posteclipse brightening event, and an additional source of energy is required in order to remove the SO_2 frost in the requisite amount of time. Our results above indicate that a volcanic plume does indeed have the ability to remove local regions of the SO_2 frost. As discussed above, the falling gas works as a "pump" and keeps blowing away the sublimation atmosphere established by solar heating. This pump maintains a locally lower surface pressure than the equilibrium vapor pressure. One could also see that the rate of frost removal for our simulated Pele type volcanic plume is, in fact, much larger than that for solar heating under certain conditions. For example, the rate of frost removal in the ring about our plume with surface temperature ~110 K, is about an order of magnitude larger than that near the subsolar region over a sheet of frost at a subsolar temperature of ~110 K (Austin and Goldstein 2000). It has been suggested (Nash *et al.* 1980, Fanale *et al.* 1981) that the posteclipse brightening effect occurs only during periods of intense volcanic activity. So we suggest that, instead of being an additional source of energy only, local erosion by volcanic plumes may be a significant cause of the frost removal during the post-eclipse period.

The contours of photon emission rate for a day-side Pele type plume are very similar to those of a night-side plume especially around the plume core and the canopy shock and thus are not presented in detail. However, another relatively bright spot is seen below the re-entry shock in emission rate contours. This feature is illustrated in Fig. 4.15, which shows the total rotational (microwave) emission contours. As at the canopy shock, the temperature and
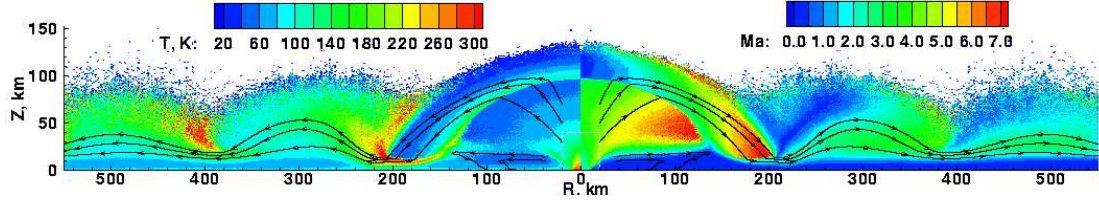
Figure 4.16: Temperature (left) and Mach number (right) contours of dayside Prometheus type plume. The white dashed lines show the interfaces between regions of different resolutions.

number density are both high at the re-entry shock and inter-molecular collisions become so frequent that rotational and vibrational temperatures of the gas increase again so the gas re-emits.

4.4 Dayside Prometheus type Plume

Another type of plume on Io is a Prometheus type which is much smaller than the Pele type, but more common. Six out of nine plumes detected by Voyager 1 were of the Prometheus type (McEwen and Soderblom 1983). As suggested by Kieffer *et al.* (2000), Prometheus is likely not a geyser like Pele but more likely caused by molten lava impinging on a thick SO_2 frost field. The source region for the Prometheus plume has moved over 60 km between the Voyager and Galileo missions. Even so, the nature of the plume itself remains fairly constant. In our early simulations (Zhang *et al.* 2003a), the vent conditions for Prometheus plume were based on the work of McEwen and Soderblom (1983). They suggested that the vent velocity is likely around 500 m/s and the vent temperature is less than 400 K. We chose 500 m/s and

79
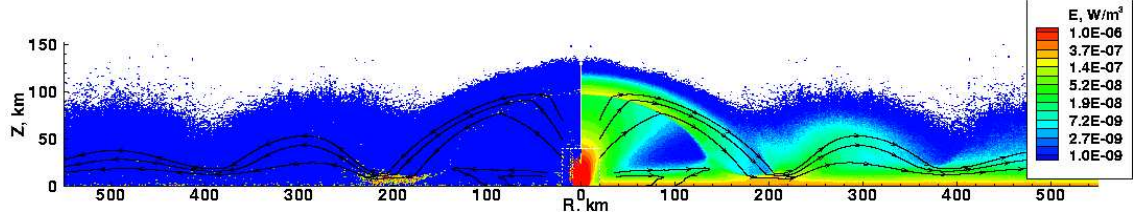
Figure 4.17: Emission (W/m^3) contours from ν_2 vibrational band (left) and overall rotational bands (right) of dayside Prometheus type plume. The white dashed lines show the interfaces between regions of different resolutions.

300 K for the vent velocity and temperature, respectively. Note that these vent conditions are modified in the next Chapter. The surrounding surface temperature was set to a warm day-side value of 115 K.

As expected, in our simulations the plume is much smaller in size than Pele. The Prometheus type plume reaches an altitude of only ∼120 km. However, the flow field features are qualitatively similar to those of Pele. Figure 4.16 shows the temperature and Mach number contours of a dayside Prometheus type plume. One can see that the canopy-shock and the re-entry shock present in the dayside Pele type plume also appear in the dayside Prometheus type plume. A new and interesting feature appears, however, where multiple concentric rises and falls of the flow are seen. As the flow is compressed by the re-entry shock and reflected up, it expands and cools. The upper parts of the flow are pulled down by gravity and the flow is re-compressed to form another re-entry shock further out. This process may be repeated several times. As will be shown shortly, this feature is common to both dayside Prometheus type and Pele type plumes. Figures 4.12 and 4.14 in the previous

80

section show the development of the same features but the multiple shocks are truncated by the limited size of the computational domain.

The emission contours are plotted for the ν_2 vibrational band and overall rotational lines in Fig. 4.17. The features in both contours look quite similar to those of a Pele type plume except for the smaller scale. It is also seen that the multiple rises and falls of the flow discussed above are visible in the overall emission from the rotational lines.

4.5 Comparisons with Observations

Pele is a plume of a very large size that can even be observed from the Earth, so it has been studied extensively. Voyager 1 measured the canopy height of Pele at $\sim$300 km, with a deposition ring diameter of about 1200 km. With the vent parameters chosen, we obtain reasonably good agreement with the Voyager observations of Pele both in the height and the diameter of the plume.

Both the column density near the plume center and the average column density over a nightside Pele type plume are of the same order of magnitude ($\sim 10^{18}$ cm^{-2} and $\sim 10^{16}$ cm^{-2}, respectively) as those obtained by Lellouch (1996) from SO_2 microwave observations. The column density drops from its peak value at the plume center to one order of magnitude lower within $\sim$30 km, so observation resolution has to be smaller than 30 km to measure the large spatial SO_2 variation around plume center. The agreement in column density also justifies our chosen influx (1.1 $\times$ 10^{29} SO_2 s^{-1} or 1.1 $\times$ 10^4 kg

s^{-1}) at the vent because gasdynamic similarity exists, which means that the number density contours should simply be scaled up by roughly two orders of magnitude if we use a two orders of magnitude higher influx ($\sim 10^6$ kg s^{-1}) as Moreno *et al.* (1991) did. That is, our plumes are already sufficiently dense that rarefaction effects would not alter the central density contours significantly. Therefore, if we ignore radiative coupling to the gasdynamics in the plume core when the gas density increases, the column density profile would also be scaled up by two orders of magnitude. Since this could not match observations of column density we believe that our influx conditions are a better simulation to reality than those of Moreno *et al.* (1991).

The vertical column density profiles for dayside Pele (*cf* Fig. 4.14) and Prometheus (*cf* Fig. 4.16) type plumes are plotted in fig 4.18 for comparison with the nightside profile. The column density profile for an undisturbed hydrostatic sublimation atmosphere at surface temperature of 115 K is also plotted. Note that the flat surface approximation is used here. It is seen that the sublimation atmosphere contributes appreciably to the column density and dominates at locations ~ 100 km away from the vent. There, the column densities of dayside plumes are *even less* than undisturbed hydrostatic sublimation atmosphere. This is caused by the "sweeping" of the upper part of the sublimation atmosphere by the plume bounce. The column density of the modeled dayside Pele averaged over a disk of radius 800 km is 7.61×10^{16} cm^{-2}. The column density of the modeled dayside Prometheus plume averaged over a disk of radius 500 km is 7.55×10^{16} cm^{-2}. Interestingly, these values
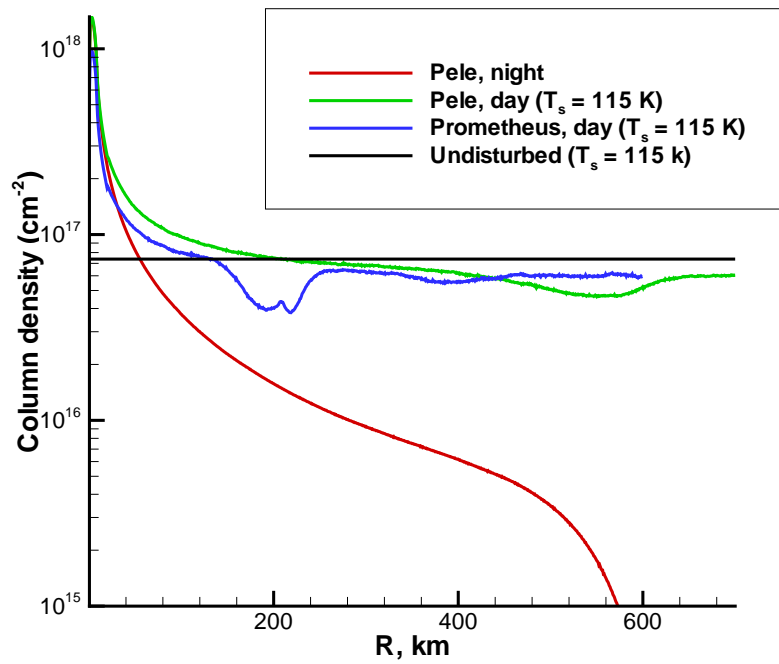
Figure 4.18: Column density profiles for Pele and Prometheus type plumes with column density of undisturbed sublimation atmosphere at surface temperature of 115 K overlayed.

are close to the sublimation atmosphere column density (7.38×10^{16} cm^{-2}) which implies that the enhancement of the column density near the plume axis and the reduction far away due to "sweeping" tend to cancel each other in a coarse spatial average. The average column densities are about a factor of two higher than the three sub-solar column densities ($\sim 1 - 4.5 \times 10^{16}$ cm^{-2}) obtained by Feldman *et al.* (2000) for three STIS (Space Telescope Imaging Spectrograph) observations. In their observation, Io subtended approximately 1 arc second and the angular resolution of the telescope camera was 0.0244×0.0244 arc seconds ($\sim 90 \times 90$ km). The higher average column density we obtain suggests that the sub-solar surface temperature of 115 K we assumed may in fact be a little high. A slightly lower sub-solar surface temperature ($\sim$113 K) reproduces the sub-solar column densities obtained by Feldman *et al.* (2000). However, it should be noted that the sub-solar column densities also depend on the frost coverage. A uniform frost coverage is assumed in all of our simulations. In reality, however, the frost is far from uniform and there thus could be the situation in which the sub-solar frost temperature is high but a broad-area-average column density is low.

The observed and simulated deposition patterns also agree reasonably well. The ring deposition around Pele forms one of the most dramatic surface marking on Io and can been seen in many published images of Io. As shown in the results above, our simulation of a nightside Pele plume suggests a very concentrated deposit in a ring with inner and outer diameters of $\sim$800 km and $\sim$1200 km, respectively, which agrees very well with the observations. When

84

the Pele plume is on the dayside, the deposition pattern is quite different (*cf* Fig. 4.2). As shown in our simulation, both the inwards and outwards turning flow could deplete some frost from the ring deposited at night and create deposits further inwards and outwards.

The most exciting result is the similarity between a shock at the top of the Pele plume suggested by Strom and Schneider (1982) and the canopy shock present in our simulation. The ultraviolet smoothed brightness images of Pele (*cf* Fig. 1.2) showed a bright top. Its shape strongly resembles that of our simulated canopy-shock. Strom and Schneider suggested that this bright envelope may be the result of a concentration of particles at a shock front. Our simulations indicate that such a canopy shaped shock should be present. As will be shown in the next Chapter, we find a possible concentration of very fine ($\sim$0.01–0.1 μm) particles at the shock front.

4.6   Is There also a Multiple Bounce Structure Around Pele?

It was initially expected that the multiple bounce structure around dayside Prometheus type plumes would also exist for dayside Pele type plume. It is expected that the Pele solution is just truncated by the limited size of the computational domain we used previously. With the incorporation of the new spherical geometry, we are now in the position to examine this supposition. The computational domain is extended quite far and the resulting modeled plume is shown in Fig. 4.19. As expected, multiple bounces do occur. However,
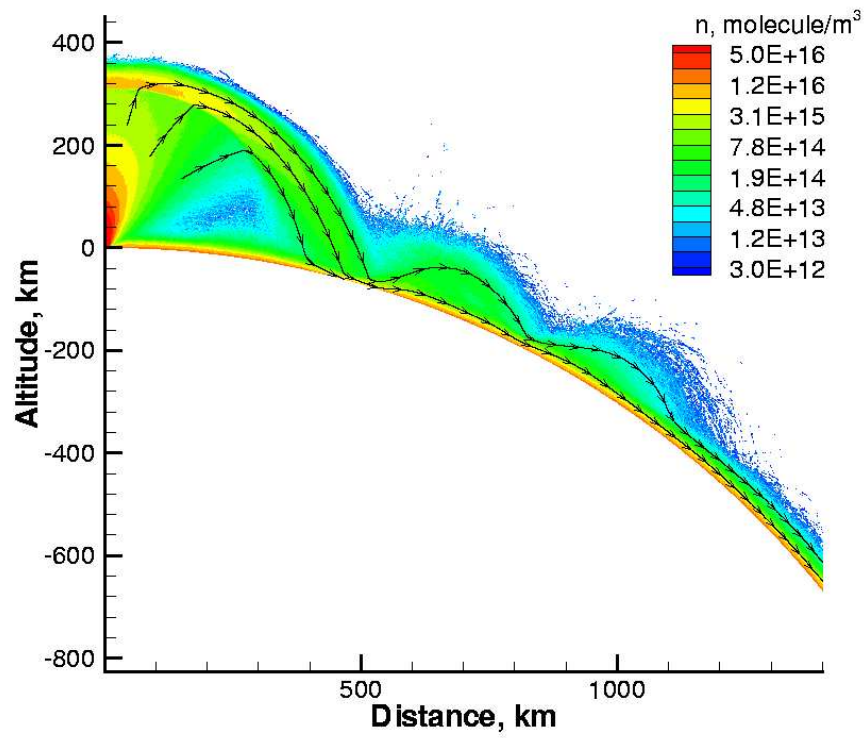
Figure 4.19: The number density contours of a simulated Pele type plume. The surface temperature is a nominal 110 K.

the plume gas becomes very diffuse by the time it reaches $R \sim 1000$ km after the first bounce. As a result, the SO_2 deposition there is also very diffuse and the peak deposition rate for the second bounce is about one order of magnitude lower than the peak value at the first bounce (*cf* Fig. 4.20). In fact, this may be the reason why no multiple rings are apparent around Pele. The SO_2 deposition rate at $R \sim 1000$ km away from the vent is simply too small and the surface could easily be modified by local volcanism or sublimation. Note that due to the large dimensions of Pele type plumes, the deposition flux at the main ring is already relatively small. It is generally about one order of magnitude lower than the deposition rate of a Prometheus type plume in its main (first) ring (*cf* Fig. 5.20). This dramatic difference is because the mass fluxes at the vents of both type of plumes are comparable but the surface area covered by the plume gas near the first ring of Pele type plume is a couple of orders of magnitude larger than that of Prometheus type plumes.

There are also several other interesting implications of the extreme diffuseness of the falling gas of Pele type plume. With the same sublimation atmosphere, the bounce (re-entry shock) occurs at higher altitude for a Pele type plume than it does for a Prometheus type plume. In another words, due to the greater density of the falling gas in a Prometheus type plume, the gas penetrates deeper into the sublimation atmosphere than does the thin falling gas in a Pele type plume. This can be seen by comparing Fig. 4.16 and Fig. 4.14. The re-entry shock heights are ~ 40 km for Pele and ~ 10 km for Prometheus.
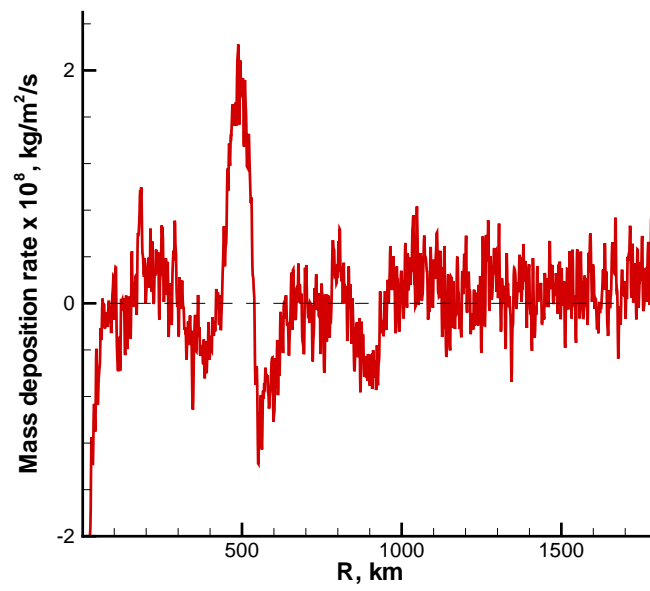
Figure 4.20: The mass deposition profile of the simulated Pele type plume shown in Fig. 4.19.

To justify our suggestion in previous Chapter as to the outer wall boundary conditions, we compare two cases (Fig. 4.19 and Fig. 4.21) with different domain sizes. It is in fact seen that the outer walls have been placed at far enough that the main plume and the bouncing region are insensitive to the outer wall boundary.

4.7 The Effects of New Features in the Model on the Earlier Result

Finally in this Chapter, the effects of new features in the model on the early result are examined. It has been shown in the previous Chapter that variable g tends to result in a higher and wider plume. On the other hand, the new model of emission from higher vibrational level tends to result in a lower and narrower plume due to the larger internal energy losses to space. As a result of this fortuitous canceling effect, the new vent conditions for a nominal Pele type plume are very similar to the early ones. A vent temperature of 650 K and a 10% lower vent velocity could produce a plume of Pele size, and the new and initial plumes are qualitatively very similar. This can be seen by comparing Fig. 4.22 with the corresponding Figs 4.1 and 4.3. Also, the deposition profile and the peak deposition rate are similar (Fig. 4.23).
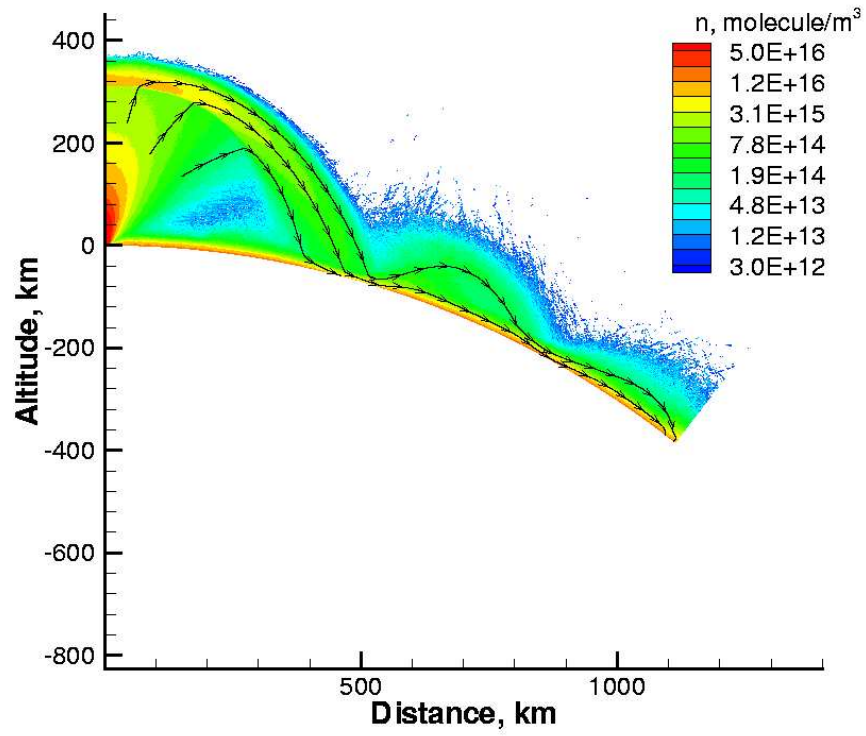
Figure 4.21: The number density contours of a simulated Pele type plume with the same conditions as the one shown in Fig. 4.19 except that the outer wall is placed at $R = 1200$ km. Note the insensitivity of the main plume and the first bounce to the position of the outer wall.

90
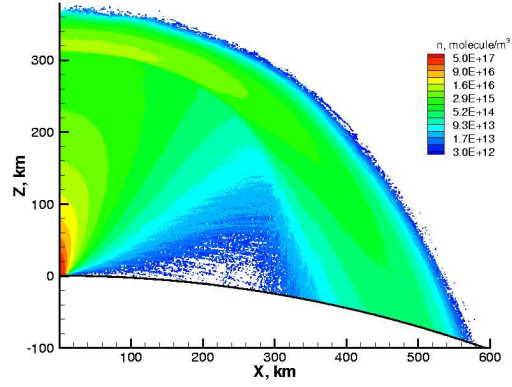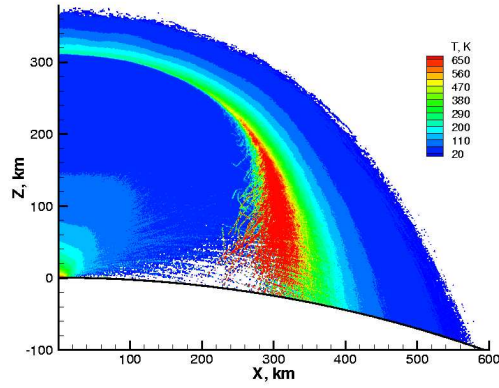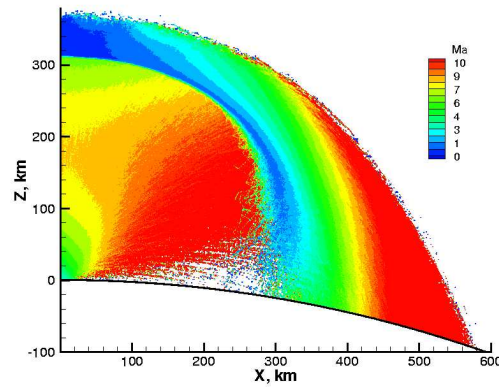
Figure 4.22: a) Number density, b) temperature and c) Mach number contours of a new simulated nominal Pele type plume. Note the velocity and temperature at the vent are 900 m/s and 650 K, respectively.
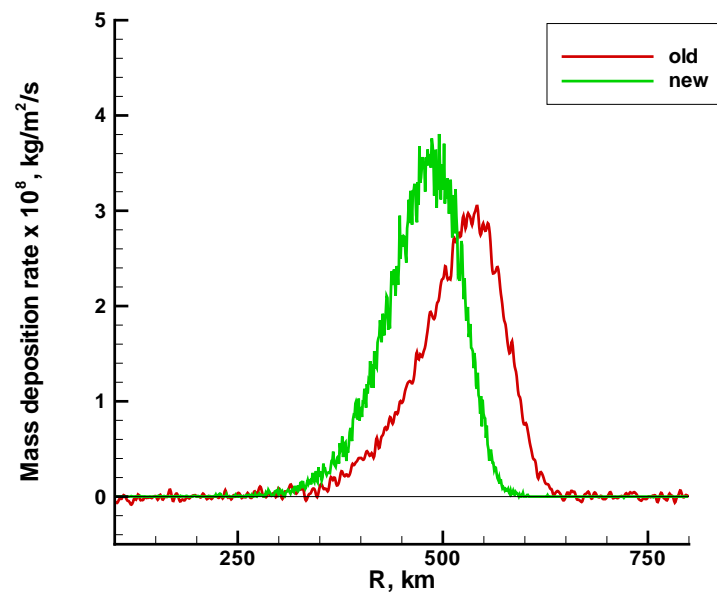
Figure 4.23: Comparison of deposition profiles between the early and new nominal nightside Pele type plumes.

Chapter 5

Parametric Studies and Matching Various Observations

5.1 Overview

A Parametric study of the vent conditions and comparisons of the simulations to observations are discussed in this chapter. Using the results of the parametric study, one can constrain the gas properties at the vent by observables, particularly the plume height and the radius of the surrounding condensation deposition ring. The flow of refractory 1 nm – 10 μm particulates entrained in the gas is modeled. The simulations of particle flow show encouraging matches to observed plume images, the shape of plume shadows and deposition patterns. Other issues such as the transport of S_2 and Na in a Pele type plume, the effect of the unsteadiness of the volcanic source, and the effect of a parabolic vent velocity profile are also discussed.

5.2 Parametric Study of Vent Temperature and Velocity

Two sets of contours (Fig. 5.1) in vent velocity-temperature (V_v-T_v) space are created from $\sim$40 individual simulations, with one set of contours corresponding to constant shock heights (H_s) and the other to constant ring
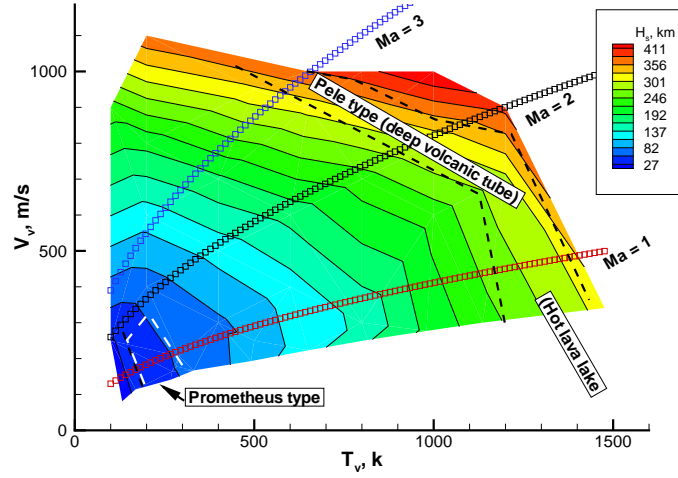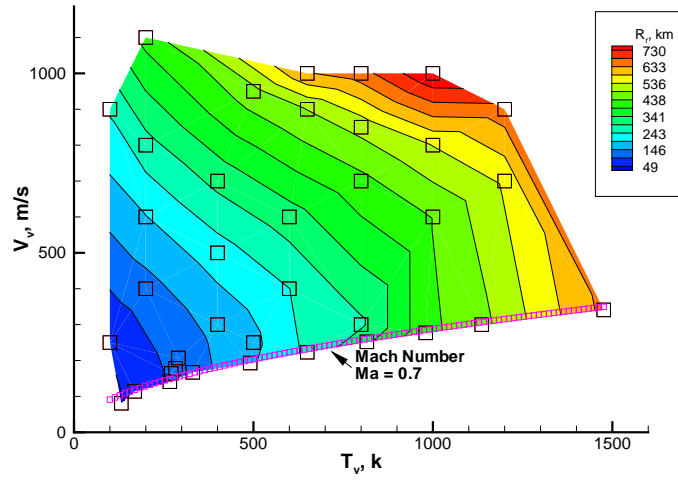
Figure 5.1: a) Constant plume height (H_s) and b) constant peak frost deposition radius (R_r) contours in vent velocity-temperature (V_v, T_v) space. Suitable regions of (V_v, T_v) for Pele- and Prometheus-type plumes are indicated. Vent conditions corresponding to Ma = 1, 2 and 3 are also shown by dotted curves in a). A bounding Ma number of 0.7 relevant to lava-lake plume is shown in b). The (V_v, T_v) at which the ∼40 individual simulations were performed are indicated by the square symbols in b).

positions (R_r, the peak deposition radius assuming a cold condensing surface[1]). As discussed in the Section 3.5 the assumptions in this parametric study include an $\sim$8 km "virtual" vent radius, a fixed source number density at the vent (5×10^{17} molecules/m^3), and an optically thin gas in the ν_1, ν_2, and ν_3 SO$_2$ vibrational bands. Also note that the simulations are performed using a single computational domain. As shown in Section 3.3 this is adequate for determining accurately the shock height and the peak deposition ring radius. Two sets of contours in vent velocity-temperature (V_v-T_v) space are shown in Figs. 5.1a and b. From these two sets of contours of shock height and peak deposition radius, it is possible to constrain the *unique* vent temperature and velocity for large plumes from an observed shock altitude and deposition ring radius at the intersection of R_r = constant and H_s = constant lines. Since the observed plume height (the maximum height of scatterers in the respective image) of Pele-type plumes ranges from $\sim$300 to 460 km (McEwen *et al.* 1998), and peak deposition radius from $\sim$500 to 620 km, a reasonable range for this type plume in (V_v, T_v) space is obtained by finding the region enclosed by contours of R_r = 500 and 620 km, and H_s = 260 and 360 km. This region is indicated in Fig. 5.1a by the band between two dashed black lines approximately corresponding to contours of R_r = 500 and 620 km. Note that our constraints are based on shock heights appropriate for the observed plume heights. The distinction between the two types of sources (deep volcanic vent

---

[1]As will be shown in Section 5.5.1, the diurnally averaged deposition profile has approximately the same peak deposition radius as that for nightside plume so the nightside deposition profile can be used to find the peak deposition radius.

and lava lake) and associated Mach number at the vent shown in Fig. 5.1a will be discussed further in Chapter 6. The bounding Mach number of ∼0.7 will be discussed in Appendix C. For small Prometheus type plumes, one cannot constrain (V_v, T_v) by this approach as the two sets of contours in Figs. 5.1a and b are essentially parallel to each other. In the absence of a usable result from the H_s/R_r plots for small plumes, other measures, such as radiation constraints, are necessary to determine the vent conditions more precisely. Despite this, we have attempted to constrain (V_v, T_v) combinations for Prometheus-type plumes as tightly as possible. These ranges are shown on Fig. 5.1a by a white dashed rectangle. The (V_v, T_v) values in this region produce plumes with shock heights of ∼35 to 50 km (plume heights of ∼60 to 80 km) and peak deposition radii of ∼65 to 105 km. These values are appropriate for Prometheus type plumes (Strom and Schneider 1982).

Note that our constrained vent velocity for the Prometheus plume is significantly smaller than the free molecular ballistic estimate of 500 m/s by Strom and Schneider (1982) based on the plume height of ∼65 km. Because it neglects the gas dynamic shock, the ballistic approximation is clearly inadequate for estimating the vent velocity, and its accuracy is especially poor at high T_v when the high internal energy of the gas and intermolecular collisions contribute appreciably to the development of the plume. The gas flow is accelerated through the conversion of internal energy to kinetic energy during the expansion of the flow. This causes the molecules to rise higher than the ballistic height and to fall further from the vent.
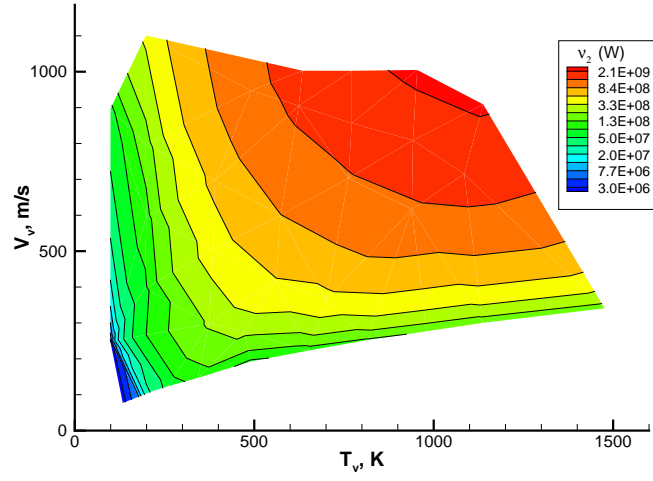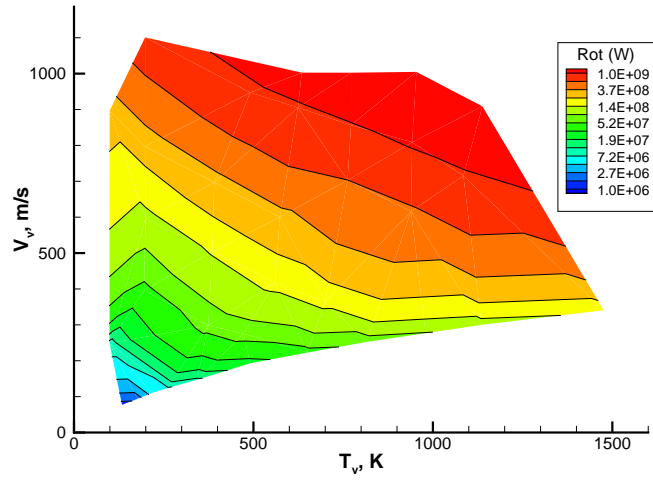
Figure 5.2: Contours of total emission power of a) ν_2 vibrational band and b) overall rotational lines in vent velocity-temperature (V_v, T_v) space.
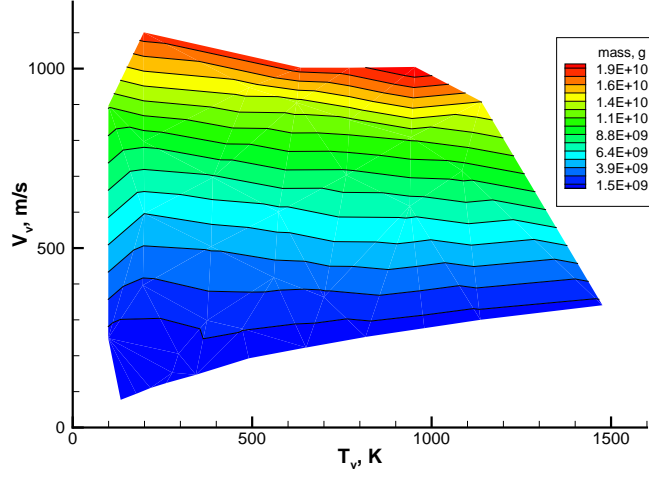
Figure 5.3: Contours of total mass in vent velocity-temperature (V_v, T_v) space.
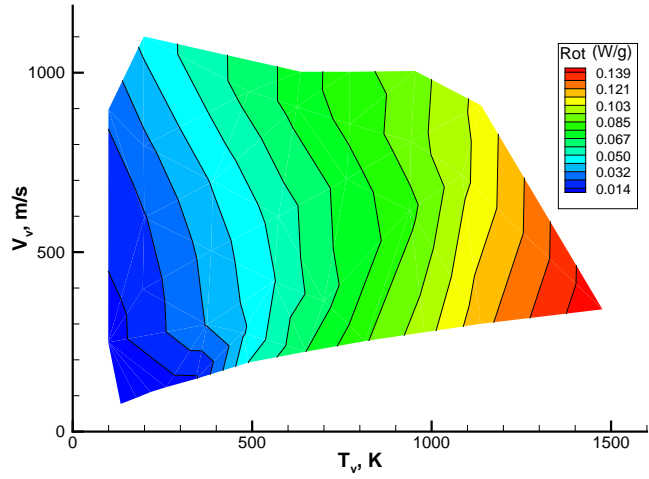
Figure 5.4: Contours of specific emission power of the overall rotational lines in vent velocity-temperature (V_v, T_v) space.

As pointed out above, radiation constraints are necessary to determine the vent conditions more precisely in some circumstances. Thus, contours of emission power in the (V_v, T_v) space are also created in this parametric study. Figures 5.2a and b show the contours of total (volume integrated) emission power from the ν_2 vibrational band and overall rotational lines of SO_2. It is seen that the Prometheus type plumes can be distinguished from Pele type plumes not only by the plume shape but also by the total emission power. There is approximately a two orders of magnitude difference in the total emitted power. It may also be possible to distinguish the source mechanisms (lava lake or volcanic tube) based on these emission contours since the lava lake plumes generally emit several times as much as the volcanic tube plumes.

It should be pointed out, however, the total power depends on the total mass in the plume and ultimately the mass flow rate at the vent. As already specified, in this parametric study, the vent radius is fixed at 8.4 km and the number density at the vent is fixed at 5.0 $\times 10^{17}/m^3$ for a volcanic tube plume. Similar values are used for lava lake plume[2]. As discussed in the previous chapter, this vent number density combined with vent radius of 8.4 km appears to be quite appropriate for volcanic plumes on Io in general. The contours of the total plume mass in the V_v-T_v space are plotted in Fig. 5.3. Combining this figure with Figs. 5.2a and b, it is observed that the high total emission power from large Pele type plumes results partly from the large total

---

[2]The difference in the vent conditions that are specified for a lava lake plume will be discussed in Chapter 6.

mass they contain in addition to the generally high vent temperatures.

Note that the total mass of SO_2 gas in our simulated Pele type plume ($\sim 1 \times 10^{10}$ g) is about one order of magnitude lower than that constrained by Spencer *et al.* (1997). As will be discussed in Section 5.3.4, the simulated gas TCD of $\sim 2 \times 10^{17}$ cm^{-2} near Pele's shock is consistent with the SO_2 gas tangential column abundance of $\sim 3.7 \times 10^{17}$ cm^{-2} obtained by Spencer *et al.* (1997) based on an HST observation. Spencer *et al.* (1997) assumed a uniform hemispherical gas plume, the one order of magnitude higher gas mass may be due to their very crude assumption. Specific emission contours are also helpful and are shown in Figs 5.4 for the rotational lines. These contours are obtained by dividing the total emission power by the total mass of each plume. In these specific emission contours, the effect of the mass flow rate dependence is canceled in an average sense and the temperature dependence of emission power is seen more clearly.

In this parametric study, the number density at the vent, n_v, a third free parameter, has been kept fixed. This is because, as mentioned in Section 3.5, the gas flow fields with different n_v appear to have approximately the same contour shapes: the contour levels are simply scaled by the source number densities. For example, Figures 5.5b–d show the number density contours, normalized by n_v, for three plumes with the same (V_v, T_v) of (200 m/s, 180 K) but different vent number densities ranging from 5×10^{17}/m^3 to 2×10^{18}/m^3. It is seen that the three contours look almost the same. This kind of gas dynamic similarity has been tested for several (V_v, T_v) combinations

100
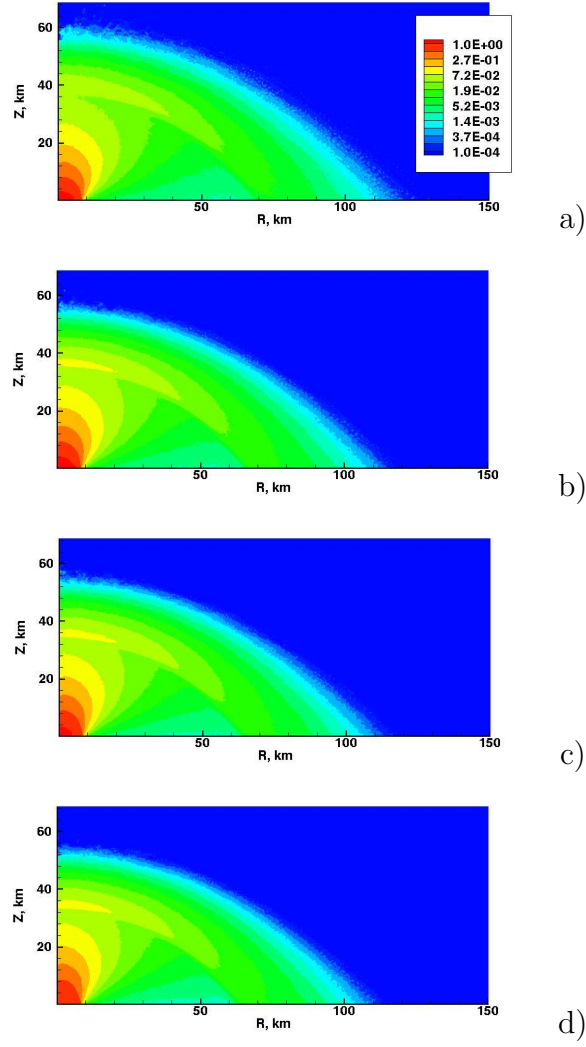
Figure 5.5: Number density contours (normalized by the vent number density) of plumes with vent number density of (a) $5. \times 10^{16}/\text{m}^3$ (b) $5. \times 10^{17}/\text{m}^3$, (c) $1. \times 10^{18}/\text{m}^3$, and (d) $2. \times 10^{18}/\text{m}^3$.

101

and is expected to hold for virtually the entire range of the parametric study. However, for this gas dynamic similarity to exist, it is necessary for the flow in the vent vicinity to be in the continuum regime ($Kn < 10^{-4}$ based on vent diameter in our case). For more rarefied vent flows ($Kn \sim 10^{-3}$), the normalized gas density flow field looks different as can be seen by comparing Fig. 5.5a ($n_v = 5 \times 10^{16}/\text{m}^3$) with Figs. 5.5b-d. The lower inter-molecular collision rate and thus lower radiation losses for lower vent number density causes the plume to retain more translational energy and thus to rise higher and expand more widely.

Because of the virtual independence of plume shape on n_v as long as the near vent flow is near continuum, n_v cannot be constrained by shock height and ring radius observations. An estimate of efflux based on an observed column density or resurfacing rate would be desirable to constrain n_v after the vent diameter and V_v are constrained. For example, an efflux of 1.1×10^{29} SO$_2$ molecules s^{-1} is found to be consistent with observations at Pele. Hence, if V_v is constrained to be $\sim$1000 m/s, then the vent number density is estimated to be around 5×10^{17} SO$_2$/m^3. A different method to constrain the vent number density is examined in Section 5.3.1.
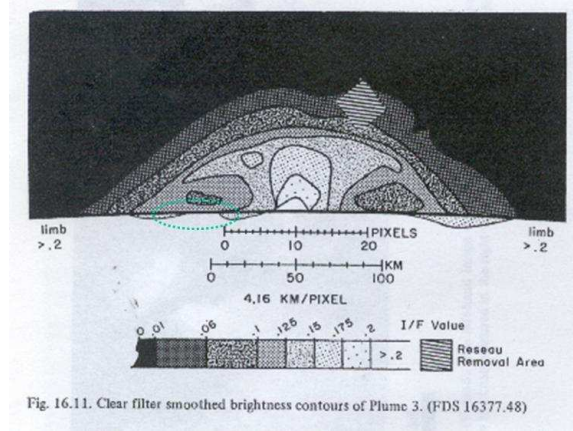
a)
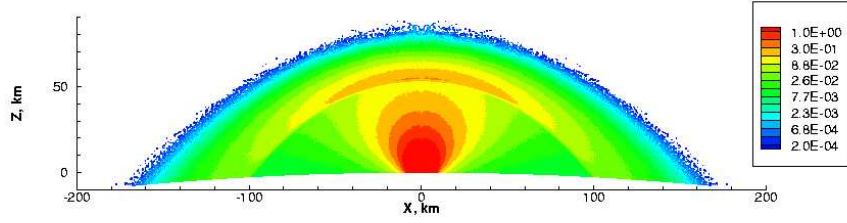
b)
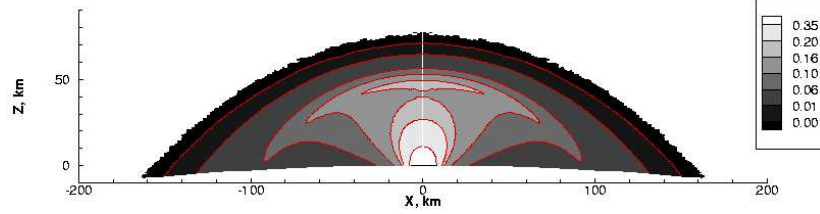
c)

Figure 5.6: (a) Voyager image of the brightness of Prometheus plume, (*From Strom and Schneider (1982), courtesy of Robert Strom*) (b) the number density contours (normalized by $5 \times 10^{16} m^{-3}$) of the modeled Prometheus gas plume and (c) the gas TCD (normalized by $6 \times 10^{17} cm^{-2}$) for the modeled plume. All three figures are drawn to the same length scale.

5.3 Matching Plume, Shadow and Deposition Ring Images

5.3.1 Reproducing Voyager Images of Prometheus Plume

Several vent conditions (Fig. 5.1) were tried and found to produce a good fit to the gas plume shape (height and canopy diameter) for the Prometheus plume observed by Voyager (Strom and Schneider 1982). The source of Prometheus is 5° in front of the limb of Io during the observation (Strom and Schneider 1982). A Prometheus type plume with an evaporating lava lake[3] at 350 K ((V_v, T_v) of (140 m/s, $\sim$300 K)) as the source was chosen. Note that the difference in the temperatures of the lava lake and the gas will be explained in Appendix C. The resulting plume with this vent condition and a low surrounding frost surface temperature of $T_s = 90$ K is shown in Fig. 5.6b. It is understood that the Voyager images were taken during Ionian day time. The simulated plume image at higher surface temperature will be discussed below. To make a more meaningful comparison to the observation of Strom and Schneider (1982) shown in Fig. 5.6a, one needs to calculate the plume column density along the line-of-sight, since the brightness of a plume depends on column density of scattering particles. Equation (5.1) (Collins 1981) shows the relation between the observed reflectivity and the gas column density for Rayleigh-scattering:

$$Nl = \frac{2N_0^2\lambda^4(I/F)}{\pi^3(n^2-1)^2(1+cos^2\theta)} \tag{5.1}$$

---

[3]See Chapter 6 for more details.

where Nl is the observed column density of the gas (in molecules/m^2), N_0 is the gas reference number density (2.68×10^{25} molecules/m^3) at 0°C and 1013 mbar, λ is the wavelength of the scattered light (m), I/F is π times the measured radiance/solar irradiance at λ, n is the index of refraction of the gas (at 0°C and 1013 mbar, a function of λ), and θ is the phase (scattering) angle. Equation (5.2) is for Rayleigh-like scattering by very small particles of radius $r < 0.03\lambda$:

$$Nl = \frac{\lambda^4(I/F)}{8\pi^5 r^6(1 + cos^2\theta)}\left(\frac{n_p^2 + 2}{n_p^2 - 1}\right)^2 \qquad (5.2)$$

where Nl is the observed particle abundance (in particles/m^2), r is the mean particle radius (m) and n_p is the index of refraction of the particle material. These two equations show that the brightness of a plume is proportional to the column density along the line-of-sight whether the scatterers are gas molecules or small particles. Thus, assuming any entrained particles move with the gas, our gas column density contours could be interpreted as scattered sunlight brightness contours with some proportionality constant. Since we have already obtained the gas density field (in molecules/m^3), the column density along lines-of-sight can be readily calculated via cell-by-cell integration (Fig. 5.6c). Note that the 5° offset of the source of Prometheus from the limb of Io is taken into account. It is seen that the total gas TCD contours show very encouraging similarities to the Voyager image. In addition to the general shapes and dimensions of the contours, the "hatchet" shape of the contours near the gas shock seen in both the observations and the simulation

105

is promising.

It is understood that the observed plume brightness probably arises from scattering of sunlight by fine particulates (refractory or volatile) rather than by the gas. In fact, Collins (1981) analyzed the Voyager images of Loki and concluded that the UV brightness of the outer plume cannot be explained by Rayleigh-scattering from the gas but may instead be explained by the Rayleigh-like scattering of very small particles with radii of 1.0 – 10 nm. Thus, the transport of fine 1 – 100 nm *refractory crystal or droplet-like* particles entrained in modeled gas plumes is examined next. It is found that nano-sized particles tend to track the gas flow well. This tracking is shown in Figs. 5.7a and b which compare the streamlines of the gas and particle flow. The background gas flow in these two figures is the same as that in Fig. 3.13 with a surface temperature of 110 K and is intended to show the response of these particles to the gas "bounce". It is seen that nano-sized particles easily track the gas flow and some 1 nm particles from the very outer portion follow the gasdynamic bounce along with the gas, although they depart from the gas flow streamlines. That is, the turning flow near the re-entry shock acts like a cyclone separator: the larger particles are sorted from the small ones. Larger particles are less responsive to the accelerating gas flow (*cf* Fig. 3.13).

The flow fields of particles in the modeled nightside Prometheus plume shown in Fig. 5.6b were then calculated: it was hoped that the TCDs of nano-sized particles would resemble the gas plume TCD and match the Voyager image since nano-sized particles tend to track the gas flow well. Figs. 5.8a-e
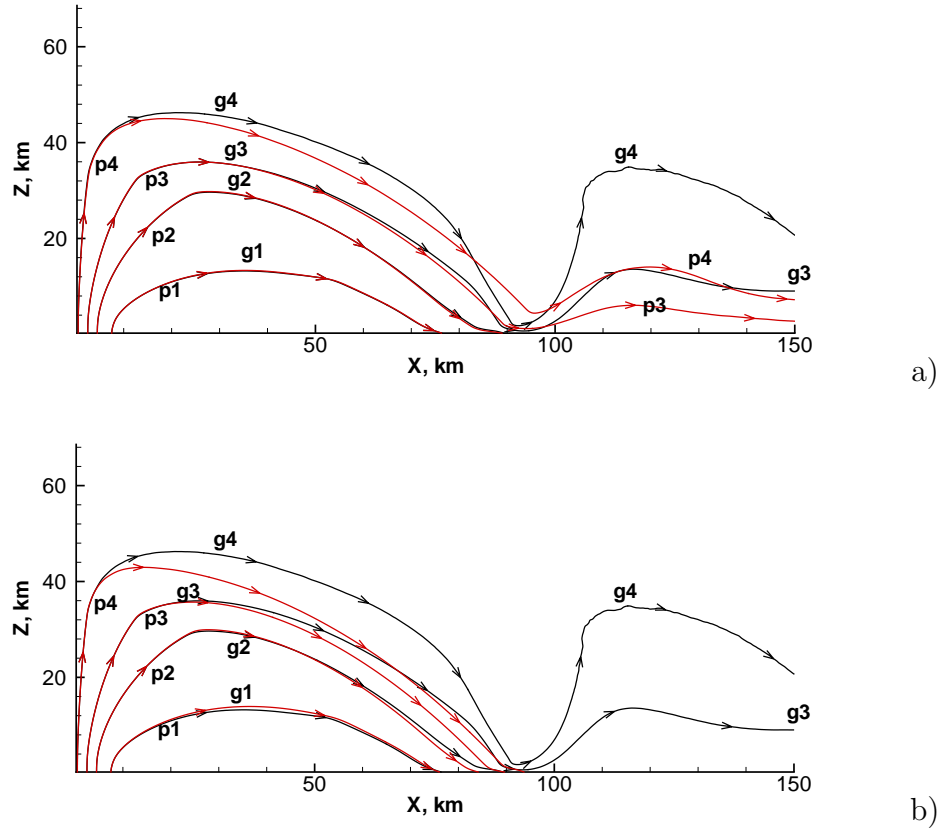
Figure 5.7: Comparison of streamlines of gas flow (black lines) and that of particles (red lines) of different sizes: a) 1 nm and b) 3nm. Notice how some of the smaller particles in a) bounce with the gas.
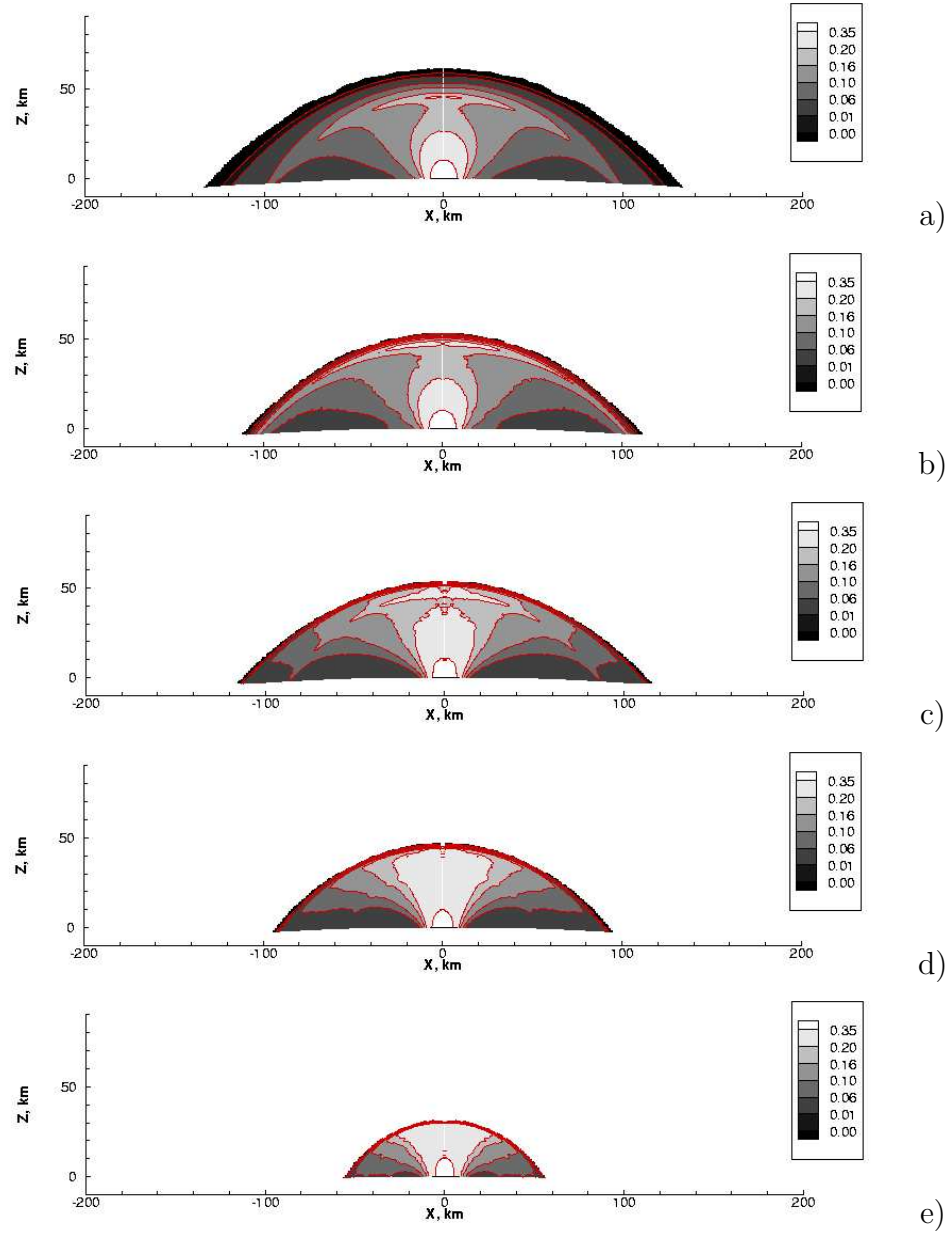
Figure 5.8: The tangential column density (TCD) of (a) 1 nm , (b) 3 nm, (c) 10 nm, (d) 30 nm and (e) 100 nm refractory particles entrained in the gas plume shown in Fig. 5.6b. Cases a) and b) were calculated by the Collision Model, and the others by the Drag Model.

show the TCD of particles of different sizes. As expected, the TCD images of nano-sized refractory particle plumes indeed show convincing similarities to the Voyager image. Figure 5.8c shows that the particle TCD differs from the Voyager image for ∼10 nm particles, especially in the outer portion of the plume (beyond the gas canopy shock): the width and the height of the particle plume decrease and the contours at high altitude coalesce. The differences in the outer portion of the plume between the TCD contours and the Voyager image in Fig. 5.6a become larger as the particle size is further increased (*cf* Figs. 5.8d and e). Thus, Fig. 5.8 suggests that most of the particles entrained in the *outer* portion of the Prometheus plume are smaller than ∼10 nm. This is consistent with the photometric analysis of the Voyager image of the similar plume Loki by Collins (1981). He suggested that in the outer portion of Loki, particles are extremely fine with radii of less than ∼10 nm. Since particles with such small sizes tend to track the gas flow well, it is reasonable to use the observed plume shape (height and canopy diameter), visualized by scattering from extremely fine particles, to constrain vent conditions by matching the modeled *gas* flow to the observed particle plume shape. The discussion above does not exclude the existence of larger particles, especially in the vent vicinity. Collins (1981), in fact, suggested that in the reddish inner portion of Loki the ejecta may consist of larger particles (1–1000 μm).

It should be pointed out that the number density of the gas at the vent influences how large the particles can be and still track the gas flow. As shown in Fig. 5.5, if the source number density of the gas is changed, the gas flow

109
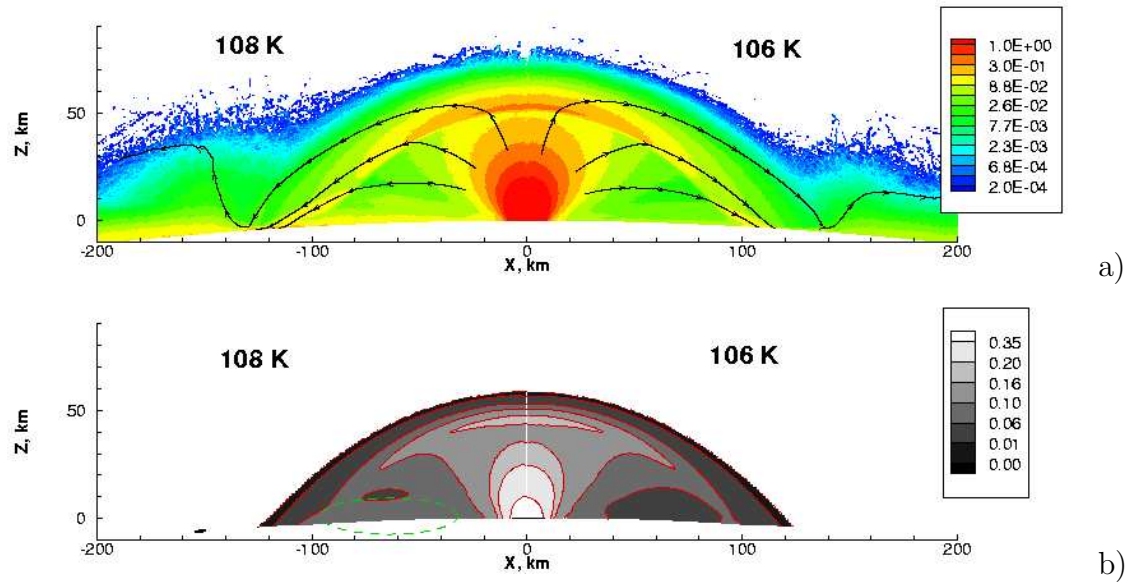
Figure 5.9: (a) Number density contours of gas plume with surface temperature
of 108 K (left) and 106 K (right), (b) the TCD of 1 nm spherical particles
entrained in these gas plumes. Note the low altitude "dust cloud" indicated
by dashed oval.

would still have roughly the same contour shapes but the contour levels would scale proportionally. A particle with a radius r would have a certain trajectory, say, trajectory "p2" in Fig. 5.7, in the gas flow for a particular source number density. If, for a fixed source velocity, the source number density of the gas is increased by some factor N, a particle of size Nr starting at the same point would then have approximately the same trajectory as "p2". This is because, for free molecular drag, the gasdynamic acceleration of a spherical particle is proportional to n/r, where n is the gas number density. Thus, it is possible that larger particles could track the gas flow if the source gas number density were larger than expected. This feature, in fact, provides another possible constraint on the gas source number density. Since our $\sim$10 nm limit is consistent with the Voyager observation of Loki analyzed by Collins (1981), the gas source number density used herein should also be fairly realistic. Future observations of the gas column density at Prometheus would provide additional constraints on the gas source number density.

A relatively high brightness near the surface (the *lighter* shading region indicated by a dashed oval in Fig. 5.6a) is seen in the Voyager image of Prometheus indicating a slightly higher particle column density there. This feature can also be reproduced by a plume of nano-size particles at a slightly higher surface temperature. The left hand side of Fig. 5.9b illustrates a plume of 1 nm particles entrained in the modeled Prometheus plume (Fig. 5.9a (left)) with surface temperature $T_s = 108$ K. A "bounce" of a portion of the falling gas from the top of the canopy is seen in Fig. 5.9a (left). The levitation of

(a)

(b)

(c)

(d)

(e)
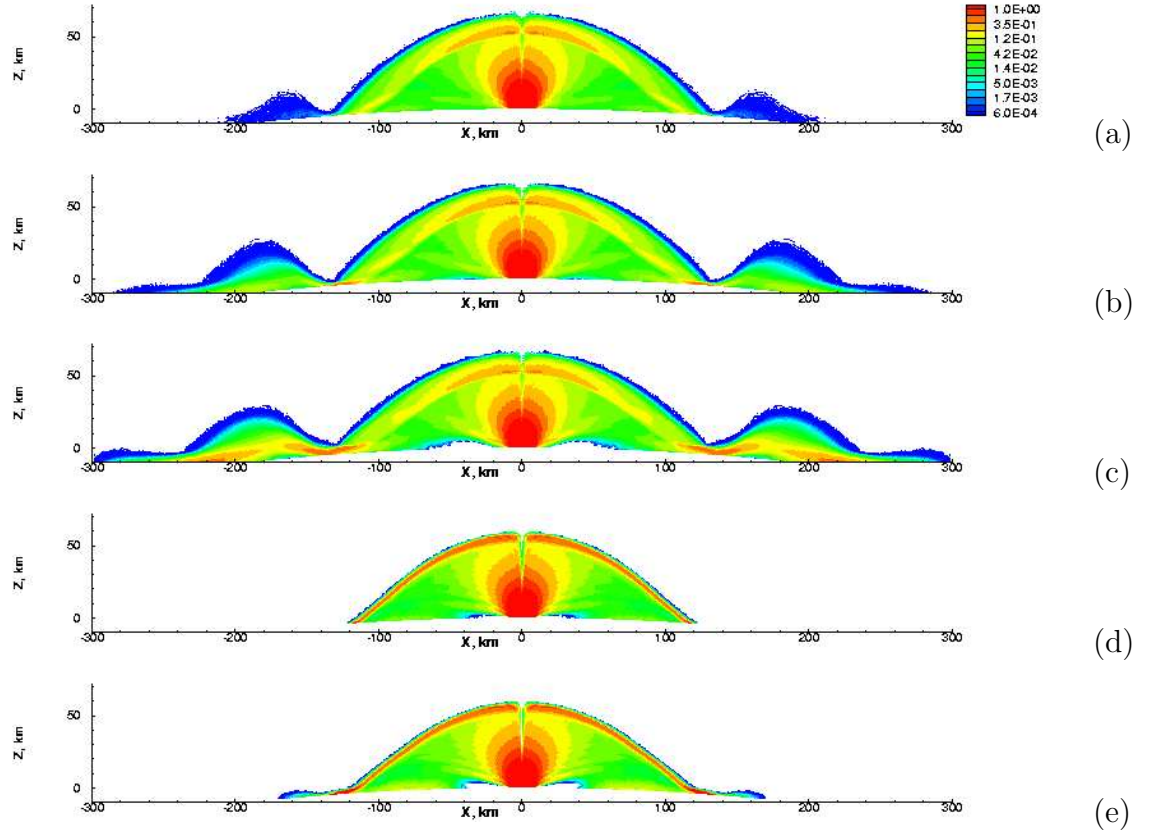
Figure 5.10: a)–c) The normalized number density (by vent number density) contours of 1nm dust in Prometheus gas plumes at $T_{surface} =$ (a) 108 K, (b) 110 K, and (c) 112 K; d) and e) for 3nm dust in gas plumes at $T_{surface} = 110$ K and 112 K, respectively.

1 nm particles by the bouncing gas and their gradual descent through the subliming atmosphere results in the higher particle column density near the surface. Note that the higher particle column density in the region indicated by a dashed oval in Fig. 5.9b (left) is due to the projection of the axisymmetric plume flow in the calculation of TCD. In addition, Fig. 5.9b shows that the Voyager image of Prometheus is best reproduced by plumes of 1 nm particles entrained in the modeled Prometheus gas plumes with slightly different surface temperatures on the left and right hand sides.

The levitation of small particles by the bouncing gas flow is more dramatic around gas plumes over a warmer surface. This is shown in Fig. 5.10 by the number density contours, normalized by vent number density, of nano-sized particles in Prometheus gas plumes at different surface temperatures. The corresponding TCD of these plumes are shown in Fig. 5.11. It is seen that the more dense sublimation atmosphere at high values of $T_{surface}$ supports larger particles, and is responsible for a possible formation of a dust cloud. "Feet" (lateral extension from the main plume) appear in some of the TCDs either when the surface temperatures are high[4] or the particles are small. There is, in fact, observational evidence suggesting the existence of such "feet" as seen later in Fig. 1.1a showing the Pillan plume at almost zero solar zenith angle. As will be discussed later, the deposition of these suspended particles at large distances from the vent might be the cause of the multiple rings observed

[4]We refer to 112 K as a "high" surface temperature because the equilibrium vapor pressure of SO_2 doubles when the surface temperature increases from 110 K to 112 K.
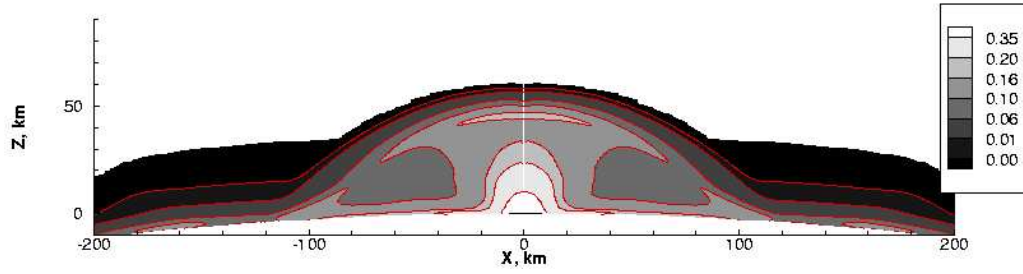
110 K, 1nm
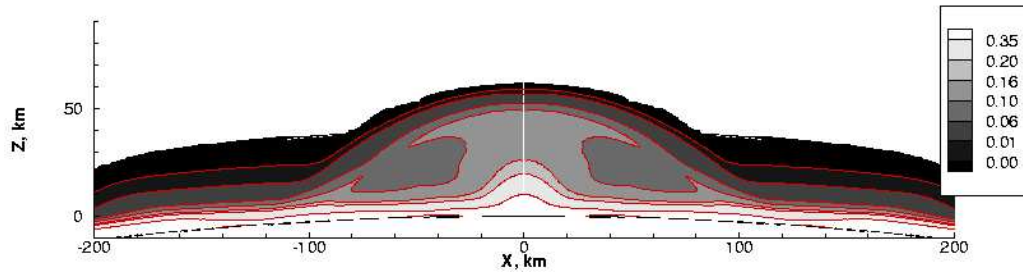
112 K, 1nm
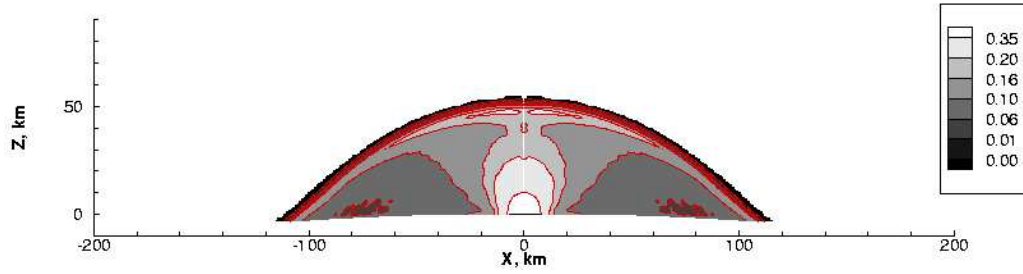
110 K, 3nm
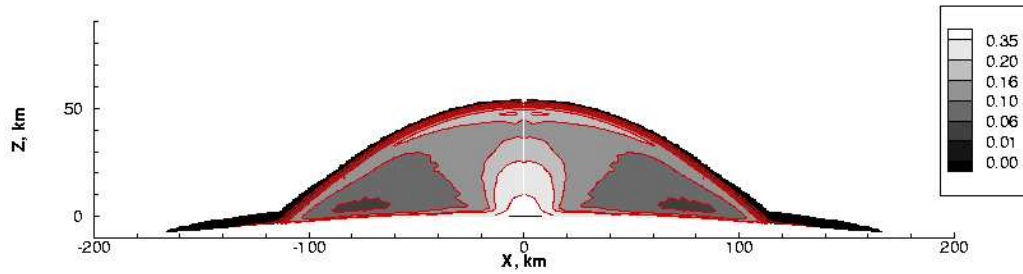
112 K, 3nm

Figure 5.11: a) and b) The normalized TCD of 1nm dust at $T_{surface} = 110$ K and 112 K, respectively; c) and d) 3nm dust at $T_{surface} =$ at 110 K and 112 K, respectively.

around Prometheus (Geissler *et al.* 2003).

5.3.2 Settling Time and Implications of Subsolar Frost Temperature on Io

As suggested above, visible dust clouds might be formed as the result of the "bounce" of small particles along with gas flows. If various plumes are continuously injecting very small particles into the region well above any sublimation atmosphere, one could anticipate the formation of thin dust clouds as particles gradually fall to the surface. No such clouds have been reported. We examine this question next.

The falling time of particles with different sizes starting at rest at 100 km above the surface in an isothermal, hydrostatic, sublimation atmosphere is here defined as the settling time and determined numerically for different surface temperatures. The particle equation of motion is:

$$-mg + \frac{1}{2}C_d\rho u^2\sigma = m\frac{du}{dt} \tag{5.3}$$

where m is the mass of a particles, g is gravitational acceleration on Io (1.8 m/s^2), C_d is the free molecular drag coefficient (eqn 7.71 in Bird (1994)), $\rho = \rho_0 e^{-z/L}$ is the local mass density of the atmosphere, u is the vertical velocity of the particle, $L = RT/g$ is the scale height of the isothermal sublimation atmosphere and σ is the cross-sectional area of particle. Fig. 5.12 is a semi-log plot illustrating the results of this calculation. The settling times are plotted in the figure as a function of surface temperature for particles of different sizes. As expected, the smaller the particle or the higher the surface temperature, the
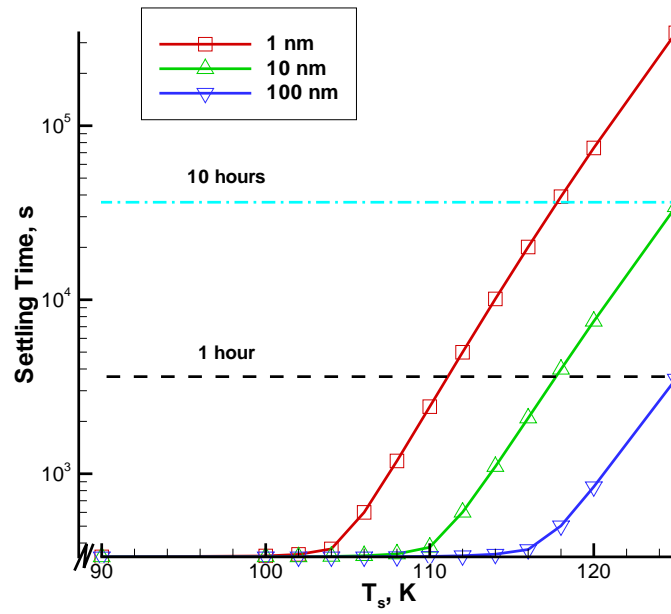
Figure 5.12: Settling time of particles of different sizes at different surface temperatures. A one hour settling time is comparable to the flow times associated with a plume while a 10 hour time is comparable to the times surrounding noon when the sunlit surface is warmest.

longer the settling time. At very low surface temperatures, particles fall almost ballistically in ∼200 s since the sublimation atmosphere is very tenuous. At high surface temperatures, the settling time increases approximately exponentially with surface temperature. The exponential dependence starts at lower surface temperature for smaller particles. The location of settling time equal to ten hours (corresponding to about a quarter of an Ionian day) is indicated in Fig. 5.12 by a dash-dotted line. The intersection of this line with the settling time profiles for potentially observable particles provides some constraints for subsolar frost temperature. If the particles in the "bounce" are observable, the absence of a more distant dust cloud on Io implies that the settling time of particles is small compared to the duration of Ionian day. Since the "feet" that appear in some of the TCD contours shown in Fig. 5.11 have comparable brightness to the plume itself, the particle cloud should be observable if the plume is. Therefore, the absence of dust clouds on Io seems to indicate that the subsolar surface temperature is relatively low. For example, if a cloud of 1 nm particles is potentially observable, the intersection of ten hour line and settling time line for 1 nm particles in Fig. 5.12 shows that the subsolar frost temperature is lower than ∼118 K.

Our assumptions about particle temperature and the nature of gas-particle collisions affect the free molecular drag coefficient C_d. In the above calculations, it is assumed that particles are cold and the gas-particle collisions are specular. Different assumptions lead to somewhat different drag coefficients. Fortunately, the constraints on subsolar surface temperature sug-

gested by Fig. 5.12 based on different assumptions for drag coefficient do not vary by more ∼1%.

5.3.3   Particle Flow in a Pele type Plume

Figure 5.13 shows the shapes of the gas and particle jets. The gas density contours and the particle locations are plotted, the latter represented by small dots. Note that the particles are simply initially placed in the flow at the vent orifice at zero velocity and the gas flow drags them upward. Several interesting features appear as the particle size increases. The first remarkable feature is that a concentration of particles at or near the canopy shock clearly appears for d = 0.01 μm particles. Further calculations show that such accumulation occurs for particles up to 0.1 μm (though below the shock). These results provide strong support to Strom and Schneider's suggestion as to the cause of the bright envelope appearing in the ultraviolet smoothed brightness images of Pele and also agree with the size range of the outer ultraviolet component found by Collins (1981). Also interesting is the relatively distinct underside of the outer portion of the particulate canopy (labeled A). This feature will be explained in the discussion of Fig. 5.14. In the three parts of Fig. 5.13 one can see the large differences in particle deposition patterns for different particle sizes. For smaller sizes (∼0.01 μm), the motion of the particles is strongly coupled with that of the gas so the range of deposition of falling particles is relatively narrow and within the band where the gas condenses. As the particle size increases, the particle deposition band is broadened and moves
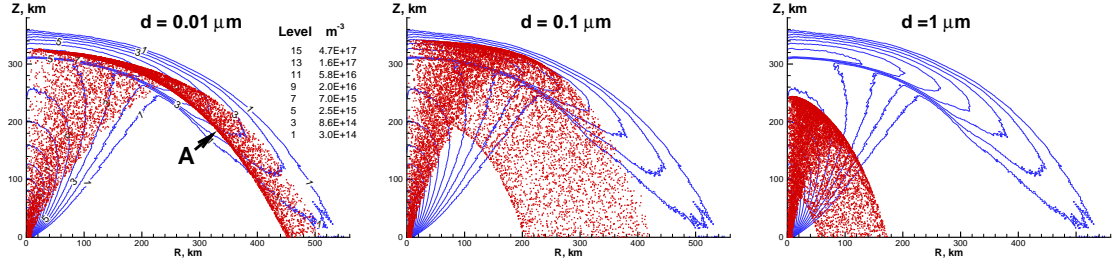
Figure 5.13: Shape of the gas and particle jets for different particle sizes (d = 0.01, 0.1 and 1 μm). Note that particle locations are represented by small dots.

inward. Larger particles ($\sim$1 μm) do not follow the gas well and their motions are much less influenced by the gas once they leave the near-vent region. They do not reach the canopy shock (as the smaller particles do) and they fall close to the vent. No other notable features appear for particles with a size larger than 1 μm. Generally, the larger the particles, the lower they rise and the closer to the vent they land. The largest particles that could be entrained in our simulated plume are $\sim$30 μm. This was determined by equating drag to weight, where weight $= mg$ and drag $= C_d \frac{1}{2}\rho u_v^2 \sigma$. Here, ρ and u_v are the gas density and the freestream velocity at the vent.

To examine how the above features are formed, we ran a parametric study on the trajectories of particles with sizes between 0.01 and 0.05 μm. Figure 5.14 shows those trajectories and the gas density contours. Insets showing the vicinity of the canopy shock are also plotted. The motions of the particles show few differences before they reach the canopy shock: they all reach and cross the shock, and are slowed down by the shock. This slowing down in the

motions of particles results in the concentration of particles near the shock. Particles in the size range 0.01–0.02 μm cross the shock, reach a maximum altitude, and then begin to fall under the action of gravity. The falling particles are dragged outward by the gas shear flow created between the rising and falling gas. The particle trajectories tend to cluster along density isocontours, and this creates a distinct underside to the particle canopy (labeled A in Fig 5.13). As might be expected the larger particle trajectories cluster at lower altitudes closer to the canopy shock. Larger particles (0.05 μm) have somewhat different trajectories. Because of their inertia, they are not slowed down as much by the shock, and thus reach *higher* maximum elevations before falling back towards the surface. The drag of the flow on these falling particles turns them outwards but they re-cross the shock before the trajectories are clustered by the upcoming supersonic gas at lower altitudes. As will be shown in the next section, the concentration of particles near these turning points forms a relatively distinct second shock-like structure.

In reality, a wide range of particle sizes is expected in the plume, so a distinct particle canopy would not be observed. However, the calculations indicate that there will be a sorting of the particles by size away from the vent and on the surface, with finer particles falling further away. Large particles stay close to the plume axis and form a dense column. Scattering from these particles may be the reason why one sees a bright column in sunlight in many Galileo plume images (e.g. Fig. 1.1). However, this does not mean that the gas plume stays only in a column and does not expand much, so one should be

careful and specific when interpreting the shape of the plume based on these images.

Note that the flat surface and constant g approximations were used in the simulations discussed in this subsection.

5.3.4 Reproducing Voyager Images of Pele Plume

The particle number density and the TCD of the particles were computed for comparison with the Voyager image. First, since our gas TCD of Prometheus appears to be very similar to the Voyager image of this plume (Fig. 5.6a), the same calculation was done for the Pele plume and similarities between the calculation and observation were sought. Figure 5.15 shows such a comparison. Note that the 10° distance of Pele center behind the limb when the Pele image was taken by Voyager is taken into account in all the TCD calculations in this section. One sees that the calculated gas TCD contours are indeed qualitatively quite similar to the brightness contours in the Voyager image, especially near the shock. Such a distinct shock feature does not appear in the Voyager image of Prometheus (*cf* Fig. 5.6b). The relatively small variation in number density near the shock in Prometheus hides the existence of a gas shock in the TCD. We observe that the simulated TCD of $\sim 2 \times 10^{17}$ cm^{-2} near Pele's shock is consistent with the SO_2 gas column abundance of $\sim 3.7 \times 10^{17}$ cm^{-2} obtained by Spencer *et al.* (1997) based on an HST observation but assuming a uniform hemispherical gas plume.

The TCDs for entrained fine refractory particulates are shown in Fig. 5.16.

121
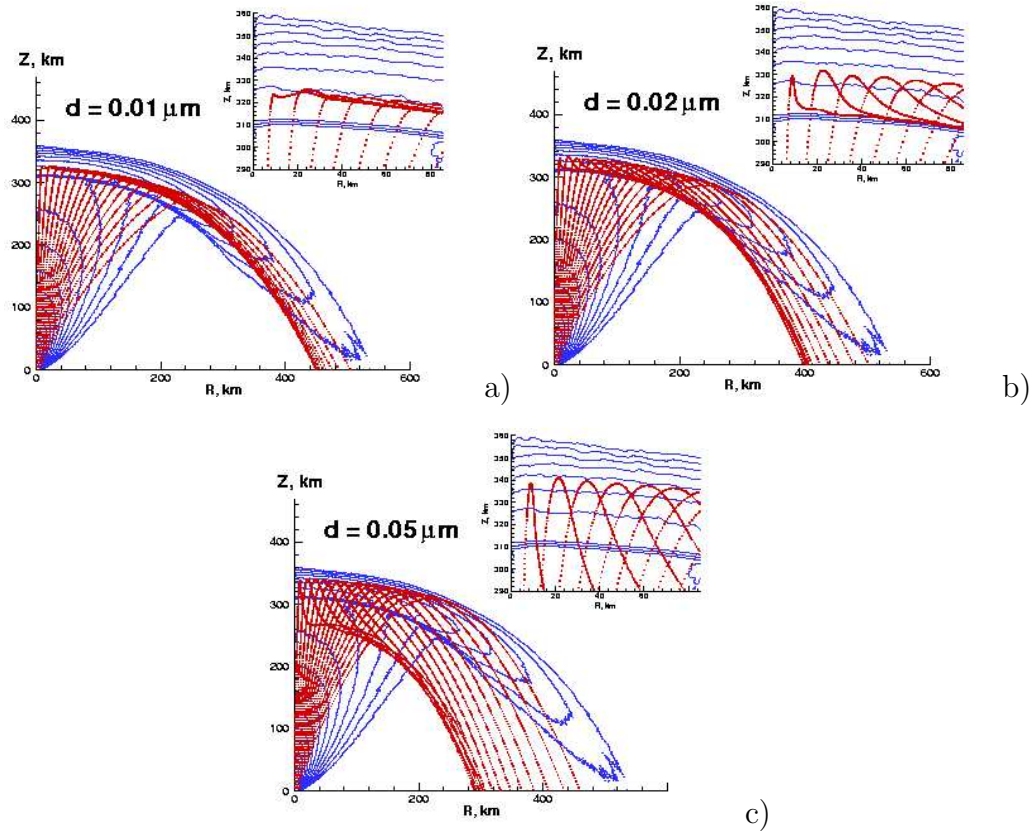
Figure 5.14: Trajectory (small dots) of different size particle (d = a) 0.01, b) 0.02 and c) 0.05 μm) with insets showing the vicinity of the canopy shock near the symmetry axis. Also shown are the same gas density contours as in Fig. 5.13.

122
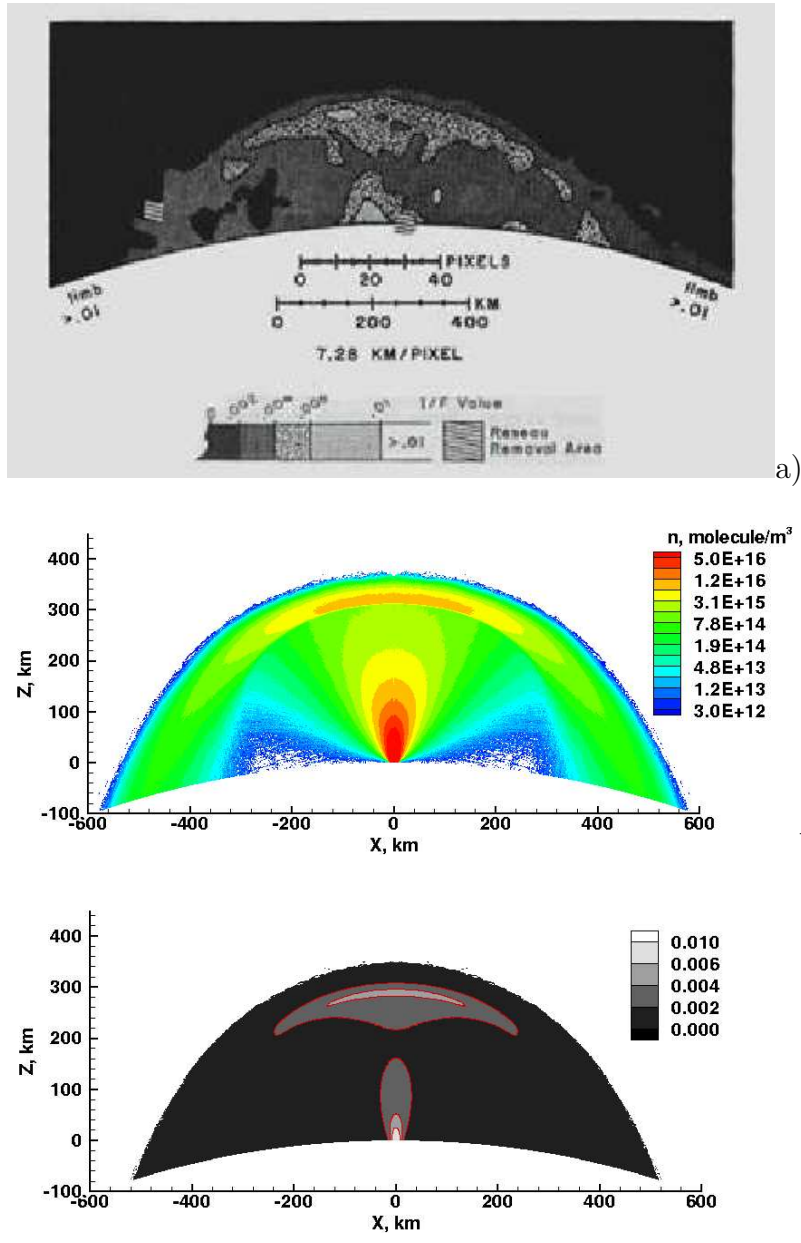
Figure 5.15: (a) Voyager image of the ultra-violet brightness of Pele, (*From Strom and Schneider (1982), courtesy of Robert Strom*) (b) the number density contours of the modeled Pele gas plume and (c) the gas TCD (normalized by $4.5 \times 10^{19} cm^{-2}$) for the modeled plume. The observed plume and the simulated plume are drawn to the same length scale. Note the calculated TCD below the limb is blanked.
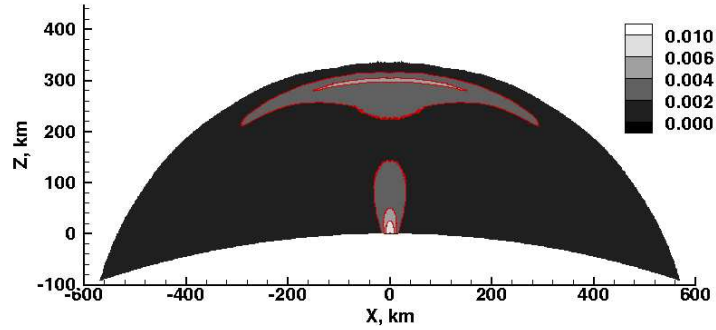
a) 1nm
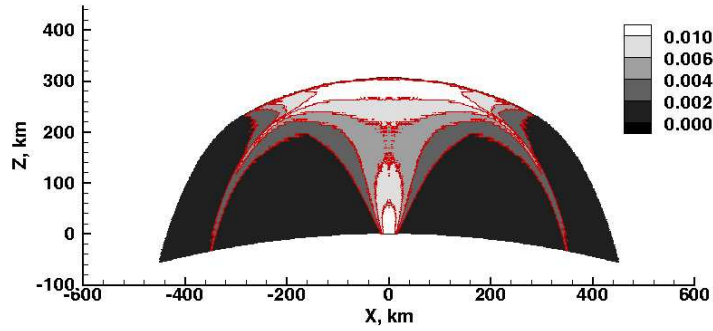
b) 10 nm
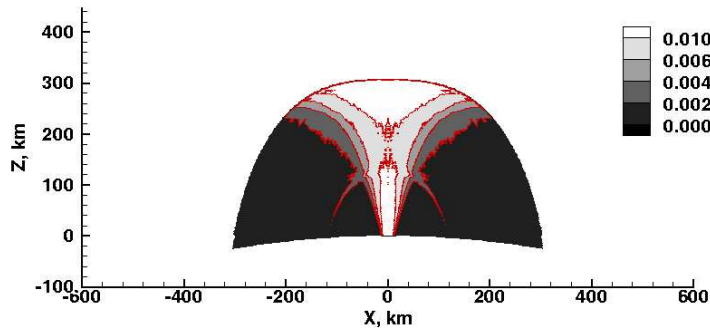
c) 100 nm

Figure 5.16: The normalized tangential column density (TCD) of (a) 1 nm, (b) 10 nm, (c) 100 nm refractory particles entrained in the plume shown in Fig. 5.15b except for plume a) where the gas plume was the early nominal Pele type plume with the flat surface and constant g approximations, and the plume was deformed into spherical geometry. The scales have been adjusted in each figure to enhance the details of the structures (the normalized TCDs at the vent are 0.015, 0.1 and 0.03 for a), b) and c), respectively). Notice the double-shock-like feature in b) and c).

As for the Prometheus simulations, it is found that the particles entrained in the Pele plume can be at most about 10 nm in size if they are to follow the gas flow. This is especially true in the outer portion of the plume. Figure 5.16a shows that the TCD contours for 1 nm particles are very similar to that of the gas (Fig 5.15c). Unlike the particle flow in Prometheus discussed in Section 5.3.1, particles as large as 100 nm in Pele can still reach and rise above the gas shock at ∼310 km altitude, so the particle size range in the outer portion (beyond the gas shock) of Pele may be wider than that of Prometheus.[5] This wider particle size range is consistent with the particle size estimates of less than 0.08 μm in Pele by Spencer *et al.* (1997), instead of 0.01 μm in Loki suggested by Collins (1981). However, as seen in Figs 5.16a-c, only particles of sizes on the order of 1 nm reproduce the observed contour shape well, especially near the canopy shock. According to Equation 5.2, 1 nm particles are far less effective in scattering sunlight than 10 - 100 nm particles. Therefore, the flow there must be dominated by ∼1 nm particles. In order to produce an I/F value of 0.004 at 0.35 μm wavelength, the column density of 1 nm particle needs to be ∼ 1×10^{19} cm^{-2} based on Equation 5.2 assuming the value of n_p = 1.9 of Spencer *et al.* (1997). This particle column density is two orders of magnitude higher than the gas column density. This is apparently quite unrealistic. However, due to the r^6 dependence of the light scattering efficiency, far fewer particles that are only slightly larger are needed to produce the observed

---

[5]However, the large particles cannot track the gas flow in the outer portion of Pele and they show a different signature (double-shock-like) near the gas shock as seen in Fig. 5.16c. The cause of these features has been illustrated in Fig. 5.14

I/F value, and these particles still track the gas flow quite well. For example, three orders of magnitude lower particle column density is needed for 3 nm particles, and 1.6 $\times 10^4$ times lower column density is needed for 5 nm particles in order to produce the observed I/F value. It is also understood that large particles could reach high altitude if they are created by condensation in the plume. In fact, large fluffy snow-flake-like particles track the gas flow much better than do spherical particles. This better response to the gas for snow-flake-like particles is observed in our simulations.

It must again be pointed out that the discussion above does not exclude the existence of larger micron-size particles, especially in the vent vicinity. In fact, the brightness in the vent vicinity of Pele observed by Voyager is very likely due to large particles of various sizes. The cone shape contours in the vent vicinity in the Voyager image of Pele are different from the "finger" shape contours shown in Fig. 5.16. This cone shape might be the signature of large-particle flow. Fig. 5.17a shows an example TCD computed for a particle cloud with a log-normal size distribution, and with the r^6 dependence of particle scattering efficiency indicated in Eqn. 5.2. The contour shape is quite similar to that in the vent vicinity in the Voyager image of Pele (*cf* Fig. 5.15a). A better match to the Voyager image can also be obtained by overlaying Fig. 5.17a on Fig. 5.16a to fake an image representing the injection of two classes of particles at the vent. Tiny ~1 nm grains or droplets perhaps forming from a condensate and larger 5 – 10 μm dust having a log-normal size distribution. Note that a size distribution seems to be necessary since we observed in our simulations

126
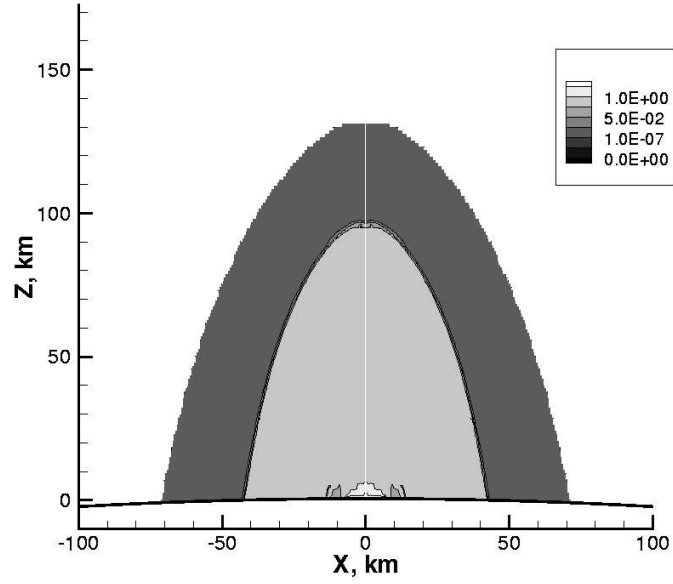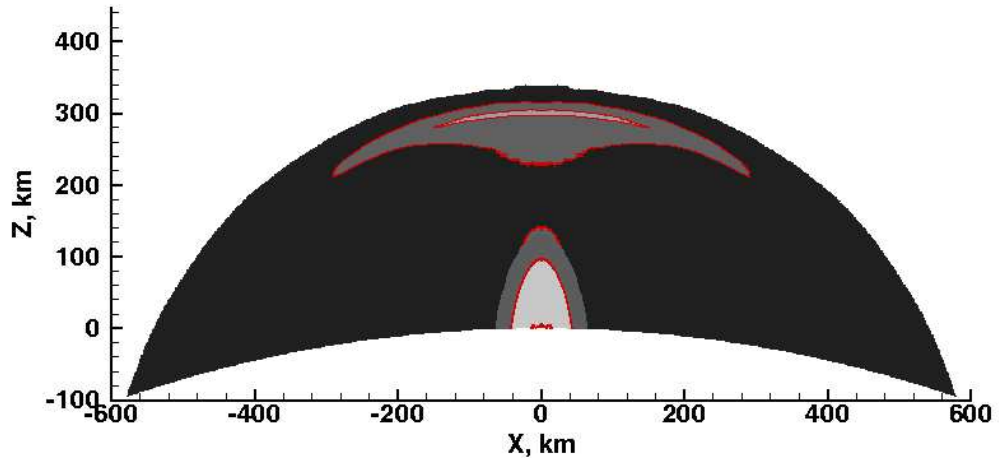
Figure 5.17: a) TCD contours of particles with size ranging from $5 - 10$ μm with a resolution of 0.25 μm. The particle size distribution is log-normal with $n_{5\mu m}/n_{10\mu m} = 100$. The gas plume is a nominal Pele plume shown Fig. 5.15b. b) A better match to the Voyager image is obtained by faked overlaying figure a) on Fig. 5.16a without the consideration of the population relation between 1 nm particles and the large micron-size particles.

127

that a plume of particles of a single size cannot reproduce the contour shapes unless some are condensates and others not.

5.4 Reproducing Plume Shadows Observed by Galileo

A remarkable reddish shadow cast by Prometheus is seen in the Galileo image shown in Fig. 5.18a. Several features appear in the image of the shadow: two components seem to be present with one corresponding to a dark "finger" and another to a "mushroom"; there is an asymmetry about the "finger" from north to south with the northern part of the shadow a little weaker and appearing to have a gradient in color while the southern part is relatively uniformly dark. An effort was made to reproduce these features by computing the shadows of particle plumes containing particles having different sizes. The solar zenith angle at the Prometheus vent in Fig. 5.18a was $\sim76.4^o$ when the image was taken. The column densities projected from the sun onto Io's surface at this angle were calculated for the particle plumes shown in Figs. 5.8 and plotted in Figs. 5.18b and c. The "finger" shape discussed above is found to be best reproduced by a plume of ~30 nm particles. The uniformly dark southern "mushroom" shape may be reproduced by ~80 nm particles. It should be pointed out that it is also possible that there are two distinct dust jets and a non-axisymmetric vent flow.

Similar calculations were conducted for the Pele gas plume, and the results are shown in Fig. 5.19. Perhaps someday a Pele shadow may be observed. Because of the large size of the Pele plume, only the lower part of the

128
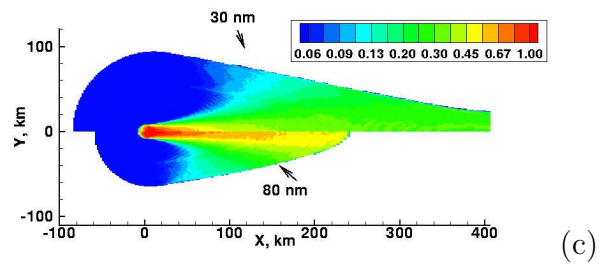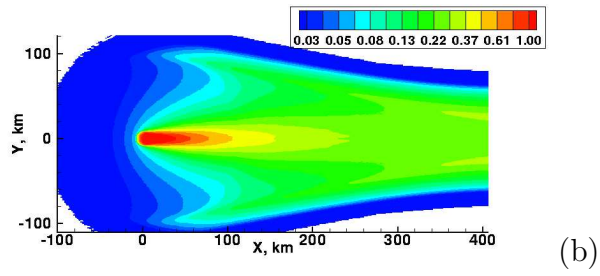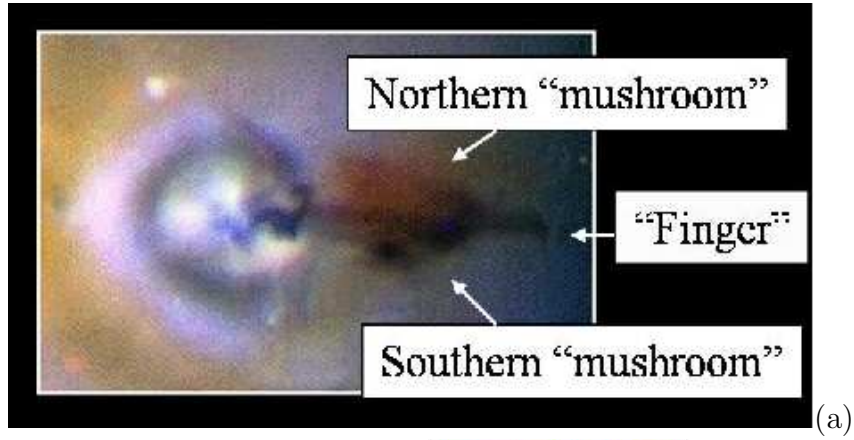
Figure 5.18: a) Galileo image of close-up views of Prometheus; b) Computed shadow cast on the surface by 1 nm particles; Shadow of 30 nm (top part of c) and 80 nm particles (bottom part of c). The simulated shadows and the inset of Prometheus in Galileo image are drawn to the same length scale.

129

plume casts a shadow on the surface at high solar zenith angles ($> \sim 50^o$).

5.5 Gas and Particle Deposition Patterns for Pele and Prometheus-type Plumes

5.5.1 Gas Deposition Patterns

Our previous results showed that the deposition pattern of the Pele plume varies as the temperature of the surrounding frost-covered surface changes during the Ionian day (*cf* Fig. 4.2). At low surface temperatures, the falling gas simply pours onto the surface and condensation dominates to build up a deposition peak. As the surface temperature increases and the sublimation atmosphere thickens, the SO_2 frost begins to be eroded away below the turning point of the impinging flow. We have made similar calculations for Prometheus and the results are shown in Fig. 5.20. Note that the simulated plumes used here are the ones with vent condition identical to that of the plume shown in Fig. 5.6b. The effect of erosion by the plume during the day when surface temperatures are high is seen for Prometheus as it was for Pele. Because the deposition profile also varies with time, one needs to calculate the time-averaged deposition profile to make a meaningful comparison with the observed multiple ring structure (Geissler *et al.* 2003) and examine the possibility of forming multiple rings by gas deposition. To do so, the deposition profiles for several different surface temperatures were weighted by the duration of time during the day the surface experienced that temperature and averaged over an Ionian day. The surface temperature as a function of time of
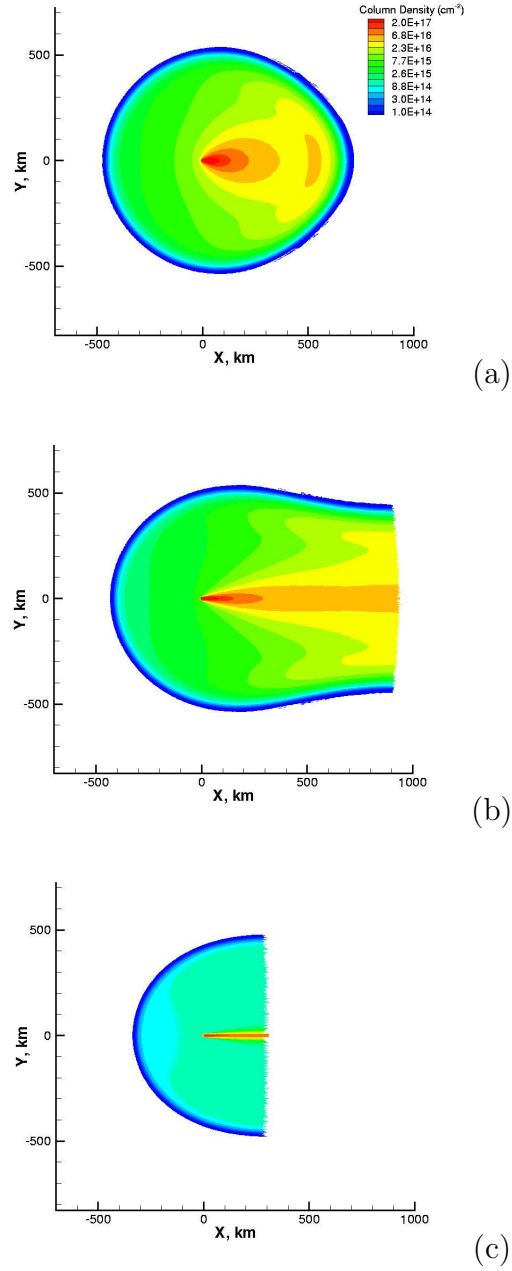
Figure 5.19: Shadow of gas or very small particles in Pele plume cast at three different solar zenith angles: a) 40°, b) 60° and c) 80°. The contour levels are arbitrary and are only chosen to illustrate the general shape of different shadow patterns. The origin is located at Pele's vent.

131
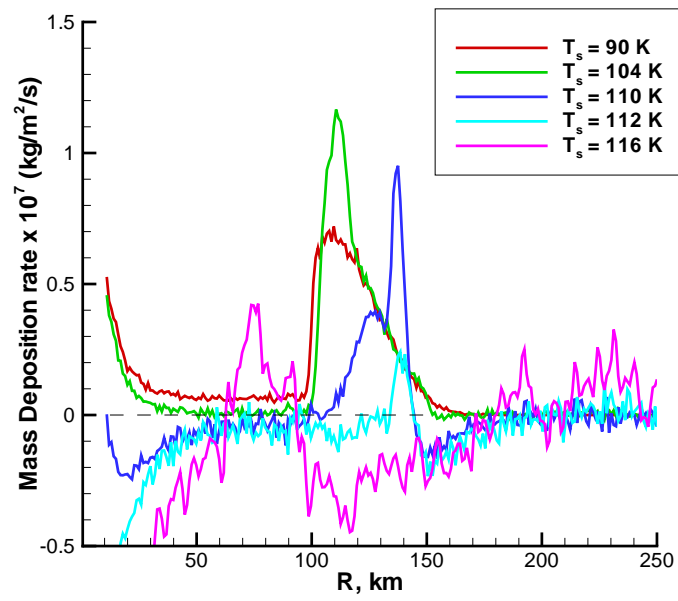
Figure 5.20: Deposition profiles around the Prometheus plume as a function of distance from the vent at different surface temperatures. Note that the profiles are blanked near the vent for R < 10 km.

Ionian day is based on the work of Kerton *et al.* (1996) as shown in Fig. 5.21. Since Prometheus is a small plume having little variation in latitude, the deposition around it is assumed to be symmetric around the vent. Figure 5.22 shows the diurnally-averaged deposition profile. It is seen that the diurnally averaged deposition profile in Fig. 5.22 has approximately the same peak deposition radius ($\sim$110 km) as the nightside plume (red curve in Fig. 5.20). Hence, the use of the nightside deposition profile to represent the peak deposition radius in the parametric study of vent conditions in Section 3.5 is justified. It is seen in Fig. 5.22 that there is a strong ring at $R = 100 - 150$ km and indications of a couple of possible other rings at radii inside and outside R of 150 km.

Another interesting feature of the deposition ring is its sharp inner edge when the surface temperature is low. This is a reflection of the extension of the canopy shock all the way to the surface. The abrupt change in the gas density across the shock near the intersection of the shock and the surface causes the jump in the flux to the surface.

5.5.2   Particle Deposition Patterns

We have shown that there is a sorting mechanism for particles inside the gas plume: the motion of large particles tends to decouple from that of the gas, and thus large particles rise lower and land closer to the vent than do smaller ones (*cf* Fig. 5.13). This sorting mechanism also exists in Prometheus. Figures 5.23a–b illustrate the normalized deposition profiles of relatively large

133
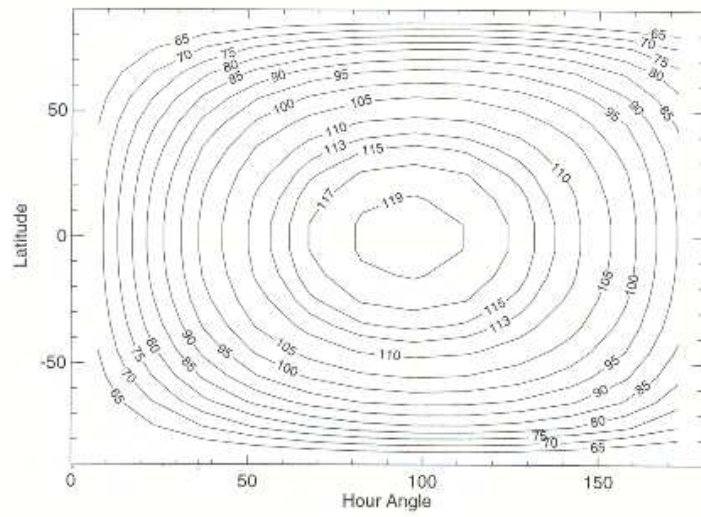
Figure 5.21: Surface temperature profile used in the calculation of time averaged deposition. Note that the minimum surface temperature has been set to 90 K at which no appreciable sublimation atmosphere is present.
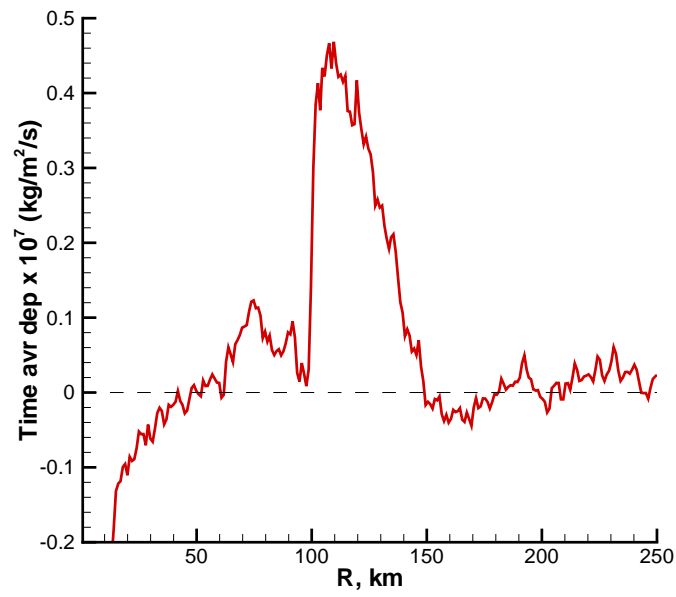
Figure 5.22: Diurnally averaged gas deposition profiles with peak subsolar temperature T_{ss} of 116 K for Prometheus.

refractory particles. Note the distinct edges of the particle rings compared to the gas condensation ring. The figures suggest that particles of different sizes deposit at different distances from the vent. Double peaks even appear in the deposition profile of particles of a single size. This is due to the deposition of particles falling from near the gas shock and from below the shock (analogous to the particle trajectory in Pele shown in Fig. 5.14). Moreover, unlike the deposition of the gas frost and nano-size particles, the deposition profiles of larger particles (> 10 nm) are very weak functions of the surface temperature. Figures 5.23a and b compare the deposition of particles in a nightside and a dayside Prometheus plume. The precipitation of these particles near the turning region of the gas flow over a warmer surface results in this insensitivity.

The deposition profiles of nano-particles in the plumes with relatively high surface temperatures are shown on a log scale in Fig. 5.23c. Outer rings are indeed seen in these profiles. Thus, we suggest that the outer rings (at $R > 110$ km) around Prometheus discussed by Geissler *et al.* (2003) are likely caused by the deposition of small nano-size particles that followed the gas through its "bounce" (Fig. 5.7a) below the re-entry shock. Bigger particles would not be carried through the "bounce" by the low density gas flow (Fig. 3.13).

The deposition profiles of different size particles in a nightside Pele plume are plotted in Fig. 5.24. An interesting feature is that the particles tend to deposit in distinct bands with a sharp rise in deposition at the band inner edge. These particle bands occur at different locations than the gas deposition ring.
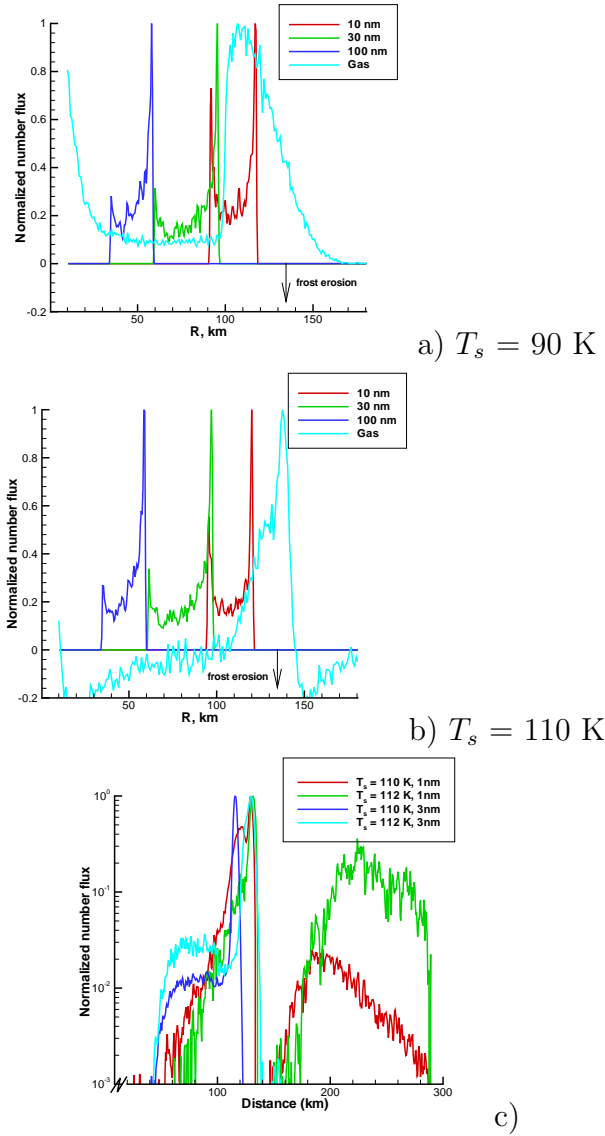
Figure 5.23: Deposition profiles (normalized by peak rate) of different size refractory particles entrained in (a) a night side ($T_s = 90$ K) Prometheus plume and (b) a day side ($T_s = 110$ K) plume, and also deposition of the gas. (c) Deposition profiles of small particles in plumes with relatively high surface temperatures plotted on a log scale to illustrate the small net deposition at large radius from the vent. Note the possible explanation of the outer deposition ring by this profile.

137
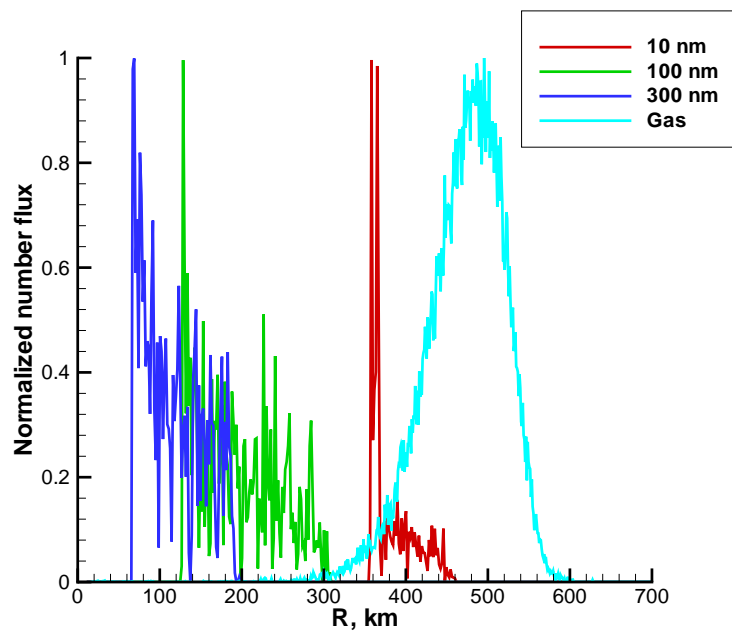
Figure 5.24: Normalized (by peak rate) deposition profiles of refractory particles of different sizes entrained in a night side Pele plume. Also shown is the gas deposition profile for comparison.

5.6 Transport of S_2 Gas and Na inside Pele-type Plume

5.6.1 Transport of S_2 Gas inside Pele-type Plume

Spencer *et al.* (2000) found that the Pele plume may contain as much as 30% S_2 by molar fraction. The effects of mixing S_2 gas inside a Pele type plume on the plume dynamics are investigated below. Due to the lack of some required data for S_2 gas that are necessary for the DSMC simulation, an artificial model of atom-like S_2 molecules was first used. Although the more realistic model for S_2 molecules that will also be discussed shortly makes the discussion of the results associated with the "atom" model appear to be redundant, the unexpected phenomena in these results are worth mentioning and may applied to similar situations in the future. In this artificial model, the S_2 molecules are assumed to be atom-like particles of mass = 64 amu having no rotational or vibrational energy. Flows with different S_2/SO_2 mixing ratios were examined. We had expected that because the S_2 was assumed to be atom-like with no internal energy other than translational energy, the more S_2 in the flow, the lower the plume would rise and the less it would expand. However, Figs. 5.25a–c show that the bulk flow is essentially insensitive to the S_2/SO_2 mixing ratio ($< 50\%$) at the vent. This is rather unexpected, and the reason for it is worth investigating and discussing.

The main "channels" through which the internal energy of gases can be lost or converted are intermolecular collisions and radiation from the rotational lines or vibrational bands. While the plume expands, the internal energy of the gases is converted to kinetic energy through intermolecular collisions. The less

the internal energy of the gas, the less the plume should expand and accelerate. However, when one of the major species, in our case SO_2, has a "wide" channel to lose internal energy, $i.e.$ the fast emission from the vibrational bands. The excess rotational and vibrational energy of SO_2 at low S_2/SO_2 mixing ratio is lost through the emission from the vibrational bands of SO_2 before it can be converted to kinetic energy and contribute fully to the expansion of the plume. The VT collision relaxation time is $\sim$1 s for the ν_2 vibration mode, and $\sim$5 s for the other two modes. However, the radiative life times for the ν_1, ν_2, and ν_3 vibrational bands are $\sim$0.3, 1, and 0.02 s, respectively. Thus, intermolecular collisions work as a pump, pumping the internal energy (both translational and rotational energy) into vibration modes from which it is lost through emission, and the flow becomes virtually independent of the amount of rotational and vibrational energy the gases have at the vent. To verify this explanation, another artificial model is used in which the vibrational energy modes of SO_2 are turned off (corresponding to infinite VT collision relaxation time) so that the channel of radiative emission and energy loss from the vibrational bands is shut down. It is expected that the flow will thus become sensitive to the S_2/SO_2 mixing ratio since the internal energy (rotational and translational energy only in this case) can only be converted into kinetic energy[6]. The difference in the amount of internal energy the gases have at the vent at different S_2/SO_2 mixing ratio will thus affect the shape of the plumes. This is actually confirmed by Fig. 5.26 in which differences are seen in the three cases shown although the

---

[6]The radiation from rotational lines is slow.

differences are small. Note the slightly higher shock in the plume shown in Fig. 5.26a than in c. The lower the S_2/SO_2 mixing ratio, the higher the internal energy the gases have at the vent and, thus, the higher the plume rises and the more widely it expands. This is the trend one would expect when mixing atom-like particles with molecules. However, as noted above, this effect is not observed when radiative losses from the major molecular species in the gas are dominant.

A more realistic S_2 model is incorporated next. The rotational and discrete vibrational energies of S_2 are incorporated, and since S_2 does not have a electric dipole moment, it does not radiate from rotational energy modes. It does not emit from the single vibrational band of S_2 (centered at 725 cm^{-1}) either since it is a homonuclear diatomic molecule. The relaxation collision number is assumed at the moment to be the same as ν_2 band of SO_2. It should be pointed out that a detailed model for S_2 actually appears to be quite unnecessary since, as already discussed, the gas dynamics is so dominated by the emission from the vibrational bands of the major species - SO_2. Figures 5.27a-c show that the results with the more realistic model of S_2. The plume heights and width are virtually insensitive to the S_2/SO_2 mixing ratios just as those shown in Figs. 5.25a-c, and the detailed S_2 model does not create appreciable new features in the flow.

The transport of S_2 gas in the plume is examined next. The S_2 gas is seen to closely follow the bulk SO_2 gas flow (Fig. 5.28), and the S_2/SO_2 mixing ratio stays approximately constant throughout the entire plume (Fig. 5.29).
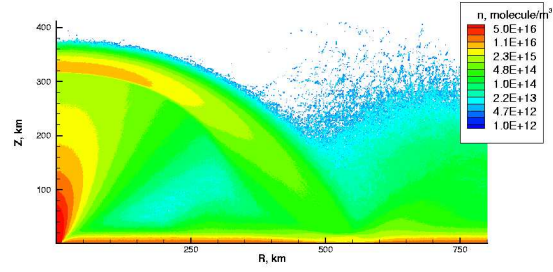
a)
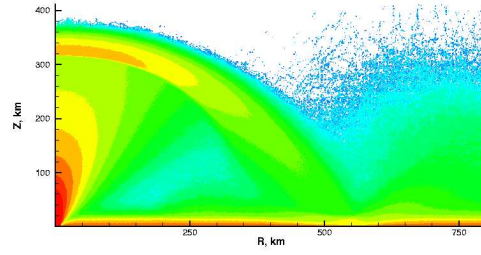
b)
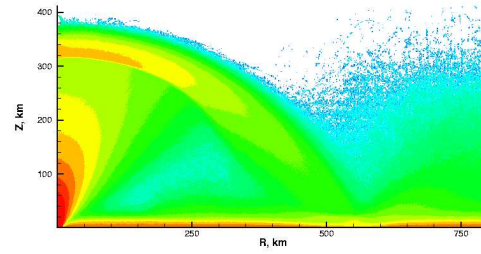
c)

Figure 5.25: Total number density contours of simulated Pele type plumes with a) no, b) 20%, and c) 40% of atom-like S_2 gas mixed with SO_2 at the vent. The surface temperature is a nominal 111 K.
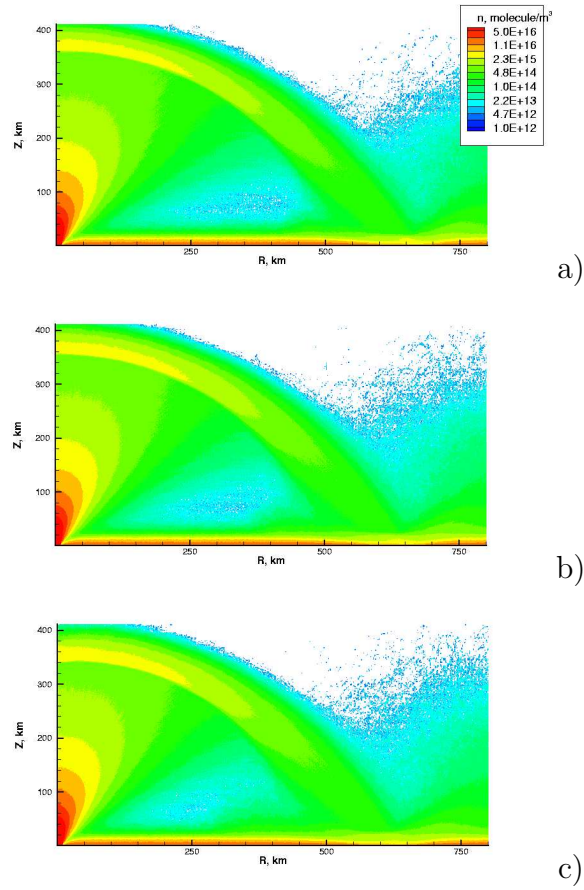
Figure 5.26: Total number density contours of simulated Pele type plumes with a) no, b) 20%, and c) 40% of S_2 gas mixed with SO_2 at the vent. Note the vibrational energy of SO_2 is turned off. The surface temperature is a nominal 111 K.
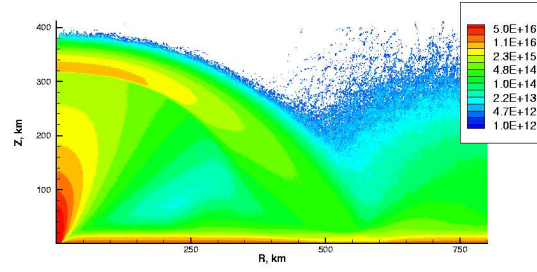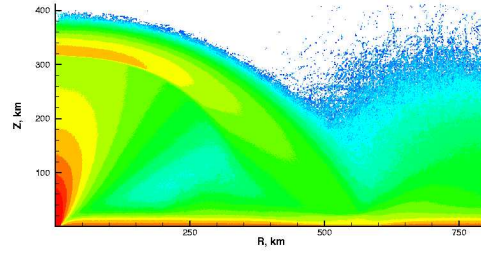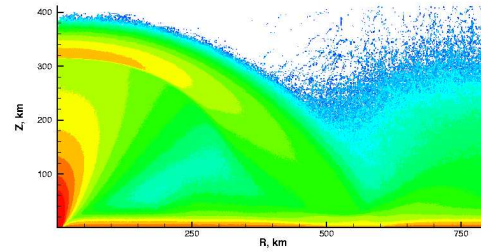
Figure 5.27: Total number density contours of simulated Pele type plumes with a) no, b) 20%, and c) 40% of S_2 gas mixed with SO_2 at the vent. The surface temperature is a nominal 111 K.

However, S_2 does not sublime from the surface at 111K and is not present in the SO_2 sublimation atmosphere at low altitude. Falling S_2 does penetrate to low altitude near the re-entry shock along with the falling SO_2 gas and also follows the SO_2 through the bounce. The deposition profiles for SO_2 and S_2 gases are plotted in Figs. 5.30a and b, respectively. It is seen that although S_2 gas closely follows the bulk SO_2 gas flow and bounces with it as it falls, the deposition profiles of these two gases are quite different. Since S_2 does not sublime appreciably from the surface at even the dayside surface temperature on Io, it cannot be depleted by the bouncing flow as is SO_2 frost. S_2 simply deposits onto the surface even in a dayside plume even though the deposition rate is low due to the bouncing with SO_2. As discussed in Section 4.6, the bouncing plume gas becomes very diffused and simply flows on the top of the sublimation atmosphere. The bouncing plume gas cannot penetrate the sublimation atmosphere to cause significant deposition. This is even more so for the S_2 deposition as seen in Fig. 5.31 which shows the deposition of S_2 from a plume having 20% S_2 like that shown in Fig. 4.19. This explains why there are no apparent multiple reddish rings around Pele. One may note that there is still appreciable SO_2 deposition after first bounce as seen in Fig. 4.20. This is not true for S_2 even though it tracks SO_2. This can be explained by distinguishing the deposition caused purely by the plume gas that originates from the vent source and by the gas scoured from the surface near the first bounce. The red profile in Fig. 5.31 shows the deposition of SO_2 purely due to the plume gas and it can be seen that the deposition of
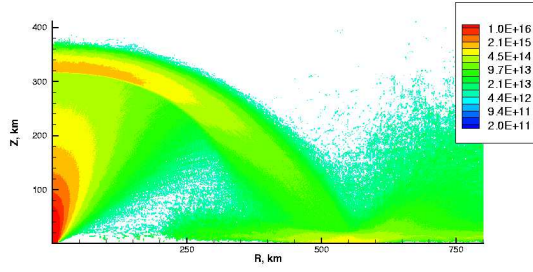
Figure 5.28: S_2 number density contours for the plume shown in Fig. 5.27b
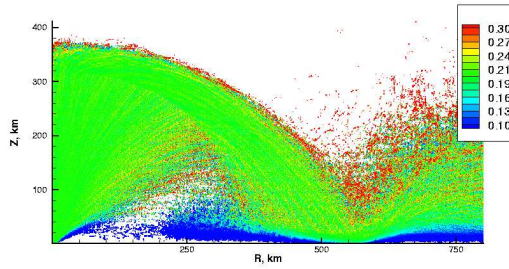
Figure 5.29: S_2 concentration contours for the plume shown in Fig. 5.27b.

plume SO_2, like S_2, is also virtually zero after the first bounce. This also confirms the suggestion above that the plume gas becomes very diffuse and cannot penetrate the sublimation atmosphere to cause significant deposition.

5.6.2 Transport of Na inside Pele-type Plume

The existence of a sodium cloud surrounding Io is another spectacular phenomenon associated with the planet. The ultimate source of Na is thought to be NaCl, and an atmospheric source of NaCl other than sublimation of frost must be considered (Lellouch *et al.* 2003). Active volcanoes have been

146
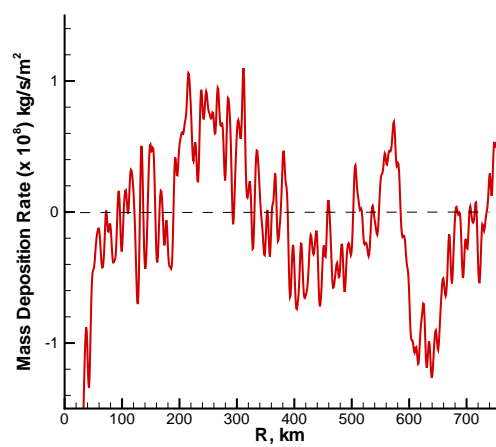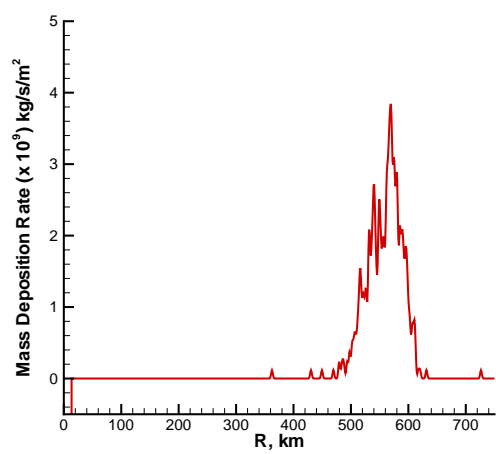
Figure 5.30: a) SO$_2$ and b) S$_2$ deposition profiles for the plume shown in Fig. 5.27c

147
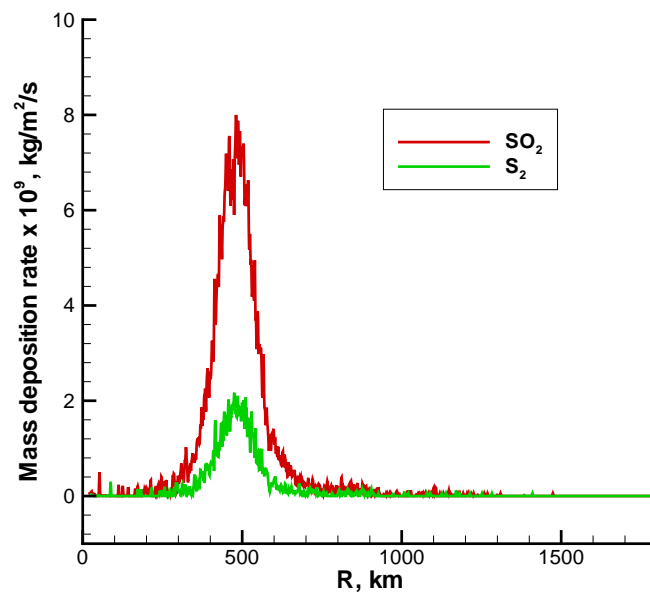
Figure 5.31: The deposition purely due to the plume gas (from the vent) for the simulated Pele type plume like that shown in Fig. 4.19. That is, the red SO_2 curve represents the deposition profile only of the SO_2 molecules which came from the vent, not those sublimated off the surface.

suggested as important sources of Na and Cl (Moses *et al.* 2002a, Lellouch *et al.* 2003). In an attempt to reproduce the atomic sodium number density profiles observed at high altitude by Schneider *et al.* (1991a), Moses *et al.* (2002a) found that if realistic sodium number densities at the vent is used, the sodium densities calculated seem to be too high at high altitude as seen in Fig. 5.32. In their model, plume dynamics are ignored so that there is no shock at high altitude as in our results. If one accounts for the rapid slowing of the upward moving SO_2 and entrained sodium through the canopy shock, the observed low sodium number density at high altitude may well be reproduced. The transport of Na in plumes is thus examined in some detail below. The VHS molecular diameter of Na is not provided by Bird (1994). The VHS molecular diameter of Ne is used instead.[7] Figures 5.33a and b show that although Na is light and tends to have larger thermal velocities than SO_2, it closely follows the bulk SO_2 gas flow, and the Na/SO_2 mixing ratio of 5:95 stays approximately constant throughout the entire plume. It has been assumed that Na does not sublime from the surface at 111K. It is therefore seen that Na is not present in the SO_2 sublimation atmosphere at low altitude. The Na rising from the volcanic vent is indeed blocked by the canopy shock and the Na number density is low above the canopy shock at high altitude. Further investigation, *e.g.* of the effect of plasma bombardment of the top of the plume, is needed to finally match the Na density profile at altitudes greater than ∼600 km in Schneider

---

[7]Note that Ne is a noble gas and may have a smaller collision diameter than Na. However, the conclusion drawn in this section is rather insensitive to the collision diameter.
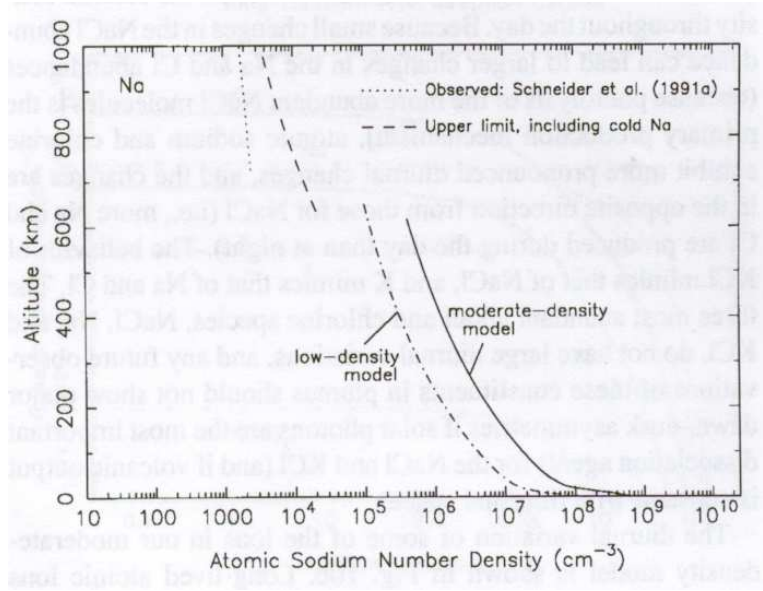
Figure 5.32: Na number density profiles. Adapted from Moses *et al.*, 2002.

et al. (1991a). Preliminary results do show inflation of the top of the plume by plasma bombardment as illustrated by Figs. 5.34a and b.

5.7   Results associated with Partially Opaque Gas Model

Under some circumstances, the plume opacity could be important. For example, the number density at the vent exit increases as $1/r_v^2$ as we reduce the vent radius r_v, if the vent rate (1.1×10^4 kg/s) and velocity (1000 m/s) are kept constant to match certain observations such as resurfacing rates and the resulting average column density. As a result of the density increase, the opacity of the gas in the vent vicinity may become important. Therefore, the effects of plume opacity at the three SO_2 vibrational band centers have been
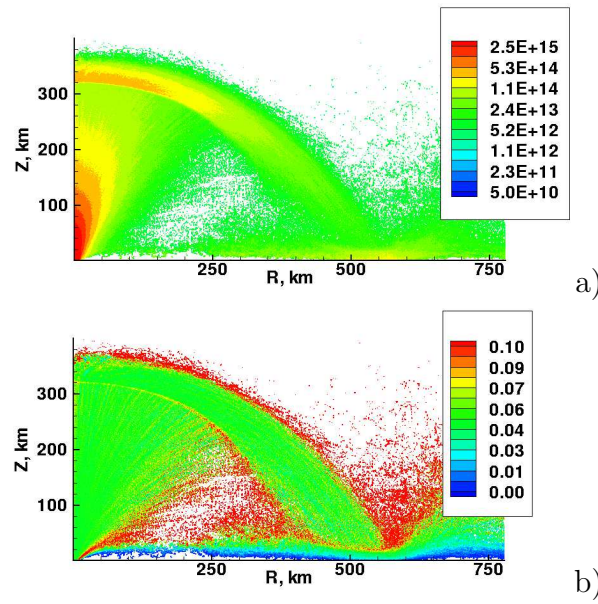
Figure 5.33: a) Na number density contours and b) concentration of Na inside a simulated Pele type plume with 5% of Na mixed with SO_2 at the vent. The surface temperature is a nominal 111 K.

a)

b)
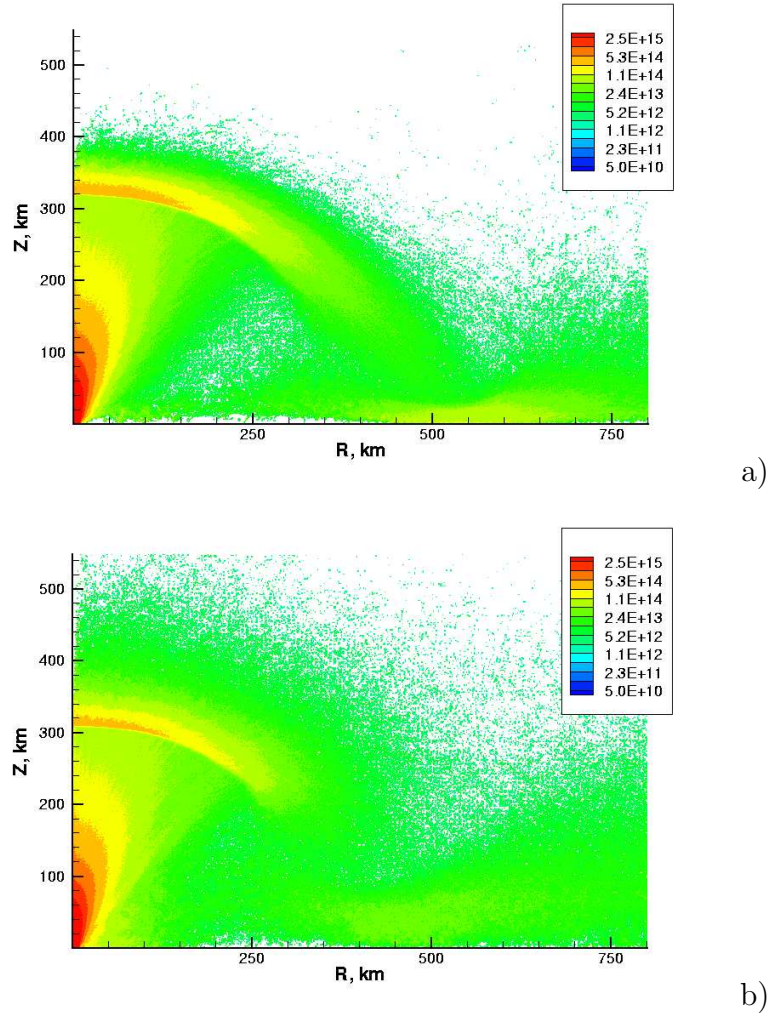
Figure 5.34: Na number density contours inside a simulated Pele type plume with plasma energy flux of a) 1.3 erg/m^2/s and b) 26 erg/m^2/s. In both cases, 5% of Na is mixed with SO_2 at the vent. The surface temperature is a nominal 111 K.

examined. The line intensities, σ, from HITRAN are here assumed constant in this part of the model for low gas temperature, and 5×10^{-22} cm^{-1}/(molecule cm^{-2}), 5×10^{-22} cm^{-1}/(molecule cm^{-2}), 4×10^{-20} cm^{-1}/(molecule cm^{-2}) are chosen as the typical intensity for the ν_1, ν_2 and ν_3 bands, respectively. The absorption coefficients, α, are then calculated as $\sigma \phi n$, where ϕ, the line shape function, is evaluated at 1151 cm^{-1}, 518 cm^{-1} and 1361 cm^{-1} for the ν_1, ν_2 and ν_3 bands, respectively, in each computational cell.

Consider the ν_3 band for example. Fig. 5.35 shows the effect of vent size on the absorption coefficient α. It is seen that the absorption coefficient at the vent increases by almost two orders of magnitude when the vent radius is decreased from 8 km to 1 km. Therefore, the effects of plume opacity at the three SO$_2$ vibrational band centers must be examined. Note that optically thin gas model was used to obtain the flow fields shown in Fig. 5.35.

The choice of the threshold for α is based on the radius of the vent. A vent radius of 1 km is used in the following discussion in this section. A threshold of $\alpha = 1$ km^{-1} is set for the calculation of vibrational band radiation. That is, if $\alpha > 1$ km^{-1} for a vibrational band in a cell, the gas in that cell is assumed to be opaque and does not radiate from that vibrational band (immediate local re-absorption); otherwise, the gas is assumed to be optically thin and the spontaneous emission from that vibrational band escapes without being re-absorbed.

Fig. 5.36 shows the comparison of the SO$_2$ number density contours for an optically thin gas model and the model in which opacity is accounted

153
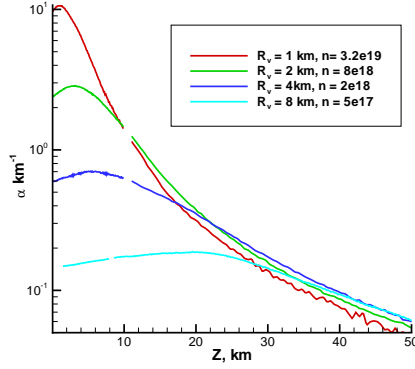
Figure 5.35: Absorption coefficient profiles of ν_3 band along the vertical symmetry axis. $\alpha < 1$ km^{-1} means transparent, $\alpha \geq 1$ km^{-1} means opaque. R$_v$ is the vent radius.

for approximately as discussed above. Because less energy is lost through vibrational radiation in the opaque region in the vent vicinity (shown in greater detail in Fig. 5.37), the partially opaque gas plume rises $\sim$10% higher and expands $\sim$10% more than the optically thin gas plume. In consequence the vent parameters need to be readjusted to fit the observed Pele plume shape and deposition pattern. New values of vent temperature of 500 K and velocity of 950 m/s are found to be suitable[8]. They are 23% and 5%, respectively, lower than the optically thin gas fits. The calculated plume emission power density contours of the three vibrational bands in the vent vicinity are shown in Fig. 5.37. It is seen that the opacity of the ν_3 band is the highest and, with the threshold of $\alpha = 1$ km^{-1}, almost no emission could escape from the

---

[8]Note the model used here is the early one which does not account for variable g, spherical geometry *etc.*

154
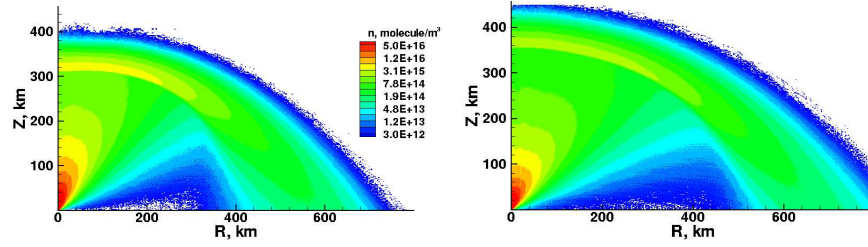
Figure 5.36: The comparison of the SO_2 number density contours for the optically thin gas model (left) and the partially opaque gas model (right). Vent conditions are the same. Notice the greater vertical and horizontal spreading of the partially opaque plume.

plume core. That is, the plume cools via ν_1 and ν_2 radiation and gas dynamic expansion while still opaque to ν_3: once it expands enough to be transparent to ν_3, the population of the excited ν_3 mode has become small due to the de-excitation through inter-molecular collisions and it is too cool to radiate much. The opacity of the ν_1 band is the lowest. The total (volume integrated) power from ν_3 is dramatically reduced to virtually zero due to the opacity. For the ν_2 band, the absorption coefficient of α transitions from > 1 km^{-1} to < 1 km^{-1} inside the plume core at the boundary between zero emission power and non-zero emission power.

It should be pointed out that the plume opacity is only important when the vent size is small ($< \sim 1$ km in radius). As will be shown later in Chapter 6, the concept of a "virtual" vent makes the ~ 8 km vent radius we have been using reasonable. The plume opacity is thus not important for our purposes and an optically thin gas assumption can be used. Therefore, most of the results discussed in the present work are from the optically thin gas model

155
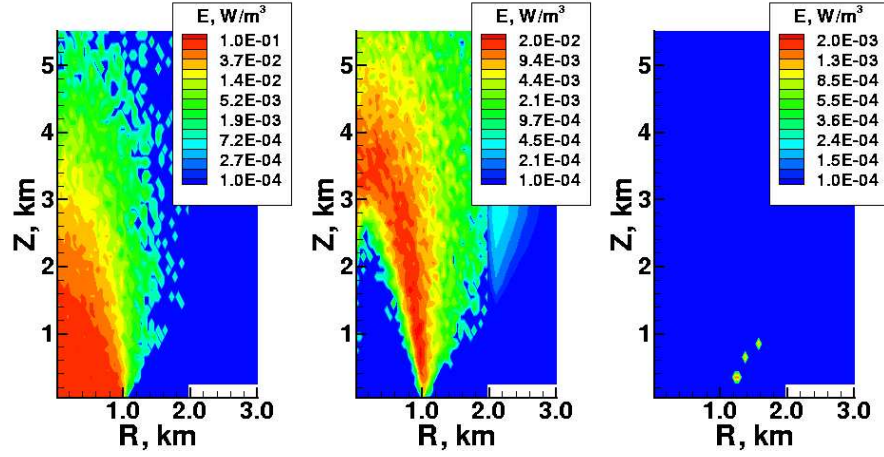
Figure 5.37: The emission power density contours of the three vibrational bands (for ν_1, ν_2 and ν_3 from left to right) in the vent vicinity. Note the logarithmic color bar.

unless explicitly indicated otherwise.

5.8   The Effects of Unsteadiness and Parabolic Velocity Profile of Volcanic Sources

5.8.1   The Effect of Unsteadiness of Volcanic Source

It is quite likely that the volcanic sources experience some kind of unsteadiness. Efforts are made to investigate the effects of unsteadiness of volcanic sources. The unsteadiness is simulated by pulsing the source velocity in a sinusoidal fashion with a particular period but keeping the number density and temperature at the vent constant. Note that other possibilities would, of course, have been possible. The amplitude of the velocity pulsing is set to be a nominal 30% of the mean vent velocity of 1000 m/s. A parametric study is

performed on the period of the pulsing source velocity for a Pele type plume. Since the flow time scale of Pele is ∼20 minutes, pulsing periods of ∼30 min. (close to the flow time scale), 10 min. and 1 min. (much shorter than the flow time scale) are tried.[9] Figures 5.38 and 5.39 show that when the pulsing period is comparable to the flow time, well defined and strong moving shocks are formed due to the strong impact between the rising and falling gas. For a shorter pulsing period (∼1 min.), a quasi-steady state can be reached and the canopy shock becomes virtually stationary as shown in Fig. 5.40. Wave patterns are also seen in the flow. The time evolutions of emission from the overall rotational lines and the ν_2 vibrational band of SO_2 are also illustrated in Figs 5.41 – 5.46. Enhanced rotational emission at the moving shocks is seen for the flow with 30 or 10 minutes pulsing period. Figure 5.47 shows that the volume integrated power for 30 min period case varies by a factor of two during the entire period of oscillation. The finding of enhanced emission at the moving shocks is also true for the three vibrational bands although they are not shown here. Note that only emission from the ν_2 band in the vent vicinity is shown here for illustration. The emission from the other two vibrational bands are qualitatively similar. It is interesting that for a stationary shock to be developed, it is necessary for the pulsing period T to be much shorter than the ballistic time t_0 (in this case 9.3 min) determined by the mean velocity at

---

[9]Note that only part of the plume close to the axis is simulated to increase the smoothness of the transient calculation and for the convenient presentation without losing plausibility. The flow out the circumferential boundary remains supersonic. Also, a constant g is used in these results.

157
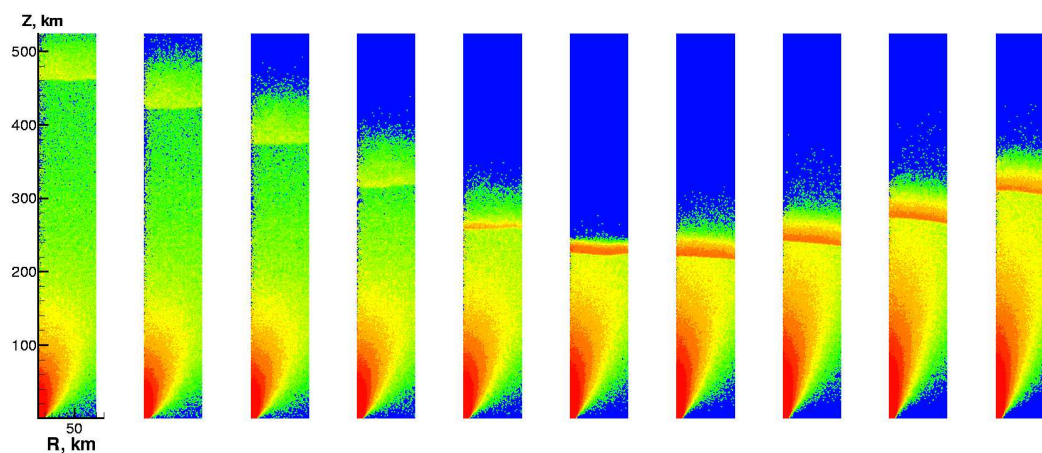
Figure 5.38: Time evolution of SO_2 number density contours of Pele type plume with an unsteady source. Time interval between each frame is 80 s. The source number density is kept constant but the source velocity has an oscillating period of $\sim$30 min. The oscillating amplitude is a nominal 30% of the mean vent velocity of 1000 m/s.

the vent.

5.8.2   The Effect of Transient Flow on the Observed Plume Shape

Not all of the volcanic plumes observed by Voyager have the symmetric, umbrella shape as do the Prometheus and Pele. Loki is one of the examples of the plumes that does not have an umbrella shape (Fig. 5.48) and has no obvious canopy shock. Kieffer (1982) has suggested a classification of two categories: balanced (Prometheus and Pele) and underexpanded (Loki) plume based on their shape. A vent gas pressure approximately equal to ambient pressure will result in a balanced plume which has symmetric umbrella shape,

158
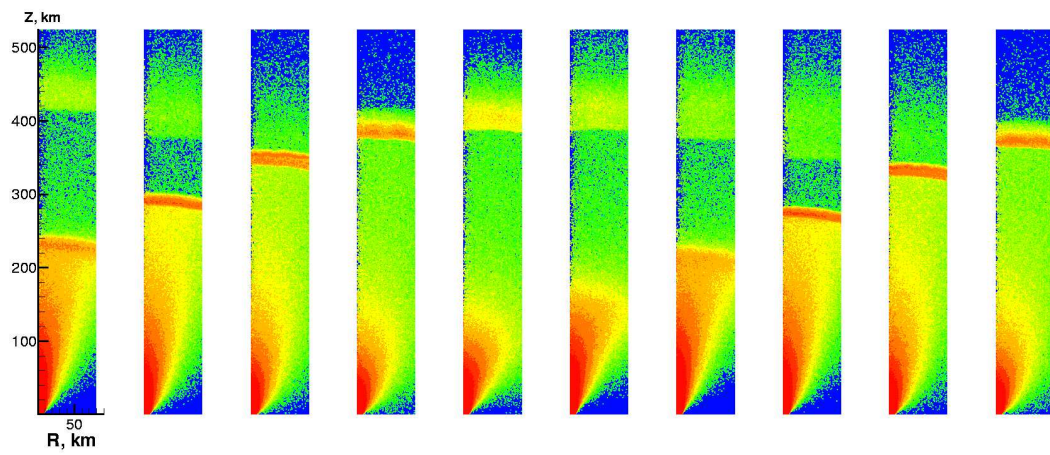
Figure 5.39: Time evolution of SO_2 number density contours of Pele type plume with an unsteady source. The conditions at the vent are the same as the case shown in Fig 5.38 except that the source velocity has an oscillating period of ~10 min.
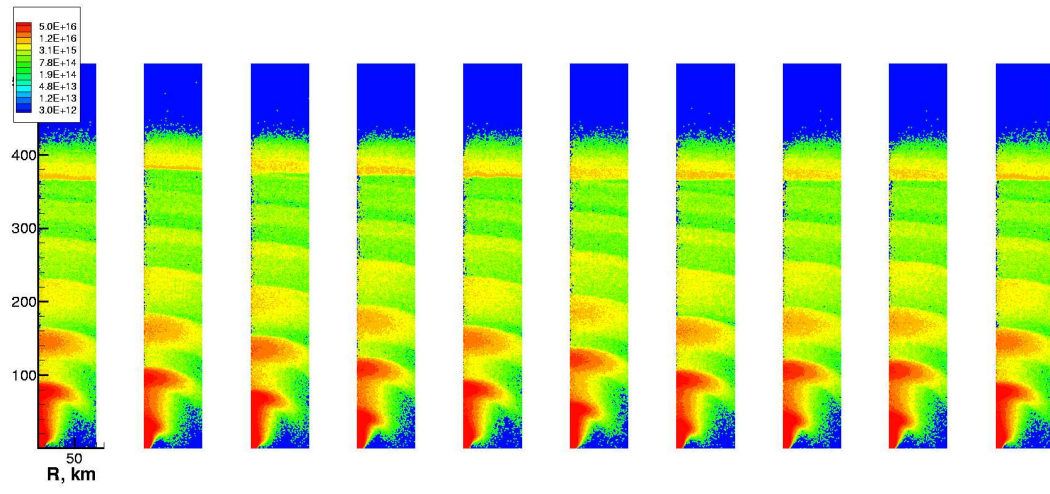
Figure 5.40: Time evolution of SO$_2$ number density contours of Pele type plume with a unsteady source. The conditions at the vent are the same as the case shown in Fig 5.38 except that the source velocity has an oscillating period of $\sim$1 min.
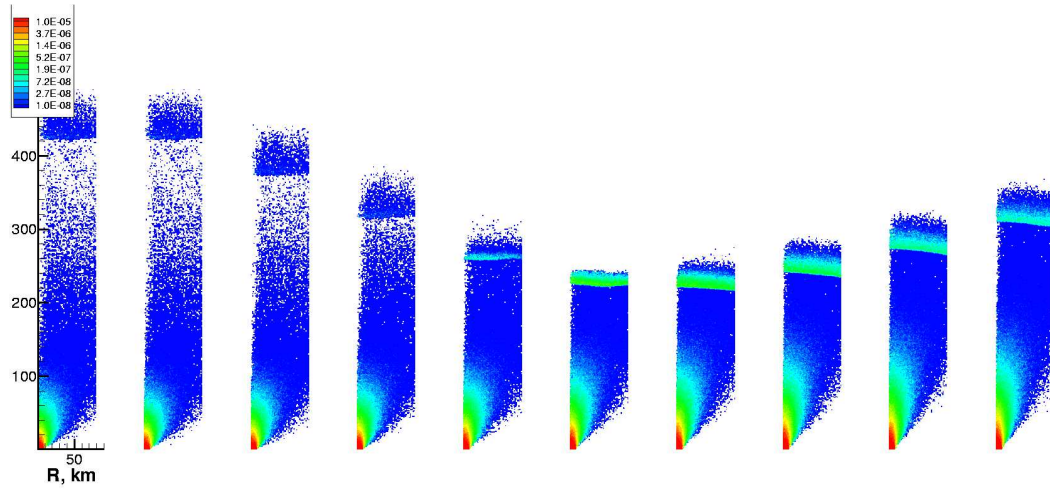
Figure 5.41: Time evolution of SO_2 overall rotational lines emission contours of Pele type plume with an unsteady source. Time interval between each frame is 80 s. The source number density is kept constant but the source velocity has an oscillating period of $\sim$30 min. The oscillating amplitude is a nominal 30% of the mean vent velocity of 1000 m/s.
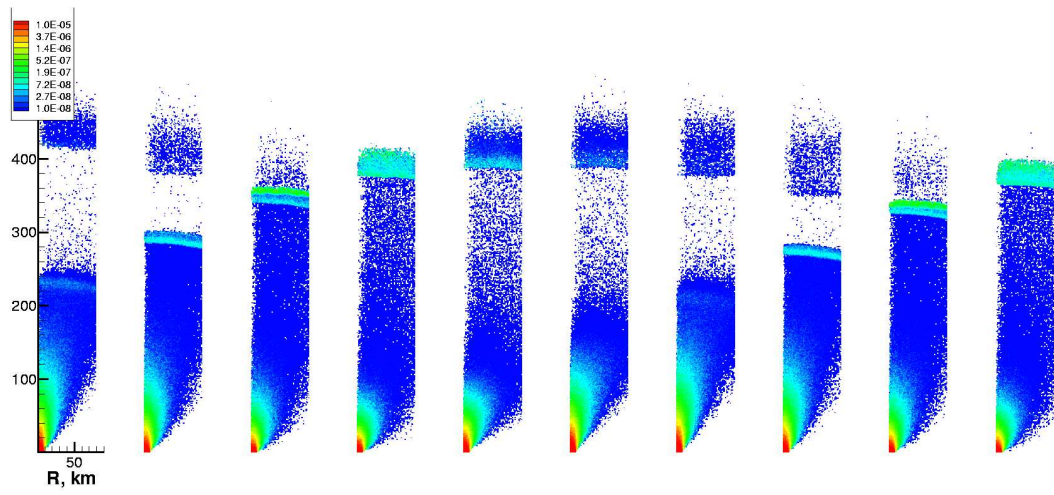
Figure 5.42: Time evolution of SO_2 overall rotational lines emission contours of Pele type plume with an unsteady source. The conditions at the vent are the same as the case shown in Fig 5.38 except that the source velocity has an oscillating period of $\sim$10 min.
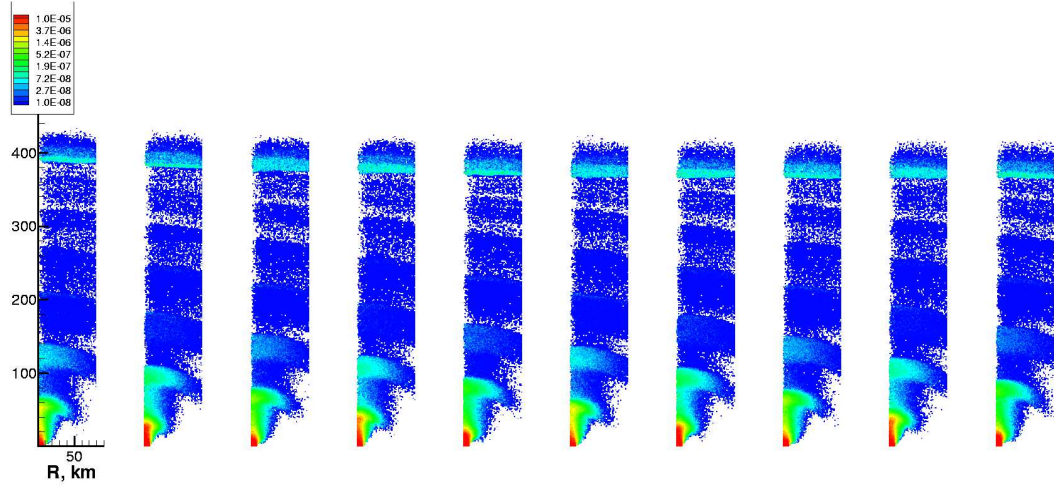
Figure 5.43: Time evolution of SO_2 overall rotational lines emission contours of Pele type plume with a unsteady source. The conditions at the vent are the same as the case shown in Fig 5.38 except that the source velocity has an oscillating period of $\sim$1 min.
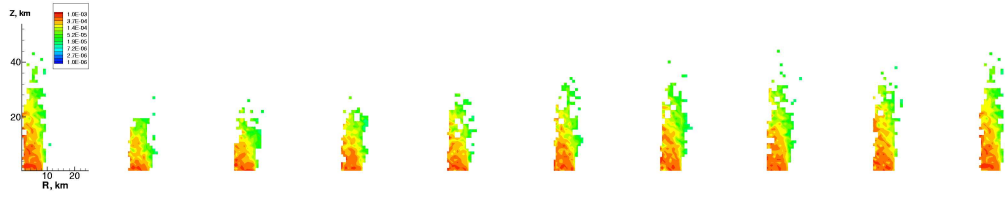
Figure 5.44: Time evolution of SO_2 ν_2 band emission contours of Pele type plume with an unsteady source. Time interval between each frame is 80 s. The source number density is kept constant but the source velocity has an oscillating period of $\sim$30 min. The oscillating amplitude is a nominal 30% of the mean vent velocity of 1000 m/s.

163
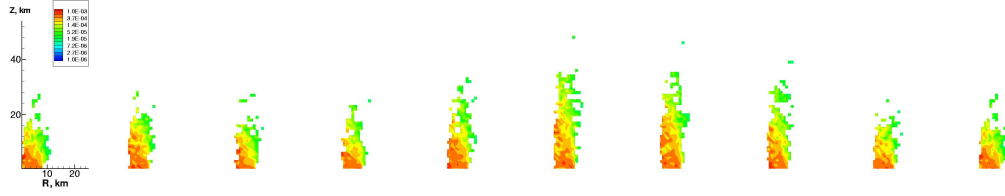
Figure 5.45: Time evolution of SO$_2$ ν_2 band emission contours of Pele type plume with an unsteady source. The conditions at the vent are the same as the case shown in Fig 5.38 except that the source velocity has an oscillating period of $\sim$10 min.
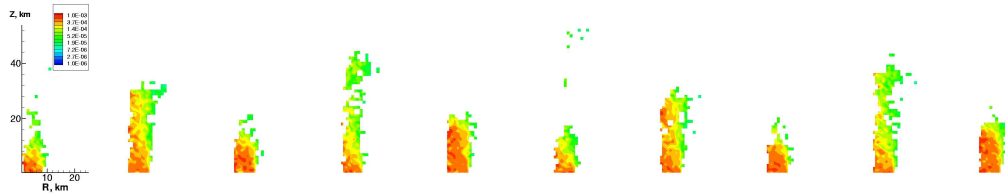
Figure 5.46: Time evolution of SO$_2$ ν_2 band emission contours of Pele type plume with a unsteady source. The conditions at the vent are the same as the case shown in Fig 5.38 except that the source velocity has an oscillating period of $\sim$1 min.
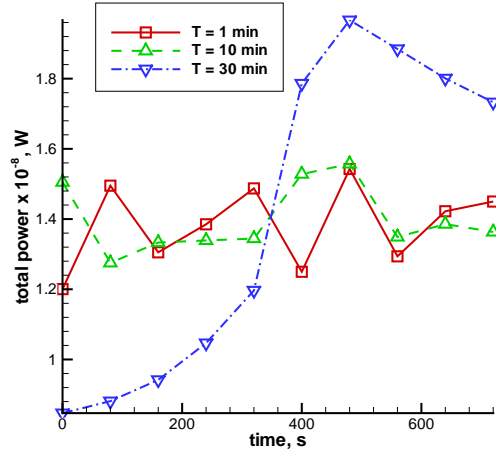
Figure 5.47: Time evolution of total rotational emission power of Pele type plume with unsteady sources.

while a vent gas pressure much larger than the ambient pressure will result in a overpressured (underexpanded) plume (Kieffer 1982). However, since the ambient atmosphere (presumably a sublimation atmosphere) has a scale height of only ∼8 km on dayside, it is relatively thin compared to the plume height. Therefore, once the plumes rise above the ambient scale height, they all virtually become underexpanded.

While the complexity at the vent may also cause the irregular plume shape, an alternative explanation of the difference in the plume shape is suggested here. It is possible that the Prometheus and Pele plumes were in steady state when being observed by Voyager, while the Loki plume was still developing and had just erupted and had not reached a steady state (presuming that the exposure time is less than a few minutes.) A suggested transient flow

165
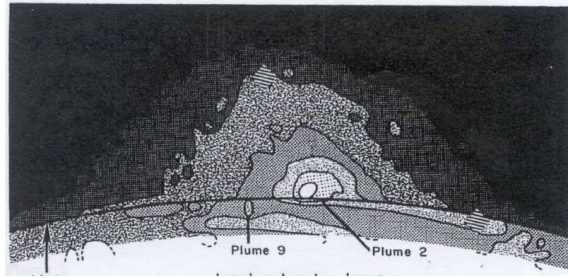
Figure 5.48: Voyager image of the ultra-violet brightness of Loki, (*From Strom and Schneider (1982), courtesy of Robert Strom*)

appropriate for Loki plume is simulated and the initial developing stage before steady state is shown in Figs. 5.49a–d. The corresponding TCDs of these plumes are shown in Figs. 5.50a–d for further comparison with the Voyager image. It is indeed seen that the plume at the early erupting stage ($< \sim 500$ s) is diffuse and does not have an umbrella shape. As the plume further develops, a steady state is reached just as for the Prometheus and Pele plumes and a steady state umbrella-shaped plume can also be formed. So, it is possible that Voyager caught a transient bursting or erupting stage for Loki and other plumes that do not have a symmetric umbrella shape. It is worth pointing out, though, that the simulated TCD could not reproduce the contour shape in the vent vicinity in the Voyager image. This is similar to the discrepancy previously discussed for the Pele image. Further investigation of large micron-size particle flow and other velocity profile shape at the vent (*e.g.* a fan shape mean velocity profile) are needed to finally match the vent vicinity contours in these images.

166
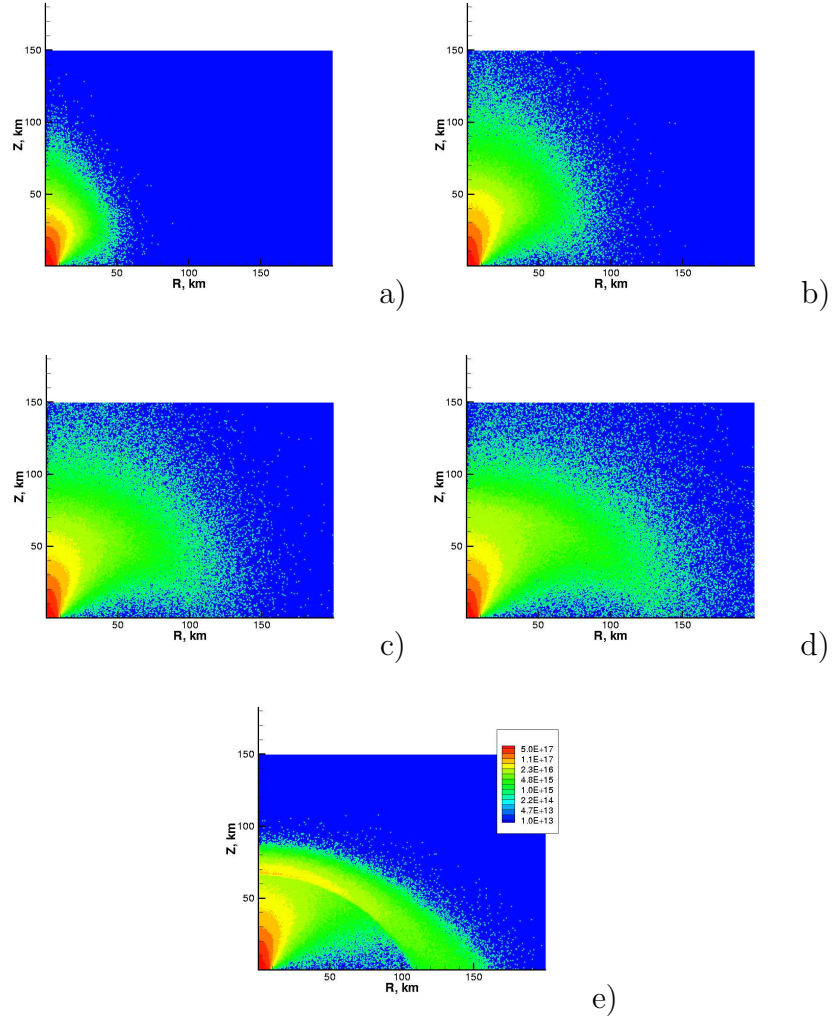
Figure 5.49: a) – d) Time evolution of the number density contours of simulated Loki plume. Time interval between each consecutive frame is 100 s. e) is the steady-state (reached after ∼800 s) number density contours of the plume.
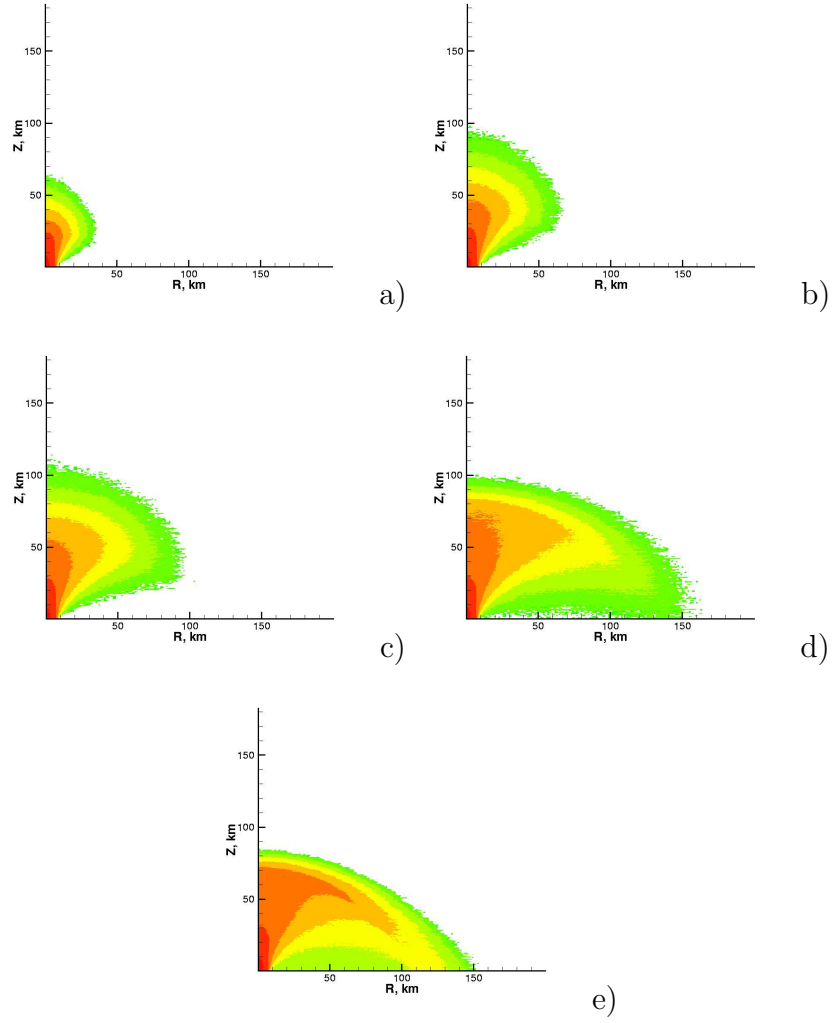
Figure 5.50: Time evolution of the TCD contours of the corresponding transient Loki plumes shown in Figs. 5.49.

5.8.3 The Effect of Parabolic Vent Velocity Profile

It has been argued in Chapter 3 that a uniform instead of a parabolic velocity profile at the vent is reasonable at relatively high Reynolds number ($\sim 5 \times 10^4$ for Pele) if one assumes pipe-like flow out of a relatively straight subsurface conduit. A plume flow with a parabolic velocity profile at the vent is examined here. The results suggest that the parabolic velocity profile does not seem to reproduce the observed plume shape of Pele. The vent temperature and velocity of 650 K and 1000 m/s which best reproduce the observed Pele plume shape with a uniform velocity profile are first tested. Figure 5.51a shows that the plume shape is appreciably different from the observed umbrella shape with the plume diameter being almost half of the observed diameter. One can adjust the vent parameters in order to try and reproduce the observed plume height and width. For example, since the plume diameter is too small for the case shown in Fig. 5.51a, one could increase the vent temperature. However, the plume shape (the aspect ratio of plume height and diameter) still does not resemble the observed umbrella shape as seen in some examples shown in Figures 5.51b and c. Therefore, we conclude that a uniform vent velocity profile is more reasonable than a parabolic one.
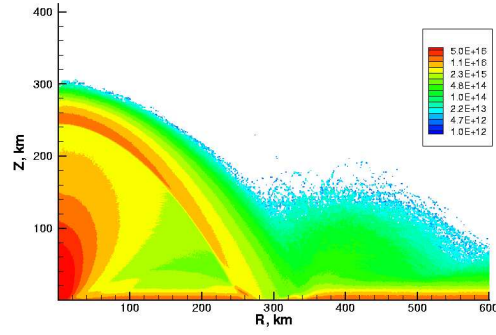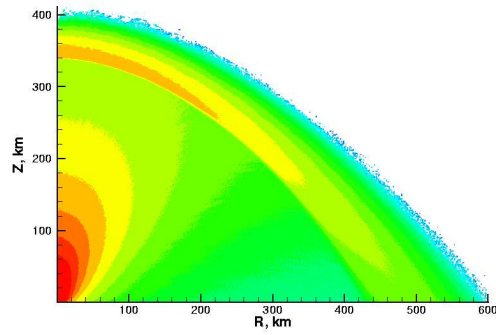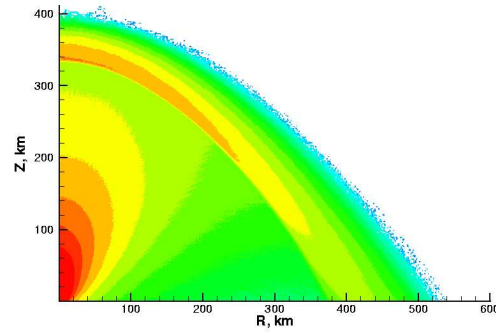
Figure 5.51: Number density contours of simulated plumes with parabolic vent velocity profile. The vent temperature and vent velocity at the center are a) 650 K, 1000 m/s, b) 1500 K, 1000 m/s, and c) 1200 K, 1100 m/s. The surface temperature in a) is 111 K.

170

Chapter 6

Discussion

6.1 What does Our Modeled Vent really Represent?

The dependence of Pele's vent pressure on vent temperature has been calculated by Zolotov and Fegley (2001) based on the HST observed SO_2/S_2 and SO_2/SO ratios in the plume (McGrath *et al.* 2000, Spencer *et al.* 2000). The vent temperatures they assumed are high (around 1700 K) in agreement with the recent Galileo NIMS observations by Lopes-Gautier *et al.* (2002). Zolotov and Fegley (2001) calculated a total vent pressure, for the observed gas species, of 0.01 – 2 bars in this temperature range ($\sim$1700 – 2000 K). This result is drastically different from our previous vent conditions–we found a vent static pressure of only $\sim$ 40 nanobar and temperature of 650 K for Pele. However, the vent appropriate for the model of Zolotov and Fegley (2001) and our model should be distinguished.

There thus remains the question of what our modeled vent really represents. We propose that our modeled vent may be interpreted as a "virtual" vent representing the location - a relatively "clean" plane - where the gas temperature and velocity reach the modeled values. A schematic diagram of such a virtual vent is shown in Figs. 6.1a and b for a volcanic tube and lava lake

plume, respectively. Our virtual vent is not necessarily right at the exit of a volcanic tube or at the same location appropriate to the model of Zolotov and Fegley (2001). Our virtual vent is assumed to be close to the exit where the flow is supersonic and the temperature has dropped below the lava temperature. A modeled vent diameter of $\sim$10 - 20 km in this context is thus reasonable. The match to the Voyager image of Prometheus we obtained provides further support of this idea. The contour dimension in the vent vicinity is on the order of 10 - 20 km in the Voyager image. A very likely scenario for the source of Prometheus is that a large number of bubbling sites of dimension of $\sim$10 - 100 m are distributed over a region of $\sim$ 20 km in diameter. We have recently been able to model this kind of volcanic plume with a diffusing disk (simulating an evaporating lava lake) as the source. We do so by specifying a temperature and a reasonable number flux at the disk with the same size of our nominal vent ($\sim$8 km in radius). A lower bounding steady state Mach number of $\sim$0.7 adjacent to the disk is found regardless of the disk temperature. Further details are discussed in Appendix C. For the Pele plume seen in the Voyager image (*cf* Fig 5.15a), the contour dimension in the vent vicinity is even larger and on the order of 100 km though the image saturation in the vent vicinity may also contribute to the large size of the contours. In this case, what happens may be similar to that in Prometheus except that the bubbling sites be replaced by deeper cracks or holes. Some of our results show that a diffusing disk at $\sim$1700 K could also be a possible source for Pele. Interestingly, this is consistent with the high lava temperature observed at

172

Pele (Lopes-Gautier *et al.* 2002), and this is the reason we mark a "lava lake" region in Fig. 5.1a for Pele.

The "virtual" vent idea appears to be a little arbitrary. This situation is caused by the relatively large uncertainties involved in observation. If there were an "exit" - the "clean" plane parallel to the surface as shown in Figs. 6.1a and b - where every relevant parameter, such as the width of the gas stream crossing the plane, the gas temperature and velocity, could be simultaneously determined by observation, then we believe that our model would reproduce the plume flow well. Unfortunately, this is not the case for the observations on Io. We almost know nothing definite at the vent, nor has a vent been observed directly. Thus, it is strongly suggested that, in the future, observations focus on the direct measurement of the velocity and temperature specifically for the gas at a well defined location, say a certain plane parallel to the surface with good knowledge of the size of the gas stream crossing the plane. It is understood that this task is difficult for remote sensing.

Given the current situation, what can we say more specifically about our modeled vent and the vent conditions constrained by the model? First, the "virtual" vent must be close to the actual exit. For example, as mentioned earlier in this section, a diffusing disk at ∼1700 K could also be a possible source for a Pele type plume. In that simulation, the flow reaches Mach 3 (from Mach ∼0.7 at the disk) within ∼15 km above the disk. This is relatively short compared to the height of a Pele type plume.

Second, the most important parameters at the vent are the velocity (V_v)
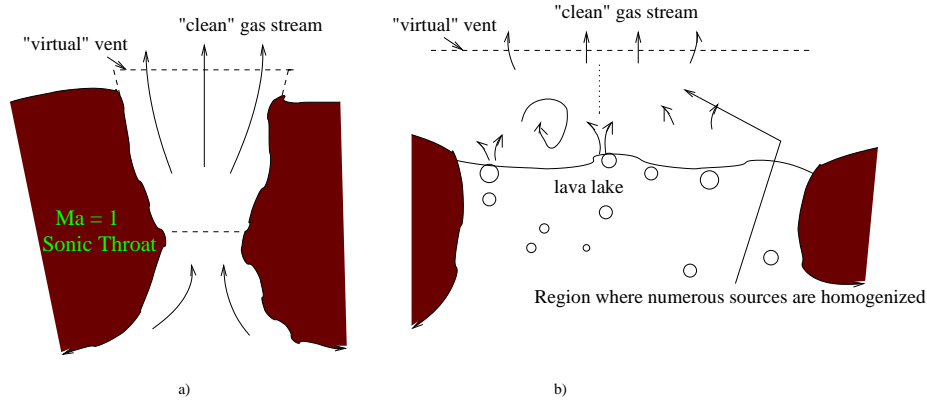
Figure 6.1: Schematic diagram of "virtual" vent.

and temperature (T_v), which determine the kinetic and internal energy of the gas and ultimately the height and width of the plume. Other parameters – the vent size, the number density at the vent, the vibrational degrees of freedom and vibrational relaxation numbers (discussed in Appendix A), opacity of the gas and the presence of other species – appear to perturb the plume height and width slightly, usually about $10 - 20$ % as seen throughout this work. Thus, the constraints on the vent conditions (T_v, V_v) made in the present work are reasonably accurate.

In the lava lake plume simulations, the gas pressure in the hot lava lake vicinity is still in the range of tens to hundreds of nanobar which is much less than the equilibrium SO_2 vapor pressure over lava at a high lava temperature. It should be noted that equilibrium is not reached when there is a steady-state dynamic expansion with the vapor generated at the surface expanding into a near vacuum. Therefore, the dynamic expansion must be considered when

linking the calculation of vent pressure by Zolotov and Fegley (2001) to the resulting escaping gases.

It should be pointed out that the dynamic expansion from the lava vicinity to our "virtual" vent is very complex due to radiative heating of the gas from the hot lava, gas radiative losses to space, and possible mixing of the gas from different degassing spots (say, from along a fissure in the crust of a lava lake). A detailed investigation, beyond the scope of the present work, is needed to examine the process that connects the degassing in the lava and the virtual vent region.

6.2   Evaporating Lava Lakes as Volcanic Sources

In the lava lake plume simulations, we have seen that a Prometheus type plume with a canopy shock developed can indeed be achieved with appropriate disk conditions ($T_d \sim 350$ K). A simple sublimation atmosphere can also be produced by an evaporating disk under low temperature conditions. It is thus interesting to further investigate what determines the type (volcanic plume or sublimation atmosphere) of the flow from an diffusing or evaporating disk. To examine this issue, a wide temperature range of the evaporating disk needs to be explored. This parametric study has been done and was discussed briefly in the previous section. Here, a dimensional analysis is provided to find the parameter that determines the type of the resulting flow. We find that the plume morphology (non-dimensional canopy height, h/r, or canopy diameter, d/r) is a function of a non-dimensional number $S = RT/gr = H/r$, where H

175

is the scale height[1] of the sublimation atmosphere at the disk temperature, T, and r is the radius of the disk. S can be interpreted as the measure of the tendency to develop a volcanic plume instead of a sublimation driven atmosphere. The larger the value of H compared to r, thus the larger the value of S, the more likely it is that a volcanic plume with a canopy shock will be formed from the evaporating disk. A large S corresponds to a large scale height or a small evaporating disk. If S is small, a low speed sublimation-driven flow is developed without the formation of a canopy shaped shock in the plume. Figure 6.2 indeed shows that when S is less than one, a low speed sublimation-driven flow is formed without developing a canopy shock whereas a volcanic plume with a distinct canopy shock is formed if S is larger than one. Therefore, a critical value of S of ~1 is suggested as the transition point for forming a volcanic plume with canopy shock presence. Figure 6.3a further illustrates the quantitative functional dependence of volcanic plume morphology on S. It is seen that the parameters of plume morphology depend approximately linearly on S within the parameter space explored.

If there is a subliming frost around the diffusing disk, the ambient sublimation atmosphere could also have an effect on the flow from the disk. To examine this effect, a nominal surrounding frost temperature of 110 K is tried. Figures 6.4 and 6.5 illustrate the Mach number and number density fields of the plumes with different disk temperatures[2] and an ambient atmosphere.

---

[1]The scale height is used in a broad sense here since at high disk temperature a volcanic plume may be developed.

[2]Note the diffusing disk is in a general sense and some of the disk temperatures may not

a) $S = 0.86$

b) $S = 1.7$

c) $S = 0.86$

d) $S = 1.7$
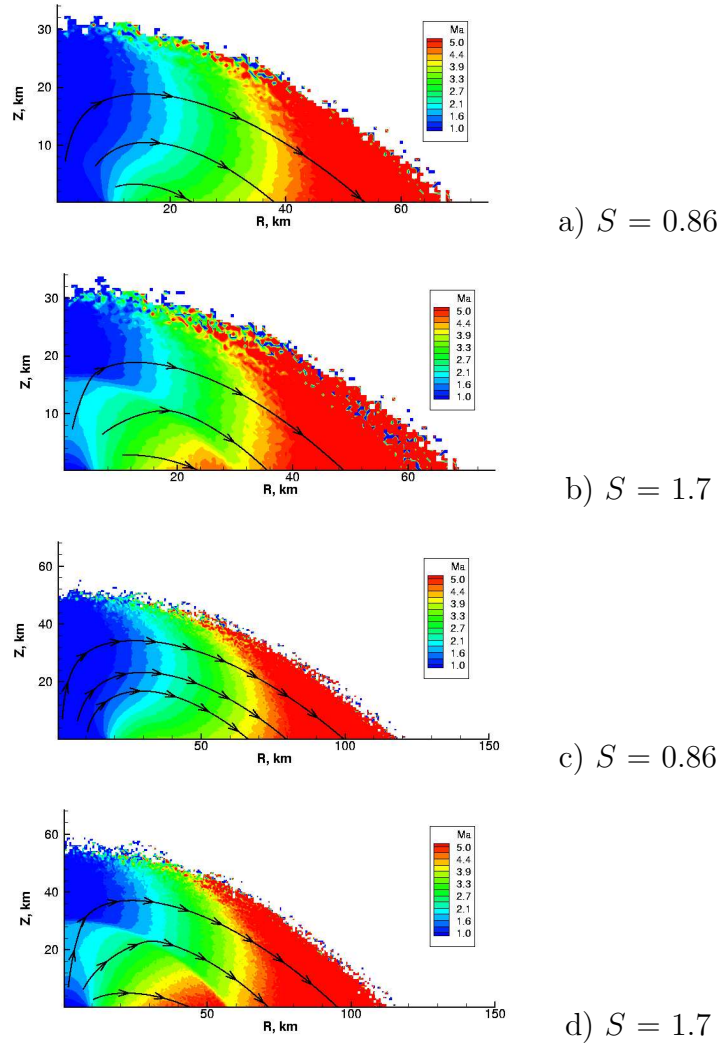
Figure 6.2: Mach number contours of gas plume from diffusing disks with $S = RT_0/r$, disk temperature, T_0, and disk radius, r, of a) 0.86, 100 K, and 8.4 km, b) 1.7, 100 K, and 4.2 km, c) 0.86, 200 K, and 16.8 km, and d) 1.7, 200 K, and 8.4 km. A shock starts to appear for S greater than one.

177
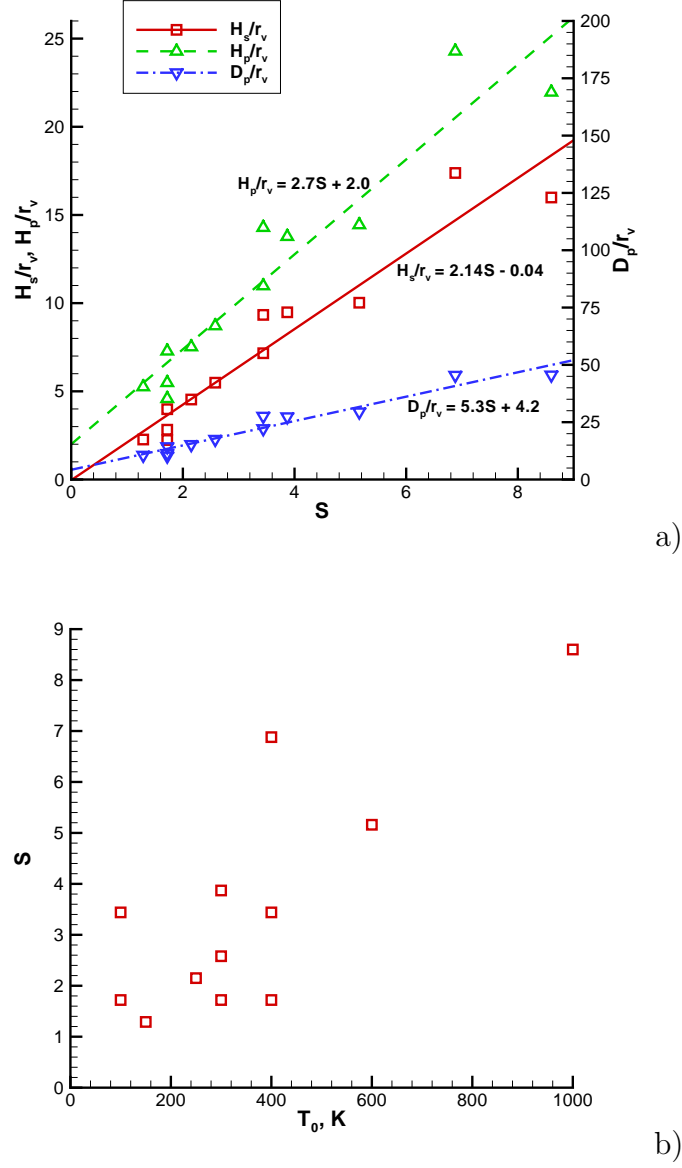
Figure 6.3: a) Shock height, plume height, and plume width normalized by the radius of the diffusing disk (r_v) as functions of S. b) The parameter space explored to obtained the curve fits shown in a). Both the temperature of the diffusing disk (T_0) and the radius of the disk are varied in the study.

Apparently, for a plume to penetrate and blanket the ambient atmosphere, it is necessary for the plume to have a shock height H_s greater than the scale height H_a of the ambient atmosphere. In this case, for example, the plume with disk temperature of 150 K rises appreciably above the ambient atmosphere since the shock height H_s (15 km) of the plume is larger than the scale height ($\sim$8 km) of the ambient atmosphere at the surface temperature of 110 K. Another necessary condition for a plume to penetrate the ambient atmosphere is that the vapor pressure near the disk (p_d) is higher than that of the ambient pressure (p_a) near the surface. Otherwise, the ambient atmosphere could be dominant and even stop the plume from developing if the gas pressure near the disk is too low. In the cases shown in Fig. 6.4, the gas pressures near the disk are $\sim$20 times larger than the ambient pressure near the surface. However, if p_d is lower than p_a, a plume cannot form as shown in Figs. 6.6c and 6.7c where the *initial* p_d is $\sim$3 times lower than that of the ambient pressure. In this case, a "backward" flow from the ambient atmosphere to the disk actually develops until the vapor pressure near the disk equilibrates with the ambient pressure.

6.3 What is the Source of the extremely Fine Particulates in the Outer Portion of Prometheus Plume?

The small particles in the outer portion of Prometheus plume discussed in Section 5.3.1 could be dust or pyroclastic particles entrained in the gas plume, or volatile SO_2 snow-flakes, droplets and/or crystals that formed via

---

be appropriate to representing lava temperature.

179
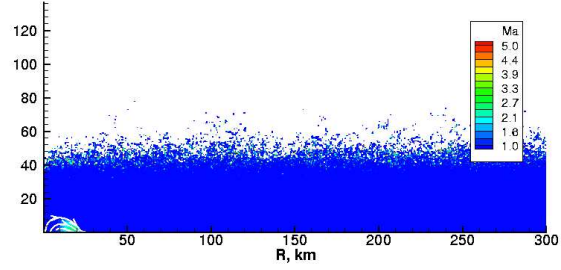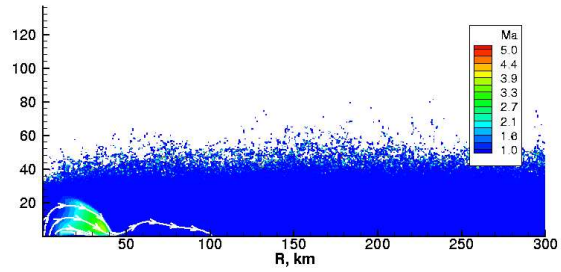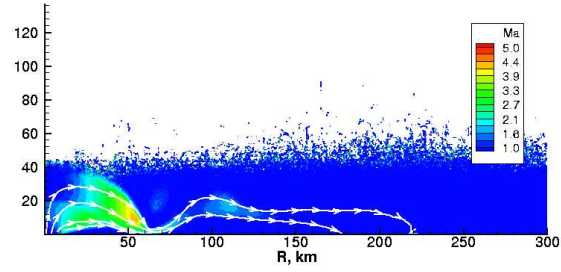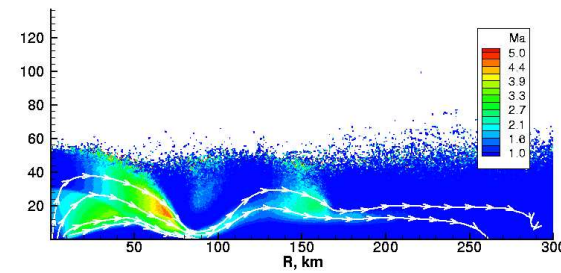
a) $S = 0.43$

b) $S = 0.86$

c) $S = 1.29$

d) $S = 1.7$

Figure 6.4: Mach number contours of gas plume with lava temperature of a) 50 K, b) 100 K, c) 150 K, d) 200 K. Note the same disk size of r of 8.4 km and the surface temperature is a nominal 110 K.
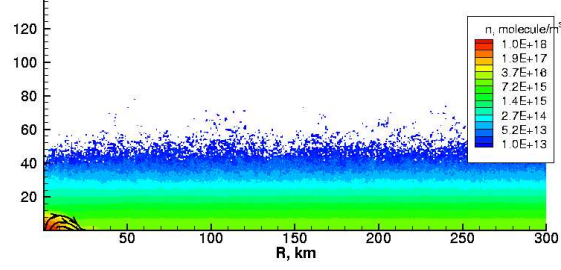
a) $S = 0.43$
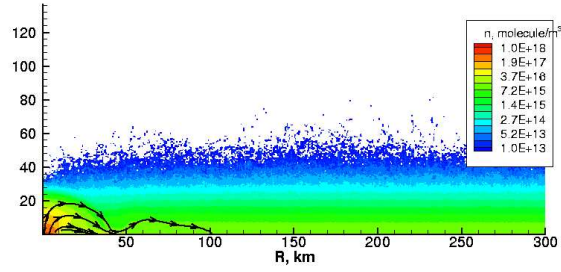
b) $S = 0.86$
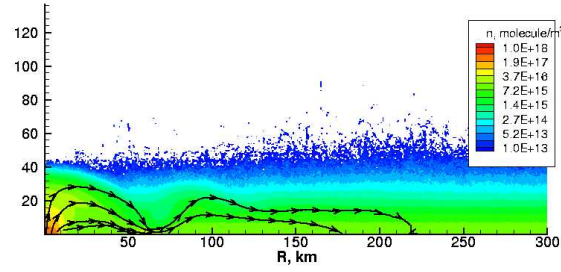
c) $S = 1.29$
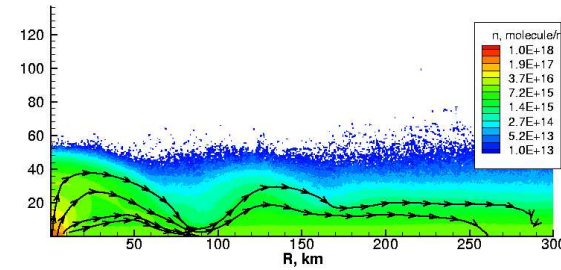
d) $S = 1.7$

Figure 6.5: Number density contours of gas plume with lava temperature of a) 50 K, b) 100 K, c) 150 K, and d) 200 K. Note the same disk size of r of 8.4 km and the surface temperature is a nominal 110 K.
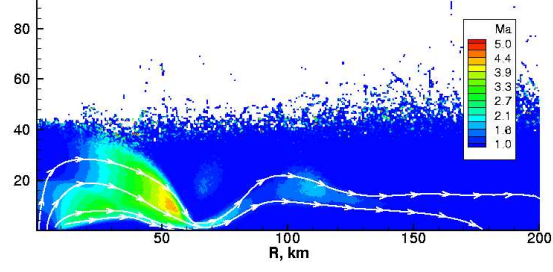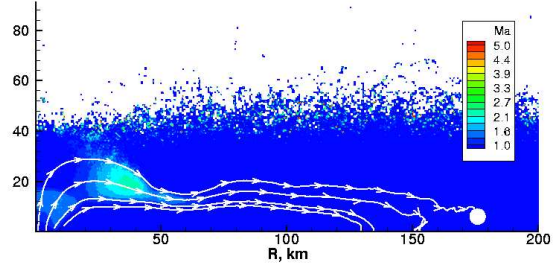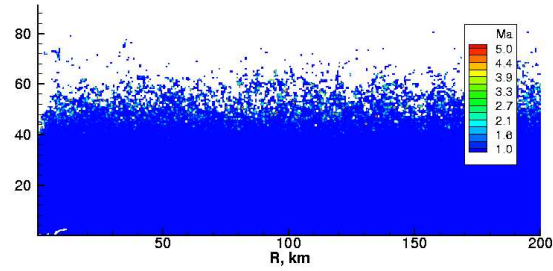
Figure 6.6: Mach number contours of gas plume (lava temperature of 150 K) with vent pressure of a) ~20 times larger than, b) about the same as, and c) ~3 smaller than the equilibrium SO_2 vapor pressure at 110 K. Note the same disk size of r of 8.4 km and the surface temperature is a nominal 110 K. p_v is varied at constant T_v by varying ρ_v.
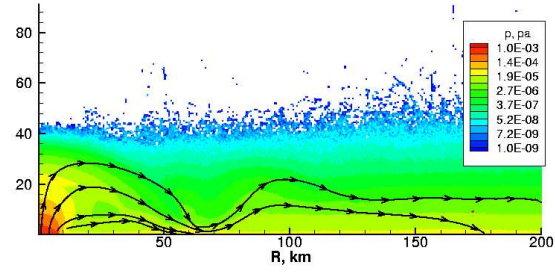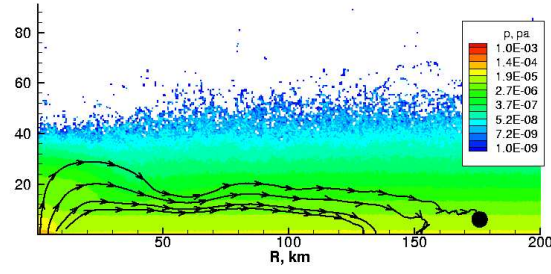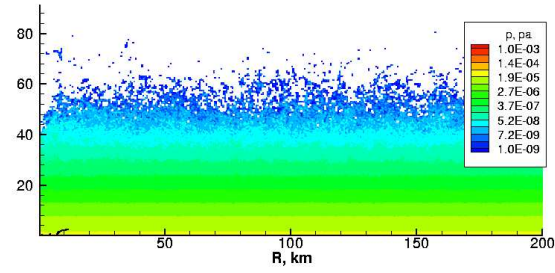
Figure 6.7: Pressure contours of gas plume (disk temperature of 150 K) with gas pressure of a) ∼20 times larger than, b) about the same as, and c) ∼3 smaller than the equilibrium SO_2 vapor pressure at 110 K. Note the same disk size of r of 8.4 km and the surface temperature is a nominal 110 K.
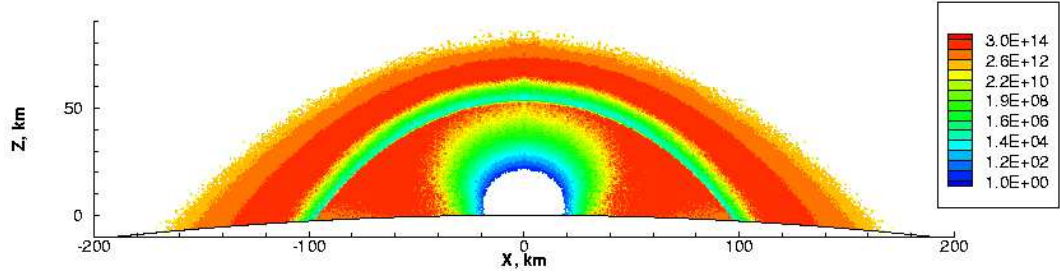
Figure 6.8: The ratio of local gas pressure to the equilibrium vapor pressure for a simulated Prometheus type plume. Notice the logarithm color bar. The regions where the ratio is less than one are blanked. Colors indicate possible condensation.

condensation in the plume. Both refractory particles and volatile condensates may be present. Although none of these possibilities can be excluded yet, the plausibility of particles formed via condensation in the plume is examined briefly. In fact, the conditions in the plume away from the vent vicinity are quite favorable for these particles to form through inter-molecular collisions. Figure 6.8 shows the contours of the ratio of the local gas pressure (nkT, where n is the local gas number density, k is the Boltzmann constant, and T is the local gas temperature) to the local equilibrium vapor pressure (Ingersoll *et al.* 1985) ($P_{vapor} = 1.52 \times 10^{13} e^{-4510/T}$) for a Prometheus type plume. The figure indicates that most regions within the Prometheus plume away from the vent vicinity are highly super-saturated, and the conditions are favorable for condensation. It is not yet certain if collision rates are sufficient to grow substantial particles or whether the temperature of such particles is even close to the local gas temperature. It is also understood that P_{vapor} is that over

184

a macroscopic sheet of ice and the nano-particles may have a different equilibrium vapor pressure. Moreover, the kinetic temperature in non-equilibrium conditions that occur in many locations of the plume may be misleading. Still, it is likely that as the gas plume cools via both expansion and radiation, some condensation occurs inside the plume. The particles formed (SO_2 snow-flakes, droplets and/or crystals) may be very fine (< 10 nm) and track the gas flow in the outer portion of the gas plume accounting for the Voyager observed plume brightness in those regions. In fact, Kieffer (1982) had a detailed discussion of condensing vapor for both an equilibrium and a non-equilibrium situation, and suggested that condensation of SO_2 could occur in an expanding flow and the condensate particles would be generally less than 100 nm. It has also been shown that, for a sticking coefficient of 0.1, the maximum size of particles that could grow through condensation of SO_2 is ~ 50 nm (Moore *et al.* 2003).

6.4 Subsolar Frost Temperature on Io − Implication of Relative Significance of Volcanic/Sublimation Atmospheres

Our modeling suggests that the observed lateral extension of the Pillan plume (*cf* Fig. 1.1) and multiple ring structure around Prometheus imply that the temperature of frost near the subsolar point is greater than ~ 110 K. Combining this with the upper limit we suggested in Section 5.3.2 of Chapter 5, the subsolar frost temperature range would be $\sim 110 - 118$ K. It is interesting that the corresponding density of a SO_2 sublimation atmosphere for subsolar

frost temperatures in this range is precisely in the range to play a significant role in the gas dynamic interactions with plumes, the parameters of which are independently chosen. Rathbun *et al.* (2003) obtained a subsolar surface temperature of ~133 K based on the Galileo Photopolarimeter-Radiometer (PPR) observation. However, though this was not pointed out by Rathbun *et al.* (2003), a careful examination of the surface temperature map (their Fig. 1) near the subsolar point reveals that high subsolar surface temperatures seem to be correlated with dry surfaces (dark area) with little frost coverage while relatively low surface temperatures (less than 120 K) are observed in bright areas presumably covered with frost. Therefore, our constraint on the subsolar frost temperature appears to be consistent with the Galileo PPR observation.

Ingersoll (1989) pointed out that "the key unknowns for Io are the strength of the volcanic sources and the temperature of frost near the subsolar point". The recent Galileo PPR observation (Rathbun *et al.* 2003) gives a better understanding of subsolar surface temperature. However, the relative significance of volcanic/sublimation atmosphere is still controversial. Our modeling suggests constraints on these unknowns, i.e. a subsolar frost temperature of less than 118 K, virtual vent velocity of ~150 m/s for Prometheus-type plumes and ~900 m/s for Pele-type plumes and a source number density of ~5 $\times 10^{17}$ molecules/m^3 for both types of plumes with an virtual vent diameter of ~16 km. Thus, the relative significance of volcanoes or frost in maintaining the atmosphere on Io may be assessed. On the nightside, the surface temperature is low so that the only substantial atmospheres are beneath the

186

plumes and the length scale associated with each plumes can be obtained from Fig. 5.1. In plumes the vertical column density drops quite rapidly with distance from the vent. Figure 4.18 shows that the column density decreases by an order of magnitude within 100 km for both type of plumes. The only place where a sublimation atmosphere will play an important role is on the dayside around the subsolar region because of the rapid variation of vapor pressure with temperature. Figure 4.18 indicates that the column is dominated by the volcanic plume within $R = \sim100$ km, while the sublimation atmosphere plays an important role farther away from the vent, where the plume is only a small perturbation. However, the relative significance of plume atmosphere discussed above is in terms of column density. The relative role may not be the same for other observations like inferred temperature or species composition of the atmosphere. Figure 4.16 shows that although the column density is dominated by the sublimation atmosphere ~100 km away from the vent, the plume locally rises way above and blankets the sublimation atmosphere. The plume gas shows dramatic dynamic features such as a canopy and re-entry shocks and bounces. Therefore, to emphasize and reiterate what was suggested in the literature review section, even when both sublimation atmosphere and volcanic plumes are present at the same time, and the sublimation atmosphere dominates the value of the column density, volcanic plumes may still play important roles in other aspects of the atmosphere like its temperature, interaction with the plasma and radiation from space and its composition. Thus, when discussing the relative significance of volcanic/sublimation atmosphere, one must

be specific about the particular aspect one is interested in. The effect of the Prometheus plume on the atmospheric temperature inferred by Jessup *et al.* (2003) should be assessed. Similarly, the effect of plumes on the interaction of the upper atmosphere with the plasma torus and radiation from space should be studied; Wong and Johnson (1996) neglected volcanic plume flows in their model.

Chapter 7

Conclusions

Volcanic plumes on Jupiter's moon Io are modeled using the direct simulation Monte Carlo (DSMC) method. The main goal of this work is to improve the understanding of Ionian atmosphere itself and the internal processes that are responsible for the volcanic plumes with rarefied gas dynamics modeling techniques developed for aerospace engineering applications. Increasing confidence in our model has been built up through the encouraging matches to and agreements with a variety of observations, such as plume shape, vertical gas column density in the plumes, plume images, plume shadows, ring depositions, *etc.*. Uncertainty and question remain, most importantly, how to connect our modeled virtual vent to the ultimate internal processes.

The most important conclusions are

- A DSMC model including innovations of spherical geometry, variable gravity, internal energy exchange (discrete VT and continuous RT exchange) in the gas, infrared and microwave emission from the gas, multi-domain sequential technique to resolve the fast emission events, opacity and two phase gas/particle flow, has been developed.

- A concept of virtual vent is proposed and the parametric study of the two most important parameters at the virtual vent - velocity and temperature - is performed. Constraints are put on the vent conditions via the observables such as the canopy shock height, peak gas deposition ring radii, vertical and tangential gas column densities, and total gas mass and emission power.

- A virtual vent temperature of 650 K and velocity of 900 m/s is appropriate for a nominal Pele type plume, and a diffusing disk (simulating evaporating lava) at 350 K can reproduce the Voyage Prometheus image well.

- A nominal source rate of 10^{29} SO$_2$ s^{-1} is found to be suitable for all types of the plumes (Pele or Prometheus, tube or lava lake). The source number density needs to be adjusted when varying the virtual vent size. Opacity of the gas can be important when the vent size is small ($<\sim 1$ km in radius).

- Typical gas plume flow features include a canopy-shaped shock, multiple bounce re-entry shock structure on the dayside, ring deposition, concentration of emission in the vibrational bands in the vent vicinity and re-emission at the shocks for certain band.

- An upper limit on the size of spherical particles that can track the gas flow in the outer portion of the plumes is ~ 10 nm. Particles of size ~ 1 nm can track the gas flow well throughout the entire plume. The

190

Voyager plume images of Pele and Prometheus are matched with both gas and 1 nm particle column densities. Galileo images of shadow cast by Prometheus plume is reproduced with the calculated shadows of particle plumes.

- Indications of possible multiple rings are observed in the diurnal averaged SO_2 gas deposition around simulated Prometheus plume. There are no multiple instantaneous S_2 deposition rings around simulated Pele plume. Multiple rings are seen in the particle deposition profiles.

- A subsolar frost temperature in the range of $\sim 110 - 118$ K is suggested.

7.1   Summary

A DSMC model including spherical geometry, variable gravity field, internal energy exchange and thermal radiation has been developed for the rarefied gas dynamic application to volcanic plume on Io. For the convenient calculation of inter-molecular collisions in DSMC, the molecules are moved in a Cartesian coordinate system with appropriate accelerations due to the gravity. The coordinates of the molecules are then transformed back to spherical coordinates for indexing. The variable gravity field is incorporated because it has noticeable influence on the trajectory of the molecules inside a large Pele type plume and thus affects the plume shape. However, it is not necessary to account for spherical geometry and variable g effects for small Prometheus type plumes.

Internal energy exchange during collisions between SO_2 molecules, *i.e.* vibration-translation (VT) and rotation-translation (RT) energy exchange has also been included. The modeling of RT energy transfer is performed using the Larsen-Borgnakke method, and a discrete version of the method is used for VT energy transfer because at the relatively low temperatures of present interest the vibrational modes can not be regarded as being fully excited. Thermal radiation from the vibrational bands and the rotational lines can then be modeled. The radiation due to $n \rightarrow n-1$ transition from higher (up to the third level) vibration levels is incorporated and it is assumed that $A_{n \rightarrow n-1} = nA_{1 \rightarrow 0}$. The rotational (microwave) cooling model of Lellouch *et al.* (1992) was originally used to calculate the microwave radiation from the gas. However, this model was recently found to cause error at high temperatures due to the missing of "hot" band transition data in Hitran. The near quadratic temperature dependence in which $R[Js^{-1}/SO_2] = 1.744 \times 10^{-28}T^{2.043}$ by the model of Varghese (2003) is used for SO_2 rotational emission in the present work.

A multi-domain sequential technique is developed to resolve the fast emission events in the vent vicinity. The whole domain is split into multiple subdomains and sequential calculations are performed from the inner to outer domains. The flow in the inner domains is computed with higher spatial and temporal resolutions to capture the fast emission events there. Molecules are passed from the inner to outer domains.

The criterion for the choice of spatial and temporal resolution is usually

192

based on the mean free path λ and collision time τ_{col}, respectively. This criterion is quite stringent for a non-adaptive single domain calculation. The less stringent but reasonable spatial and temporal resolution based the length and time scale in the flow structure are used in the single domain calculations and have been shown to converge.

A canopy-shaped shock appears in the simulated volcanic gas plumes and multiple bounce re-entry shock structure is present only in dayside plumes as the result of the interaction between the falling gas and the sublimation atmosphere. Frost ring deposition is found for nightside plume while frost depletion effect is found in a dayside plume. It is suggested that the turning flows near the re-entry shock entrain the upper part of the sublimation atmosphere which results in a (surprisingly) slightly lower surface pressure than the equilibrium vapor pressure; this causes the depletion of SO_2 frost from the surface by sublimation.

Gas column densities in the simulated plumes are found to be consistent with various observations. A nominal source rate of 10^{29} SO_2 s^{-1} is thus believed to be suitable for all types of the plumes (Pele or Prometheus, tube or lava lake). The total gas mass in a nominal Pele type plume is $\sim 1 \times 10^{10}$ g and the total microwave and infrared emission power are both $\sim 1 \times 10^9$ W in a optically thin Pele type plume. A cooler and smaller Prometheus type plume generally contains one order of magnitude lower total gas mass and emits a couple of orders of magnitude lower radiation than a Pele type plume.

For the three vibrational bands of SO_2, virtually all the emission power

comes from the plume core. For the overall rotational lines, the power emitted from the plume core is only about one tenth the total power from the whole plume. The emission from the three vibrational bands dominates in the vent vicinity but stops at an altitude of ~ 50 km. Radiative cooling mostly continues in the rotational lines at high altitude. The additional heating of the surface by plume emissions is found to be unimportant beyond a few tens of kilometers away from the edge of the vent.

A parametric study of vent conditions has been performed with certain reasonable assumptions about the vent region of Ionian volcanic plumes. A "virtual vent" was defined as the location where the gas temperature and velocity reach the modeled values. This concept makes our model applicable to either volcanic or lava lake plumes with the sacrifice of the detail connecting the reservoir to the virtual vent. With such a definition, a virtual vent of $1 - 10$ km in diameter appears reasonable. Two sets of iso-contours in vent velocity-temperature (V_v-T_v) space were created; one set corresponded to constant shock heights and the other to constant deposition ring positions. The virtual vent condition ranges appropriate for both Pele- and Prometheus-type plumes are constrained by matching the shock heights and the observed peak deposition ring radii. A unique determination of vent condition is possible for a Pele-type plume. A virtual vent temperature of 650 K and velocity of 900 m/s is appropriate for a nominal Pele type plume, and a diffusing disk (simulating evaporating lava) at 350 K can reproduce the Voyager Prometheus image well. The adjustment to the constraints due to the opacity of the gas

194

when the size of the virtual vent decreases is usually less than 10 - 20%.

The dilute flow of refractory nano-particles entrained in the gas plumes was modeled with two "overlay" techniques. The column densities along tangential lines-of-sight were calculated and compared with Voyager plume images. Encouraging matches to Voyager observations were obtained for both the gas and nano-particle TCDs in both Pele and Prometheus type plumes. The calculated TCD of gas near the shock is consistent with that inferred from HST observation (Spencer *et al.* 1997). An upper limit on the size of spherical particles that can track the gas flow in the outer portion of the plume was found to be $\sim$10 nm. We believe that some of these particles are likely formed through condensation in the gas plume although further study of this issue is required.

The shadows cast by Prometheus' particle plumes are computed and compared to a Galileo image. Multiple particle sizes best explain the observed image. The multiple ring deposition around Prometheus is likely to be explained by deposition of nano-particles. The particles that are ejected from the volcanic source are levitated by the gas "bounce" as they fall toward the warm surface so that they are deposited further from the source. The absence of any observed more distant dust clouds suggests that the subsolar frost temperature is less than $\sim$118 K, assuming that a cloud of 1 nm particles would be observable.

The transport of S_2 gas in a Pele type plume is examined. The S_2 gas closely follows the bulk SO_2 gas flow, and the S_2/SO_2 mixing ratio stays

approximately constant throughout the entire plume. S_2 deposits onto the surface even in a dayside plume even though the deposition rate is low due to the bouncing with SO_2. However, no multiple S_2 rings can be formed around Pele. Similar conclusions can be drawn for Na inside a Pele type plume. Preliminary results show inflation of the top of the plume by plasma bombardment. This could potentially explain the Na profile observed at high altitude.

The effects of unsteadiness of volcanic sources are investigated. The emission is enhanced at the moving shocks when the pulsing period is larger than the flow time, and for a stationary shock to be developed, it is necessary for the pulsing period T to be much shorter than the ballistic time t_0 determined by the mean velocity at the vent.

The absence of the canopy shock during the early developing stage of a plume could explain the non-umbrella shape of Loki. However, further investigations of large micron-size particle flow and the velocity profile shape at the vent (*e.g.* a fan shape mean velocity profile) are needed to finally match the vent vicinity contours in the Loki image.

7.2 Future Work

Roughly sorted by decreasing complexity or importance, the future areas of work suggested are:

- Connecting the reservoir details to the virtual vent proposed in this work.

- Incorporating condensing/evaporating of SO_2 snow/droplet mechanism in the model.

- A study of the Rayleigh-like scattering behavior of nano-sized particles. More image analysis like that of Strom and Schneider (1982) and Collins (1981) for the Galileo data.

- Reproducing the contour shape in the vent vicinity of Pele and Loki in the Voyager image maybe with a fan-shaped large particle velocity profile. Detailed observation in the vent vicinity is suggested.

- Developing a more sophisticated opaque gas model and completing the parametric study in the vent velocity-temperature-size space.

Appendices

Appendix A

The Effect of Vibrational Relaxation Number Z_v on the Gas Dynamics of Plumes

The significance of emission from the vibrational bands of SO_2 in the gas dynamics of a plume found in Section 5.6 makes it important to investigate the effect of vibrational relaxation number Z_v on the gas dynamics of plumes in greater detail.

As discussed in Chapter 3, the DSMC collision relaxation number (Z_v) is defined as the average number of inter-molecular collisions during a time interval that is equal to the vibrational relaxation time (Bird 1994), while the collision number (Z) in Bass *et al.* (1971) is defined as the average number of inter-molecular collisions necessary for a molecule to lose one quantum of vibrational energy. The relation between these two numbers can be expressed as (Lambert and Salter 1957),

$$Z = Z_c\beta(e^{-h\nu/kT} + 1) = Z_v(e^{-h\nu/kT} + 1) \tag{A.1}$$

where Z_c is the number of collisions one molecule suffers per second (collision frequency), ν is the frequency of the vibrational mode, and β is the relaxation time for that mode. Therefore, Z_v and Z are different by a factor of $(e^{-h\nu/kT} + 1)$ which matters at high temperature and can be at most 2. For a Pele type

plume, there is only $\sim 30\%$ difference between the two for the ν_2 vibration mode in the vent vicinity where temperature is 650 K and much less elsewhere. Since the flow time in the vent vicinity of Pele is only ~ 10 s and the VT collision relaxation time is ~ 1 s for the ν_2 vibration mode, the effect of $\sim 30\%$ difference betweent Z_v and Z_{10} on the gas dynamics would not be dramatic and even may be negligible. The effect is even less pronounced for the other two vibration modes due to their smaller populations and their slower VT collision relaxation.

Previously, the DSMC collision relaxation number for the ν_1 (1151 cm^{-1}) and ν_3 (1361 cm^{-1}) vibrational modes ($Z_{v,\nu_{1,3}}$) of SO_2 was assumed to be a constant value of 1000 instead of a function of temperature. It is also recognized that the difference between the collision relaxation number appropriate for DSMC (Z_v) and that (Z) defined by Bass *et al.* (1971) is not distinguished. It was argued that the assumption of constant Z is crude but is only aimed at an order of magnitude estimation. However, as will be shown in this section, unless one needs a very accurate ν_1 and ν_3 emission map, an accurate Z_v is not necessary for proper modeling of the gas dynamics. Moreover, the emission from those three vibrational bands does not differ by more than $\sim 20\%$ between the results obtained with a more accurate temperature dependent Z_v and with the previous crude model.

In our early simulations (Zhang *et al.* 2003a), a constant Z_{v,ν_2} of 300 based on the work of Bass *et al.* (1971) was used for the ν_2 vibration mode, and the difference between the collision relaxation number appropriate for

200
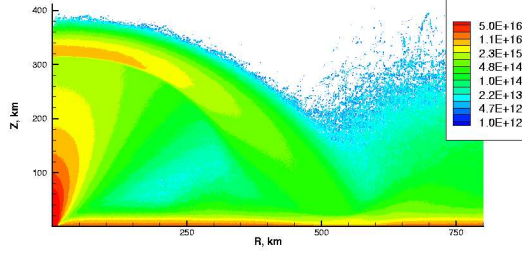
Figure A.1: SO_2 number density contours of simulated Pele type plumes with constant Z_{10} of 300 for the ν_2 vibration mode and temperature dependent Z_{10} for the ν_1 and ν_3 modes. The surface temperature is a nominal 111 K.

DSMC and that defined by Bass *et al.* (1971) was not distinguished either. To actually examine this effect, the model is revised such that a constant Z_1 (not Z_v) of 300 is used and Z_v is derived from Eqn. A.1 as $Z_1/(e^{-h\nu/kT} + 1)$ which is now temperature dependent. The resulting flow is illustrated in Fig. A.1. The differences in shock heights and plume shape between this plume and that shown in Fig. 5.27a (where a constant Z_v of 300 is used) are indeed negligible, and the differences in the number density, temperature and emission density are found small (generally $<\sim 8\%$) throughout most of the plume.

The effects of temperature dependence of $Z_{v,\nu_{1,3}}$ are also investigated. Due to the longer VT collision relaxation time (~ 10 s in the vent vicinity and even longer elsewhere) and the very small populations in the ν_1 and ν_3 modes, it is expected that the effects of temperature dependence of $Z_{v,\nu_{1,3}}$ are not important. The temperature dependence of Z_2 for these two modes is based on a curve fit to the experimental data of Bass *et al.* (1971) and is expressed

as,

$$Z_2 = e^{(50.T^{-1/3}-0.097)+5.19} = 163e^{50.T^{-1/3}} \tag{A.2}$$

and $Z_{v,\nu_{1,3}}$ is obtained by dividing this equation by $(e^{-h\nu/kT} + 1)$, where ν is the frequency of the ν_1 or ν_3 vibrational mode. The result shown in Fig. A.1 has incorporated this temperature dependent $Z_{v,\nu_{1,3}}$. The differences in the emission density of ν_1 or ν_3 bands between the flow shown in Fig. A.1 and that obtained from the previous model shown in Fig. 5.27a (where a constant Z_v of 1000 was used) are found to be generally less than $\sim 20\%$ and the plume shapes are virtually the same.

It is worth pointing out that the situation would be quite different if the VT collision relaxation number were smaller and the VT collision relaxation time were longer. When constant Z_{v,ν_2}'s of as small as 1 and 50 are tested, the flows (Fig. A.2) become appreciably different than that shown in Fig. 5.27a where a constant Z_{v,ν_2} of 300 is used. Due to the shorter relaxation time, there is more translation energy being "pumped" into the vibrational modes and therefore loss through emission to space. Thus, the plume expands less. Note that even the bounce is less dramatic in the flow with Z_{v,ν_2} equal to 1.

Finally in this section, it should be pointed out that the dynamics of Prometheus type plume is less sensitive to the Z parameters discussed above due to the shorter flow time (less than 10 min. compared to $\sim$20 min. for Pele) and generally lower temperatures. The effect of the Z_v has been examined but not shown since it is quite trivial.
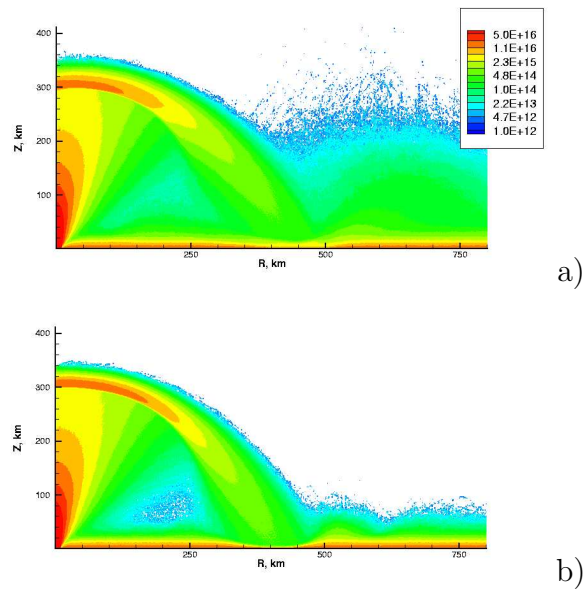
Figure A.2: SO$_2$ number density contours of simulated Pele type plumes with Z_{v,ν_2} = a) 50 and b) 1. The surface temperature is a nominal 111 K.

Appendix B

Rotational (microwave) Cooling Models

As mentioned in Section 3.2.2 of Chapter 3, Lellouch *et al.* (1992) did not provide a detailed derivation of the rotational cooling rate. A detailed explanation of this model is presented here.

The equation of radiative transfer at steady state can be expressed as (Vincenti and Kruger 1965):

$$\frac{\partial I_\nu}{\partial r} = \alpha_\nu (I_\nu - B_\nu), \tag{B.1}$$

where I_ν is the specific intensity, r is the distance from the boundary[1] where $r = 0$ and $I_\nu = I_\nu(0)$, α_ν is defined as the volumetric absorption coefficient with dimensions of inverse length, and B_ν is the Planck function. The solution of Eqn. B.1 is given as,

$$I_\nu = I_\nu(0)e^{-\tau_\nu(0)} + \int_0^r \alpha_\nu B_\nu(r')e^{-\tau_\nu(r')}dr', \tag{B.2}$$

where $\tau_\nu(r) = \int_0^r \alpha_\nu dr'$ is defined as optical depth at frequency ν. The first term in Eqn. B.2 represents attenuated transmission of radiation from an emit-

---

[1] Note that the location of the origin ($r = 0$) has been changed from that defined in Vincenti and Kruger (1965) at the point of question.

ting (boundary) surface. Neglecting this boundary term, Eqn. B.2 becomes

$$I_\nu = \int_0^{r'} \alpha_\nu B_\nu(r')e^{-\tau_\nu(r')}dr'. \tag{B.3}$$

The volumetric rate of energy addition (extraction) to the gas by radiation is

$$-\frac{\partial q_j^R}{\partial x_j} = \int_0^\infty \int_0^{4\pi} \frac{\partial I_\nu}{\partial r}d\Omega d\nu. \tag{B.4}$$

From Eqn B.3 we have

$$\frac{\partial I_\nu}{\partial r} = \alpha_\nu B_\nu(r)e^{-\tau_\nu(r)}. \tag{B.5}$$

Eqn B.4 then becomes

$$-\frac{\partial q_j^R}{\partial x_j} = 4\pi \int_0^\infty \alpha_\nu B_\nu(r)e^{-\tau_\nu(r)}d\nu. \tag{B.6}$$

Eqn B.6 is the volumetric cooling rate in W/m^3, and Lellouch *et al.* (1992) obtained the cooling rate per molecule essentially by dividing Eqn B.6 by the number density of the gas[2], N, yielding

$$R = 4\pi \int B_v k_v e^{-\tau}d\nu/N, \tag{B.7}$$

where τ is the optical depth of the gas. Lellouch *et al.* (1992) assumed an optically thin gas and obtained the rotational cooling rate as $R = 4\pi \sum_j B_{\nu_j} S_j$, where S_j is the strength of the jth rotational line. The line-by-line summation is then carried out to obtain the cooling rate.

A classical cooling model in which the molecule is treated as a decaying rotating dipole was studied and is compared to Lellouch's model. The classical

---

[2]There was a typographical error in Lellouch *et al.* (1992) p.289 which is corrected here.

rotational cooling rate by decay model is given by (Bird 1994) as

$$R = \frac{1}{2} I \omega^2 [1 - \frac{1}{1 + \delta \omega^2 \Delta t}], \tag{B.8}$$

where I is the moment of inertia of the considered molecules, ω is the angular velocity of the rotating dipole, and δ is defined by

$$\delta = \frac{\mu_e^2}{3 \pi c^3 I \varepsilon_0}. \tag{B.9}$$

where c is the speed of light, ε_0 is the free space dielectric constant and μ_e is the electric dipole moment. The angular velocity of the rotating dipole can be obtained by,

$$\frac{1}{2} I \omega^2 = E_r \tag{B.10}$$

where E_r is the average rotational energy per molecule. The classical model predicts a T^2 dependence, since Eqn. B.8 can be reduced to

$$\lim_{\delta \omega^2 \Delta t \to 0} R = \frac{1}{2} I \omega^2 \delta \omega^2 \Delta t = kT\delta(2kT/I)\Delta t \propto T^2 \tag{B.11}$$

where $\delta \omega^2$ is very small (2×10^{-2} s^{-1} at 700 K). The rotational cooling rates calculated by the classical model and the model of Lellouch *et al.* (1992) are compared in Fig B.1a for HCN (which is simple compared to SO_2). It is seen that very good agreement at low temperatures is obtained. However, as the gas temperature increases, a discrepancy between results of the two models is observed. The failure to include "hot" band transitions (the transition of rotational state at higher vibrational levels) causes the underestimate of the cooling rate by Lellouch's model. These "hot" band transitions are accounted
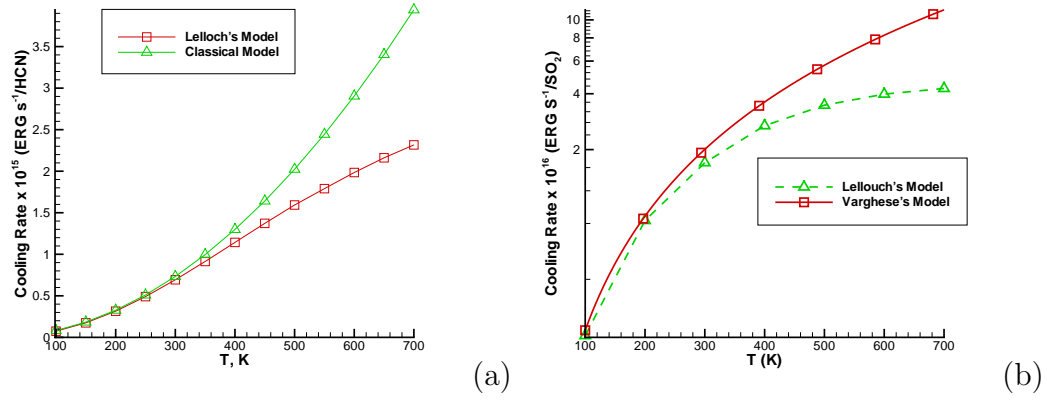
Figure B.1: Rotational cooling rate of HCN (a) and SO_2 (b).

for automatically by the classical model since the radiating molecules can be in higher vibrational levels. The error is also illustrated in Fig. B.1b for SO_2 by comparing the theoretical calculation of Varghese (2003) and the calculation of Lellouch *et al.* (1992). For example, $\sim 70\%$ error is introduced at temperature of 700 K. The model of Varghese (2003) predicts a near quadratic temperature dependence in which $R[Js^{-1}/SO_2] = 1.744 \times 10^{-28} T^{2.043}$.

Finally, it is pointed out that since SO_2 molecules have three distinct moments of inertia, one needs to find some kind of effective moment of inertia to use in Eqn. B.8 to calculate the rotational cooling rate. One can, in fact, obtain the effective moment of inertia by fitting the cooling rate obtained by the classical model to the correct spectra model (Fig B.1b).

Appendix C

Kinetic Theory Analysis of Steady-state Mach Number associated with the Evaporating Gas into a Vacuum

In our lava lake plume simulations, there appears to be a steady-state, lower bounding Mach number of ~ 0.7 right above the diffusing lava for all lava temperatures. This is shown in Figs. 5.1a and b. To find out why this is the case, one needs to find the distribution function (f_1) for the molecules between the diffusing surface and the vacuum boundary at steady-state. The distribution function (f_0) of the velocity component (u_z) normal to the diffusing surface for the diffusively generated molecules (source molecules) is,

$$f_0 = 2\beta^2 u_z e^{-\beta^2 u_z^2} \tag{C.1}$$

where β is the most probable molecular thermal speed $\sqrt{m/(2kT)}$. Note that the source molecules are not the same as the ones between the diffusing surface and the vacuum boundary (or in the first cell adjacent to the diffusing surface) at steady-state. The molecules in the first cell are, in fact, the slower moving ones that are left behind; faster molecules escape the first cell preferentially. The population of molecules of class u_z left in the first cell after a sufficiently

long time interval of Δt is,

$$\frac{l}{u_z \Delta t} f_0 du_z \tag{C.2}$$

where l is the length of the first cell in the direction normal to the surface. The distribution function (f_1) for these molecules is thus proportional to f_0/u_z which returns back to half-Maxwellian ($u_z > 0$ only) distribution after normalization:

$$f_1 = \beta/\sqrt{\pi}e^{-\beta^2 u_z{}^2} \tag{C.3}$$

Therefore, the mean z velocity of the molecules flowing between the diffusing surface and the vacuum boundary is,

$$\bar{u}_z = \int_0^\infty u_z f_1 du_z / \int_0^\infty f_1 du_z = \frac{1}{(\sqrt{\pi}\beta)} \tag{C.4}$$

which gives a Mach number right around 0.7 for SO_2. Note that since the velocity distribution f_1 is not strictly Maxwellian, the "temperature" of the gas averaged over all the molecules in the first cell is not the same as the diffusing disk temperature T_0. This is why there is a difference between the lava temperature and the gas temperature in our simulated lava lake Prometheus plume discussed in Section 5.3.1. Also, note that the distribution of the source molecules, f_0, gives a Mach number of $\sim$1.1.

The above analysis is further substantiated by the DSMC calculation. Figs. C.1 - C.3 show that the velocity distribution for the molecules adjacent to the diffusing surface is essentially the half-Maxwellian just as expected. Also, note that the velocity distribution of the diffusively generated molecules

in DSMC agrees with that expected (Eqn. C.1). This provides a validation of the routines used to generate molecule in our DSMC model.
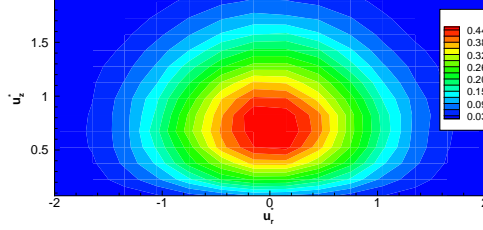

Figure C.1: Distribution function (f_0), sampled in DSMC, of (u_r^*, u_z^*) for diffusively generated molecules (source molecules) at the surface.
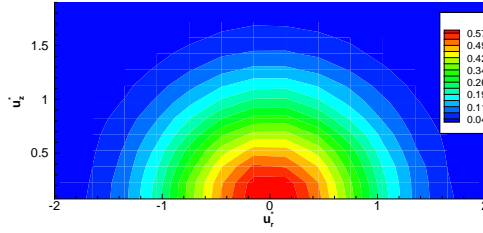

Figure C.2: Distribution function (f_1), sampled in DSMC, of (u_r^*, u_z^*) for molecules between the surface and the vacuum boundary at steady state.
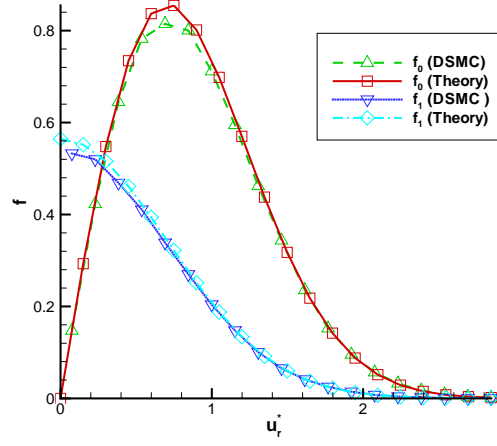
Figure C.3: Distribution function, both from theory and sampled in DSMC, of u_z^* for diffusively generated molecules (f_0) and the molecules between the surface and the vacuum boundary at steady state (f_1). Note the half-Maxwellian distribution for the flowing molecules between the surface and the vacuum.

Appendix D

Instability of the Canopy Shock due to Gravity

Under some circumstances, a "collapse" of the canopy shock is observed in the simulation of large Pele type plumes. An example is shown in Fig. D.1. It is observed that once a "lump" of gas near the shock as indicated by the dashed circle in the figure is formed, it becomes too heavy for the up-moving gas to maintain it at a fixed height. The "lump" keeps falling further as the result of gravitational pull. The cause of this instability is an insufficient number of simulated molecules. Due to the vast amount of expansion, the number density of the gas just below the canopy shock is several orders of magnitude lower than that in the vent vicinity for a large Pele type plume. Therefore, it is very difficult to maintain a reasonable instantaneous number (~ 50) of simulated molecules in each cell just below the shock. As a result, the instantaneous flow field there is usually "porous" and full of "bubbles", and the shock instability (collapse) occurs when there are too many "bubbles". This explanation can be illustrated by the following example in which only part of the plume close to the axis is simulated so that the instantaneous number of simulated molecules could be relatively easily increased by an order of magnitude in order to examine the effect of the number of simulated molecules. By comparing Fig. D.2 and Fig. D.3, it can be seen that when the instantaneous

number of simulated molecules is low, "wiggling" shape of the moving shock is seen indicating instability while the shape of the shock is much smoother if the instantaneous number of simulated molecules is sufficiently large. This instability does not occur in the simulation of small Prometheus type plumes in which the density of the plume does not vary as large as that of Pele type plumes and it is relatively easy to maintain sufficient instantaneous number of simulated molecules throughout the entire plume.

Although it is understood that such shock instability is computational, it may still occur physically if the shock is strongly perturbed. We have observed that when an artificial large "bubble" is introduced below the shock of a correct steady plume (with sufficient instantaneous number of simulated molecules), the shock will oscillate and eventually collapse. Therefore, it is suggested that axisymmetric shocks due to gravity such as those in our simulated plumes may be unstable to sufficiently large perturbations.
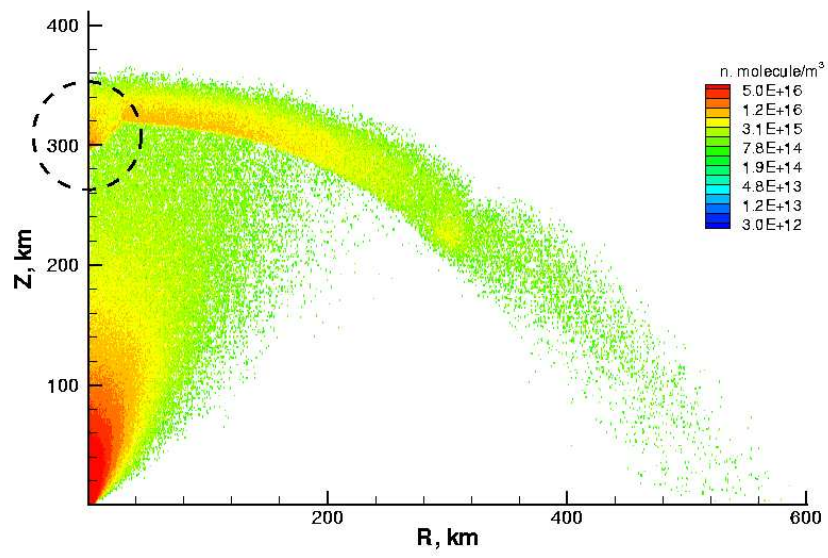
Figure D.1: Instantaneous number density contours of a simulated Pele type plume. Note the sign of "collapse" (instability) of the shock indicated by a dashed circle.
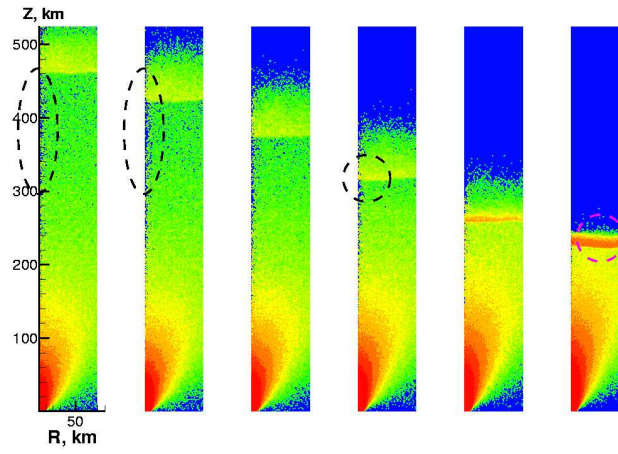
Figure D.2: Time evolution of instantaneous number density contours of a simulated unsteady Pele type plume. Note the "bubbles" indicated by the dashed ovals and the sign of "collapsing" (instability) of the shock indicated by dashed circles.
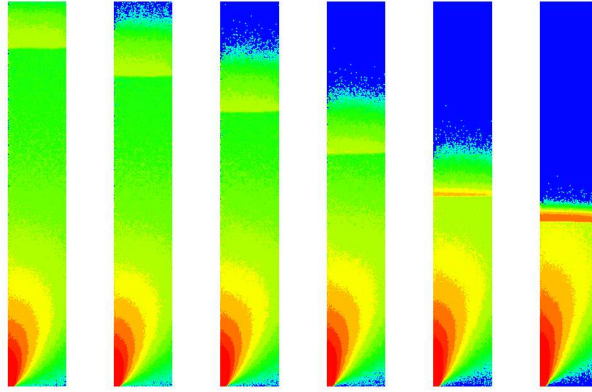
Figure D.3: Time evolution of instantaneous number density contours of a simulated Pele type plume. The simulation conditions are the same as that for the plume shown in Fig. D.2 except that the instantaneous number of simulated molecules is about 10 times larger.

Appendix E

# The Effect of Initial Velocity of Entrained Particles

The effect of the initial velocity of particles released at the vent is examined here. This initial velocity effect turns out to be very small for nano-size particles for both Pele and Prometheus type plumes. This is shown by the density fields in Figs. E.1 for a Pele type plume and E.2 for a Prometheus type plume. It is seen in Figs. E.1a and E.1b that for particles smaller than 100 nm, the initial velocity effect is very small. In fact, this is true for all the particle sizes of interest for a Prometheus type plume due to the relatively small variation in the gas density along the plume axis and the resulting strong coupling between the motions of the gas and the particles. The initial velocity, however, is important for a Pele type plume if the particles are large (> 100 nm). It is seen in Figs. E.1c and E.1d that the large particles with initial velocities equal to the vent velocity can at least reach the ballistic height while those starting out motionless cannot due to insufficient drag/acceleration and early decoupling from the gas motion.
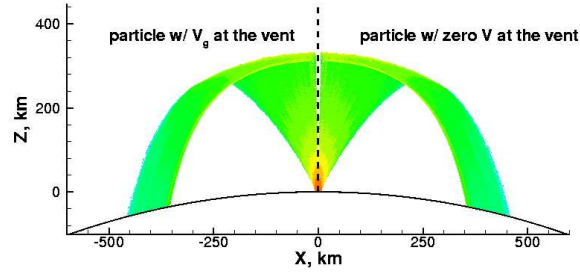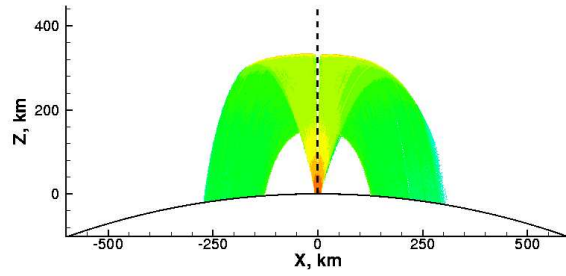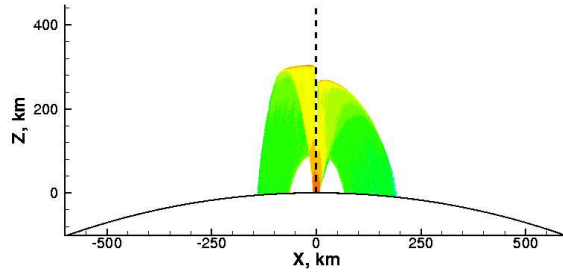
Figure E.1: Particle density fields in a Pele type plume for particles having the same velocity as that of the gas at the vent (left) and for particles starting at rest (right). The particle sizes are a) 10 nm, b) 100 nm, c) 300 nm, and d) 1 μm.
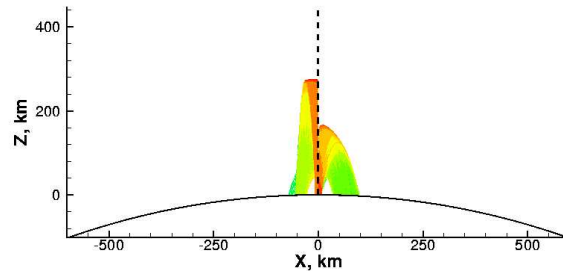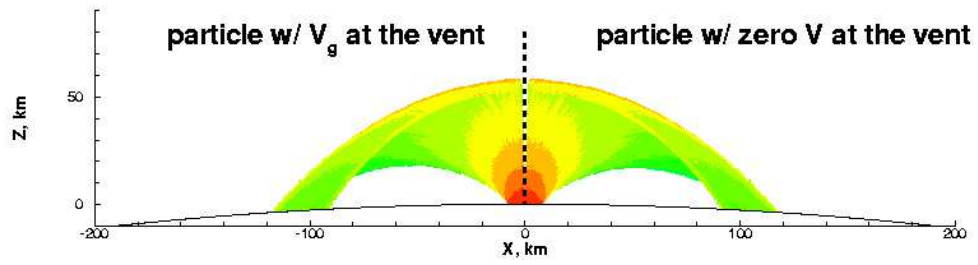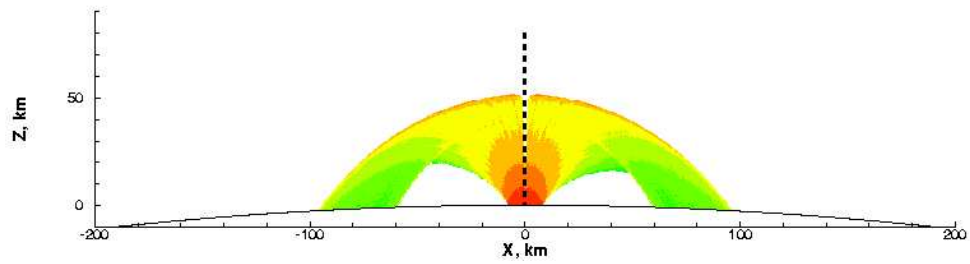
Figure E.2: Particle density fields in a Prometheus type plume for particles having the same velocity as that of the gas at the vent (left) and for particles starting at rest (right). The particle sizes are a) 10 nm, b) 30 nm, c) 80 nm, and d) 100 nm.
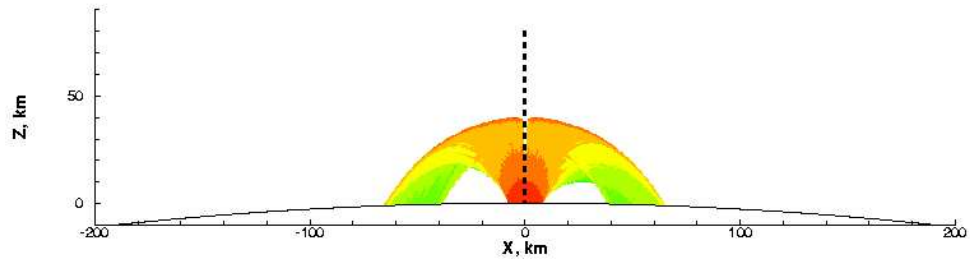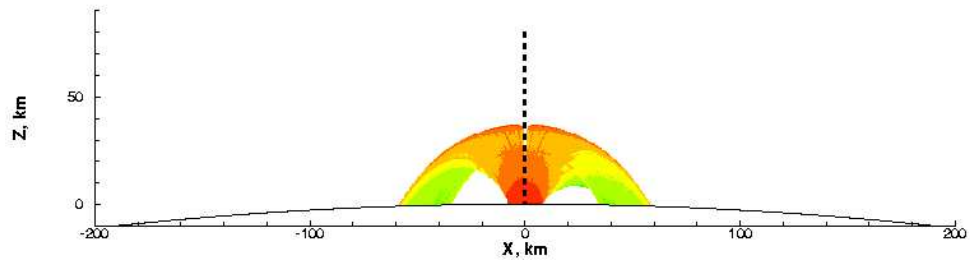
Appendix F

Preliminary results of a Parametric Study of Entrained Particle Mass Loading in a Prometheus type Plume

Fully coupled two-phase gas/particle flow is briefly examined using the DSMC method. The particles are treated as large hard-sphere molecules having no internal energy modes and they are made to collide with the gas molecules. The "overlay" assumption is dropped so that the particle flow affects the gas dynamics. Note that all the simulations discussed here correspond to plumes rising from evaporating lava. Both the gas and particle velocity are diffusively generated at a disk temperature of 350 K. Thus, while the SO_2 molecules rise with an initial speed of $\sim$200 m/s, the particles initially rise with a small speed of $\sim$20 m/s and must be dragged up to higher speeds by the gas. A parametric study of the mass loading of 1 nm dust in a simulated Prometheus plume is performed with the number density of the gas kept fixed at the vent. Figure F.1 shows that as the mass loading of the dust particles is increased, the gas plume rises lower and lower due to the increasing particle mass loading. Dust particles start out moving slower because of the smaller thermal velocity, and prevent the gas from rising higher and expanding wider. Note that when the dust mass dominates, as shown in Figure F.1c, the plume
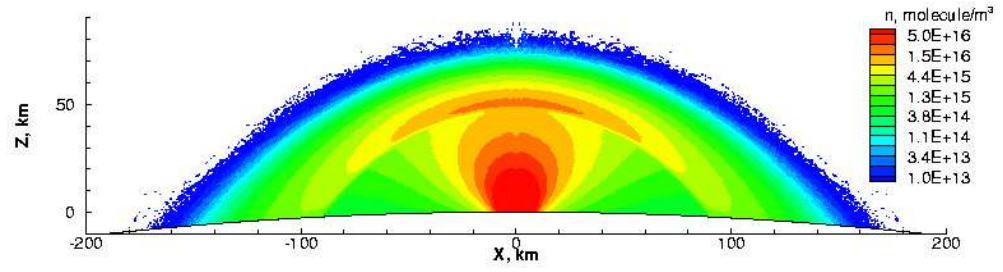
a)
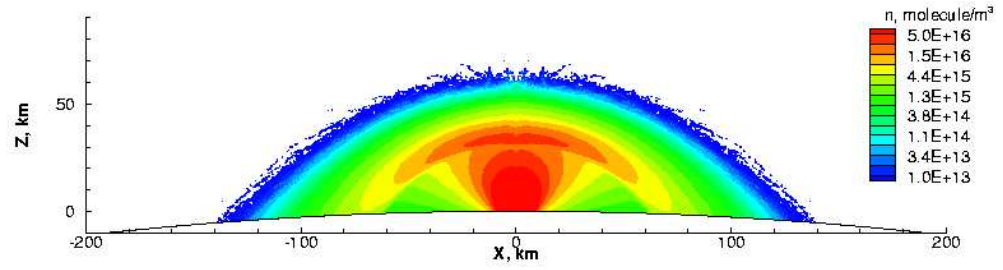
b)
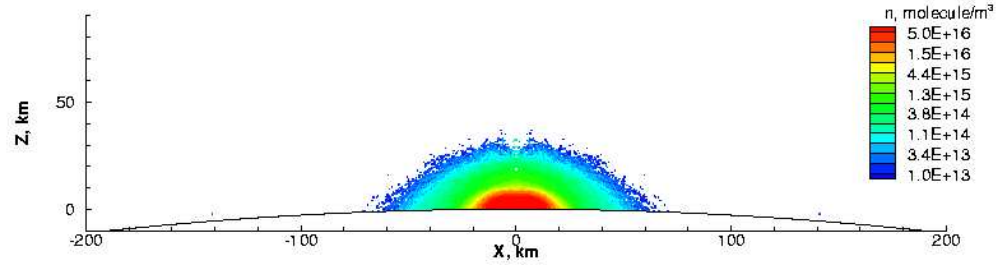
c)

Figure F.1: Total number density contours (of both gas and dust) of simulated Prometheus type plumes with a) ∼ 6%, b)∼ 30%, and c) ∼ 300% 1 nm dust mass loading at the vent. The corresponding particle number density loads are 0.1%, 0.5%, 5%.
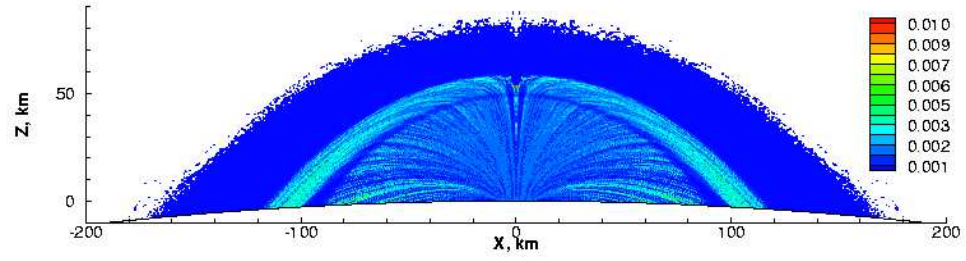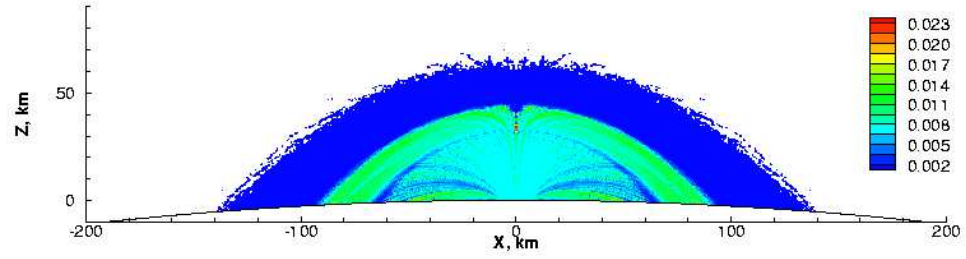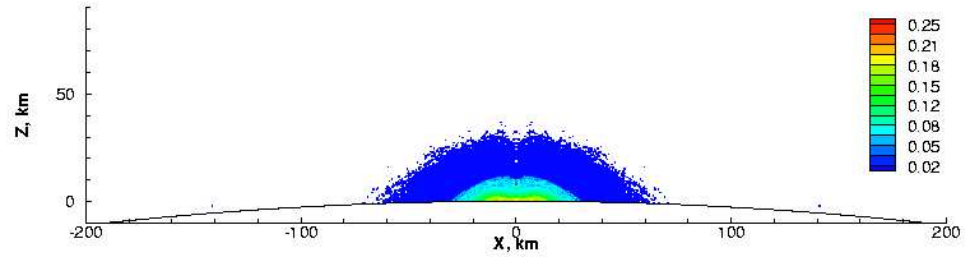
Figure F.2: Dust number concentration contours of simulated Prometheus type plumes with a) $\sim 6\%$, b)$\sim 30\%$, and c) $\sim 300\%$ 1 nm dust mass loading at the vent. Note the change in color bar between figures. The dark blue regions indicates virtually pure gas regions.

becomes a sublimation-driven-like flow without the presence of a canopy shock. The flow is like that of a gas having a smaller specific gas constant R when collisions between gas and particles are sufficiently frequent. The lower specific gas constant R in case c) due to the large dust mass loading causes a small value of S discussed in the Discussion Section, and thus the flow is more like sublimation-driven flow. Figure F.2 further illustrates where the gas becomes "free" by the boundaries between the green and dark blue color in the figures.

Appendix G

Table of Assumptions Used in the Simulations and Miscellaneous Notes about the Computational Codes

G.1 Table of Assumptions

Table G.1: Assumptions used in the results

Figure number	vg	sph	Z_v	IR	mic	o	mul
c1: Figs. 4.1- 4.18	no	no	no	no	no	no	yes
c2: Figs. 4.22- 5.6, 5.15, 5.16b-c,[a]	yes	yes	yes	yes	yes	no	no
c3: Fig. 5.35- 5.37	no	no	no	no	no	yes	no
c4: The rest of the figures	no	no	no[b]	no	no	no	no

[a]Also, Figs. 5.17a, 5.18- 5.24. Except that Fig. 5.5 belongs to category c4.
[b]Unless otherwise specified.

Note that abbreviations vg, sph, Z_v, IR, mic, o, and mul represent variable gravity, spherical geometry, new vibrational relaxation model, new infrared emission model, correct microwave (rotational) emission model, partially opaque gas model, and multiple domain calculation, respectively. Note that, in general, the Collision Model for gas/particle flow modeling needs to be upgraded in the future to account for the new features.

G.2   Notes about the Codes

The source codes for the most recent model in C is stored in /home/ jzhang/new_prog_pgz21tran/Aprog. The code has been subject to a variety of checks each time a new physical feature was added. Usually, this was done by finding a problem that was simple enough to have an analytical solution and comparing the DSMC calculation of the problem with the analytical solution. Cross-validation was also used sometimes as seen in the discussion of the Collision Model and Drag Model for gas/particle flow modeling. Sensitivity of the solution to many of the simulation parameters is examined to determine the uncertainty of the simulation results.

The single domain computation of a nominal Pele type plume with ~ 8 km vent radius usually takes a couple of days with ~ 2 GHz CPU. To determine when the flow has reached steady state, animation of transient flow can be used, and a quick but rough check is that the total number of simulated molecules in the whole domain stays approximately constant. Calculation of a small Prometheus type plume takes less than one day if the surface temperature is low. When the surface temperature is high, it takes much longer for the "bounce" to reach steady states. The Collision Model for simulating gas/particle flow is stored in /scratch/jzhang/prog/dust/prog_wgdcol/Freeze/Prom/Ts90/Aparal/AnoFree ze/AProm_old_match. It needs to be upgraded to include the new features such as the spherical geometry and the variable g.

References

Austin, J. V., and D. B. Goldstein 1995. Direct numerical simulation of low-density atmospheric flow on Io. In *Molecular Physics and Hypersonic Flows* (M. Capitelli, Ed.), pp. 749–758. Kluwer Academic Publishers.

Austin, J. V., and D. B. Goldstein 1998. Simulation of supersonic rarefied atmospheric flows on Io. In *Rarefied Gas Dynamics* (R. Brun, R. Campargue, R. Gatignol, and J. C. Lengrand, Eds.), Vol. 2, pp. 681–688. Cepadues-Editions, Toulouse, France.

Austin, J. V., and D. B. Goldstein 2000. Rarefied gas model of Io's sublimation driven atmosphere. *Icarus* **148**, 370–383.

Ballester, G. E., M. A. McGrath, D. F. Strobel, X. Zhu, P. D. Feldman, and H. W. Moos 1994. Detection of the SO_2 atmosphere on Io with the Hubble Space Telescope. *Icarus* **111**, 2–17.

Bass, H. E., T. G. Winter, and L. B. Evans 1971. Vibrational and rotational relaxation in sulfur dioxide. *J. Chem. Phys.* **54**, 644.

Bergemann, F., and I. D. Boyd 1994. Dsmc simulation of inelastic collisions using the Borgnakke-Larsen method extended to discrete distributions of vibrational energy. In *Rarefied Gas Dynamics: Theory and Simula-*

tions (B. D. Shizgal and D. P. Weaver, Eds.), pp. 174–183. Progress in Astronautics and Aeronautics.

Binder, A. P., and D. P. Cruikshank 1964. Evidence for an atmosphere on Io. *Icarus* **3**, 299–305.

Bird, G. A. 1994. *Molecular Gas Dynamics and the Direct Simulation of Gas Flows.* Oxford University Press.

Collins, S. A. 1981. Spatial color variations in the volcanic plume at Loki, on Io. *J. Geophys. Res.* **86**, 8621–8626.

Cook, A. F., E. M. Shoemaker, and B. A. Smith 1979. Dynamics of volcanic plumes on Io. *Nature* **280**, 743–746.

Douté, S., R. Lopes, L. W. Kamp, R. Carlson, B. Schmitt, and The Galileo NIMS Team 2002. Dynamics and evolution of SO_2 gas condensation around Prometheus-like volcanic plumes on Io as seen by the near infrared mapping spectrometer. *Icarus* **158**, 460–482.

Fanale, F. P., W. B. Banerdt, and D. P. Cruikshank 1981. Io: Could SO_2 condensation/sublimation cause the sometimes reported post-eclipse brightening? *Geophys. Res. Lett.* **8**, 625–628.

Feldman, P. D., D. F. Strobel, H. W. Moos, K. D. Retherford, B. C. Wolven, M. A. McGrath, F. L. Roesler, R. C. Woodward, R. J. Oliverson, and G. L. Ballester 2000. Lyman-alpha imaging of the SO_2 distribution on Io. *Geophys. Res. Lett.* **27**, 1787–1790.

Geissler, P. E., A. S. McEwen, W. lp, M. J. S.Belton, T. V. Johnson, W. H. Smyth, and A. P. Ingersoll 1999. Galileo imaging of atmospheric emissions from Io. *Science* **285**, 870–874.

Geissler, P. E., A. S. McEwen, C. Phillips, L. Keszthelyi, and J. Spencer 2003. Surface changes on Io during the Galileo mission. *Lunar and Planet. Sci. XXXIV, Abstract 1596.*

Gimelshein, S. F., A. A. Alexeenko, and D. A. Levin 2001. Modeling of the interaction of a side jet with a rarefied atmosphere. *AIAA paper 2001-0503.*

Ingersoll, A. P. 1989. Io meteorology: How atmospheric pressure is controlled locally by volcanos and surface frosts. *Icarus* **81**, 298–313.

Ingersoll, A. P., M. E. Summers, and S. G. Schlipf 1985. Supersonic meteorology of Io: Sublimation-driven flow of SO_2. *Icarus* **64**, 375–390.

Jessup, K., J. Spencer, G. Ballester, R. Howell., F. Roesler, M. Vigil, and R. Yelle 2003. The atmospheric signature of Io's Prometheus plume and anti-jovian hemisphere: Evidence for a sublimation atmosphere. *submitted to Icarus.*

Johnson, T. V., and D. L. Matson 1989. In *Origin and Evolution of Planetary and Satellite Atmospheres* (S. K. Atreya, J. B. Pollack, and M. S. Matthews, Eds.), pp. 666–681. Univ. of Arizona Press, Tucson.

Kerton, C. R., F. P. Fanale, and J. R. Salvail 1996. The state of SO_2 on Io's surface. *J. Geophys. Res.* **101**, 7555-7564.

Kieffer, S. W. 1982. Dynamics and thermodynamics of volcanic eruptions: Implications for the plumes of Io. In *Satellites of Jupiter* (D. Morrison, Ed.), pp. 647–723. Tucson: Univ. of Arizona Press.

Kieffer, S. W., R. Lopes-Gautier, A. McEwen, W. Smythe, L. Keszthelyi, and R. Carlson 2000. Prometheus: Io's wandering plume. *Science* **288**, 1204–1208.

Kliore, A. J., G. Fjeldbo, B. L. Seidel, D. N. Sweetnam, T. T. Sesplaukis, P. M. Woiceshyn, and S. I. Rasool 1975. The atmosphere of Io from Pioneer 10 radio occultation measurements. *Icarus* **24**, 407-410.

Lambert, J. D. 1977. *Vibrational and Rotational Relaxation in Gases.* Oxford University Press.

Lambert, J. D., and R. Salter 1957. Ultrasonic dispersion in gaseous sulphur dioxide. *Proc. Roy. Soc.* **243**, 78–83.

Larsen, P. S., and C. Borgnakke 1974. Paper a7. In *Rarefied Gas Dynamics* (M. Becker and M. F. Capitelli, Eds.). CFVLR Press, Porz-Wahn, Germany.

Lellouch, E. 1996. Io's atmosphere: Not yet understood. *Icarus* **124**, 1–21.

Lellouch, E., M. Belton, G. P. Ballester, and I. D. Pater 1994. Millimeter-wave observations of Io's atmo-sphere: New data and new models. *Bull. Am. Astron. Soc.* **26**, 1136.

Lellouch, E., M. Belton, I. de Pater, G. Paubert, S. Gulkis, and T. Encrenaz 1992. The structure, stability, and global distribution of Io's atmosphere. *Icarus* **98**, 271–295.

Lellouch, E., T. Encrenaz, M. Belton, I. dePater, and S. Gulkis 1990. Io's atmosphere from microwave detection SO2. *Nature* **346**, 639-641.

Lellouch, E., G. Paubert, J. I. Moses, N. M. Schneider, and D. F. Strobel 2003. Volcanically emitted sodium chloride as a source for Io's neutral clouds and plasma torus. *Nature* **421**, 45–47.

Lopes-Gautier, R. M. C., L. W. Kamp, and S. Doute *et al.* 2002. Io in the near infrared: Near-infrared mapping spectrometer (NIMS) results from the Galileo flybys in 1999 and 2000. *J. Geophys. Res.* **106**, 33,053–33,078.

Matson, D. L., G. J. Veeder, T. V. Johnson, D. L. Blaney, and A. G. Davies 2002. The mystery of Io's warm polar regions: Implications for heat flow. *Lunar and Planet. Sci. XXXIII.*

McEwen, A. S., L. Keszthelyi, P. Geissler, D. P. Simonelli, M. H. Carr, T. V. Johnson, K. P. Klaasen, H. H. Breneman, T. J. Jones, J. M. Kaufman, K. P. Magee, D. A. Senske, M. J. S. Belton, and G. Schubert 1998. Active Volcanism on Io as Seen by Galileo SSI. *Icarus* **135**, 181-219.

McEwen, A. S., and L. A. Soderblom 1983. Two classes of volcanic plumes on Io. *Icarus* **58**, 197-226.

McGrath, M. A., M. J. S. Belton, J. R. Spencer, and P. Sartoretti 2000. Spatially resolved spectroscopy of Io's Pele plume and SO_2 atmosphere. *Icarus* **146**, 476–493.

Moore, C., J. Zhang, D. B. Goldstein, P. L. Varghese, and L. M. Trafton 2003. Modeling of particulates and condensates in Io's Pele-type volcanic plumes. *Lunar and Planet. Sci. XXXIV, Abstract 2102.*

Moreno, M. A., G. Schubert, J. Baumgardner, M. G. Kivelson, and D. A. Paige 1991. Io's volcanic and sublimation atmospheres. *Icarus* **93**, 63–81.

Moses, J. I., M. Y. Zolotov, and J. B. Fegley 2002a. Photochemistry of a volcanically driven atmosphere on Io: Sulfur and oxygen species from a Pele-type eruption. *Icarus* **156**, 76–106.

Moses, J. I., M. Y. Zolotov, and J. B. Fegley 2002b. Alkali and chlorine photochemistry in a volcanically driven atomosphere on Io. *Icarus* **156**, 107–135.

Nash, D. B., F. P. Fanale, and R. M. Nelson 1980. SO_2 frost: UV-visible reflectivity and Io surface coverage. *Geophys. Res. Lett.* **7**, 665–668.

Nelson, R. M., A. L. Lane, M. E. Morrill, B. D. Wallis, J. Gibson, W. D. Smythe, L. J. Horn, and B. J. Buratti 1993. The brightness of Jupiter's

satellite Io following emergence from eclipse: Selected observations, 1981-1989. *Icarus* **101**, 223–233.

Pearl, J. C., R. Hanle, V. Kunde, W. Maguire, K. Fox, S. Gupta, C. Ponnamperuma, and F. Raulin 1979. Identification of gaseous SO_2 and new uppel limits for other gases on Io. *Nature* **288**, 757–758.

Penner, S. S. 1959. *Quantitative Molecular Spectroscopy and Gas Emissivities.* Addison-Wesley Publishing Company, Inc.

Quine, B. M., and J. R. Drummond 2002. Genspect: a line-by-line code with selectable interpolation error tolerance. *The Journal of Quantitative Spectroscopy and Radiative Transfer* **74**(2).

Radzig, A. A., and B. M. Smirnov 1980. *Reference data on atoms, molecules, and ions.* Springer-Verlag.

Rathbun, J. A., J. R. Spencer, L. K. Tamppari, T. Z. Martin, L. Barnard, and L. D. Travis 2002. Recent results from Galileo PPR at Io: Orbits I31 and I32. *Lunar and Planet. Sci. XXXIII.*

Rathbun, J. A., J. R. Spencer, L. K. Tamppari, T. Z. Martin, L. Barnard, and L. D. Travis 2003. Mapping of Io's thermal radiation by the galileo photopolarimeter-radiometer (PPR) instrument. *submitted to Icarus.*

Roveda, R., D. B. Goldstein, and P. L. Varghese 1997. A combined discrete velocity/particle based numerical approach for continuum/rarefied flows. *AIAA paper 97-1006.*

Sandford, S. A., and L. J. Allamandola 1993. The condensation and vaporization behavior of ices containing SO_2, H_2S, and CO_2: Implications for Io. *Icarus* **106**, 478–488.

Sartoretti, P., M. J. S. Belton, and M. A. McGrath 1996. SO_2 Distributions on Io. *Icarus* **122**, 273–287.

Schneider, N. M., D. M. Hunten, W. K. Wells, A. B. Schultz, and U. Fink 1991a. The structure of Io's corona. *Astrophys. J.* **368**, 298–315.

Spencer, J. R., K. L. Jessup, M. A. McGrath, G. E. Ballester, and R. Yelle 2000. Discovery of gaseous S_2 in Io's Pele plume. *Science* **288**, 1208–1210.

Spencer, J. R., J. A. Rathbun, w. A. S. McEwen, J. C. Pearl, A. Bastos, J. Andrade, M. Correia, and S. Barros 2002. A new determination of Io's heat flow using diurnal heat balance constraints. *Lunar and Planet. Sci. XXXIII.*

Spencer, J. R., P. Sartoretti, G. E. Ballester, A. S. McEwen, J. T. Clarke, and M. A. McGrath 1997. Pele plume (Io): Observations with the Hubble Space Telescope. *Geophys Res Let* **24**, 2471.

Spencer, J. R., and N. M. Schneider 1996. Io on the eve of the galileo mission. *Ann. Rev. of Earth Planet. Sci.* **24**, 125–190.

Strobel, D. F., and B. C. Wolven 2001. The atmosphere of Io: Abundances and sources of sulfur dioxide and atomic hydrogen. *Astrophys. Space Sci.* **277**, 271–287.

Strobel, D. F., X. Zhu, and M. E. Summers 1994. On the vertical thermal structure of Io's atmosphere. *Icarus* **111**, 18–30.

Strom, R. G., and N. M. Schneider 1982. Volcanic eruption plumes on Io. In *Satellites of Jupiter* (D. Morrison, Ed.), pp. 598–633. Tucson: Univ. of Arizona Press.

Trafton, L. M., J. . Caldwell, C. Barnet, and C. C. Cunningham 1996. The gaseous sulfur dioxide abundance over Io's leading and trailing hemisphere: HST spectra of Io's c^1b_2 - x^1a_1 band of SO_2 near 2100 $\mathring{A}$. *Astrophys. J.* **456**, 384-392.

Vincenti, W. G., and C. H. Kruger 1965. *Introduction to Physical Gas Dynamics.* Krieger.

Wong, M. C., and R. E. Johnson 1995. The effect of plasma heating on sublimation-driven flow in Io's atmosphere. *Icarus* **115**, 109–118.

Wong, M. C., and R. E. Johnson 1996. A three-dimensional azimuthally symmetric model atmosphere for Io, 1. Photochemistry and the accumulation of a nightside atmosphere. *J. Geophys. Res.* **101**, 23243–23254.

Wong, M. C., and W. H. Smyth 2000. Model calculations for Io's atmosphere at eastern and western elongations. *Icarus* **146**, 60–74.

Zhang, J., D. B. Goldstein, N. E. Gimelshein, S. F. Gimelshein, D. A. Levin, and P. L. Varghese 2001. Modeling low density sulfur dioxide jets: application to volcanoes on Jupiter's moon Io. *AIAA paper 2001-2767 presented at 35th AIAA Thermophysics Conference, Anaheim, CA, June 11-14, 2001.*

Zhang, J., D. B. Goldstein, P. L. Varghese, N. E. Gimelshein, S. F. Gimelshein, and D. A. Levin 2003a. Simulation of gas dynamics and radiation in volcanic plumes on Io. *Icarus* **163**, 182–197.

Zhang, J., D. B. Goldstein, P. L. Varghese, N. E. Gimelshein, S. F. Gimelshein, D. A. Levin, and L. M. Trafton 2003b. DSMC modeling of gasdynamics, radiation and fine particulates in Ionian volcanic jets. In *Proceedings of 23rd International Symposium on Rarefied Gas Dynamics* (A. Ketsdever and E. P. Muntz, Eds.), Vol. 663, pp. 704–711. AIP, New York.

Zhang, J., D. B. Goldstein, P. L. Varghese, L. M. Trafton, K. Miki, and C. Moore 2004. Numerical modeling of ionian volcanic plumes with entrained particulates. *submitted to Icarus.*

Zhang, J., K. Miki, D. B. Goldstein, P. L. Varghese, and L. M. Trafton 2003c. Modeling of radiation above Io's surface from Pele-type volcanic plumes and underground from the conduit wall. *Lunar and Planet. Sci. XXXIV, Abstract 2123.*

Zolotov, M. Y., and B. Fegley 2001. Chemistry and vent pressure of very high-temperature gases emitted from Pele volcano on Io. *Lunar and Planet. Sci. XXXII, Abstract 1474.*

Index

237

Vita

Ju Zhang was born in Shenyang, China on 24 January 1975, the son of Yuxuan Zhang and Fengyun Pang. He received the Bachelor of Science degree in Mechanics from the University of Science and Technology of China, Hefei in 1998. He was accepted and started graduate studies in Aerospace Engineering at the University of Texas at Austin in January, 1999. His research at UTA has been supported by NASA planetary atmospheres program.

Permanent address: Department of Astronomy and Astrophysics
University of Chicago
5640 South Ellis Avenue
Chicago, IL 60637

This dissertation was typeset with LaTeX† by the author.

---

†LaTeX is a document preparation system developed by Leslie Lamport as a special version of Donald Knuth's TeX Program.